



UNIVERSITA' DEGLI STUDI DI VERONA

DEPARTMENT OF COMPUTER SCIENCE

GRADUATE SCHOOL OF NATURAL AND ENGINEERING SCIENCE

*DOCTORAL PROGRAM IN
NANOSCIENCE AND ADVANCED TECHNOLOGIES*

Cycle/year XXX/2014

**Structural and vibrational spectroscopy characterizations of carbon
nanostructures synthesized using mineral oxides**

S.S.D. FIS/01 EXPERIMENTAL PHYSICS

Coordinator: Prof. Franco Tagliaro

Signature

Tutor: Prof. Gino Mariotto

Signature

Doctoral Student: Arun Kumar

Signature

To my family

Acknowledgement

This research report arose in parts out of years of research that has been done since I came to University of Verona, Italy. By this time, I have shared experiences with a great number of people whose contribution in assorted ways to the research and the making of the report, deserved special mention. It is a pleasure to convey my gratitude to them all in my humble acknowledgment.

I am grateful to **Prof. Nicola Sartor, Rector & Prof. Franco Tagliaro, Coordinator, PhD Nanoscience & Advanced Technologies, University of Verona, Italy**, for kindly allowing me to undertake the research activities project at Vibrational Spectroscopy Laboratory.

Firstly, I would like to thank my PhD supervisor **Prof. Gino Mariotto, Head, Vibrational Spectroscopy Laboratory, Department of Computer Science, University of Verona, Italy** for his meticulous guidance, discussion, support, and constant encouragement along with invaluable suggestions, support during experimental work during my stay at his laboratory. I sincerely appreciate his way of working and magnitude of patience with which he taught me. His truly scientist intuition has made him as a constant oasis of ideas and passions in science, which exceptionally inspire and enrich my growth as a student, a researcher and a scientist want to be. I am indebted to him more than he knows.

A deep sense of gratitude is extended to **Dr. Gilbert Daniel Nessim, Department of Chemistry, Bar Ilan University, Israel** for considering me able to work with him under his supervision, and making me familiar with chemical vapour deposition and other physical techniques available at his laboratory.

In a soft place, I would like to record my gratitude to **Dr. Marco Giarola** for his advice, and guidance from the very early stage of this research as well as giving me his precious time to teach me all the scientific instruments available in the laboratory. Above all and the most needed, he provided me unflinching encouragement and support in various ways.

I am deeply overwhelmed to other lab and group members, **Dr. Nicola Daldosso**, **Dr. Marco Zanatta**, **Ms. Elena Chiste**, **Mr. Michele Cassetta** and **Dr. Ali Ghafarinazari** whose very presence somehow has perpetually refreshing, helpful, and memorable.

I owe my most sincere thanks to my parents, my younger brother **Mr. Amarjit Singh** for their constant support and motivation, for managing my long absence from home and for always being my inspiration through all up and downs during the course. I am really indebted to them. Apart from my family I am very much thankful to **Mr. Vidhi Chand**, **Ms. Vandana Yadav**, for encouraging and motivating every time I visit to their sweet home. And love and affection with them cannot be explained in words.

I would like to thanks my close friends **Mr. Rohit**, **Mr. Pankaj Saraswat**, **Mr. Kaushik Kushik**, **Mr. Jitender Saini**, **Mr. Vipin Sharma**, **Mr. Kulvir Singh**, **Mr. SK Tarik Aziz**, **Dr. Rajasekar Nagarajan**, for their consistent support and love.

To God for giving me encouragement to complete this step and an endless source of inspiration for me always.

(Arun Kumar)

Abstract

Carbon nanostructures have attracted increasing interest in the past two decades due to their singular properties and their potential applications in the field of nanotechnology. Current processes with the active metals for the hydrocarbon decomposition are not meeting the present demand and supply of carbon nanomaterials on large scale level. However, metals or metal oxides, in small or even trace amounts, can be easily found in almost all natural materials and they are in the ideal form to be used as catalysts for carbon nanomaterials synthesis via CVD route. In this thesis work, we have focused on synthesis of carbon nanostructures using natural materials such as low Ni content iron laterite ores, siliceous breccia, as a catalyst and organic matter rich black carbon powder and hydrocarbon gases as a precursor and the growth process behind it. The **1st chapter** gives a brief and general background on carbon nanomaterials, on related synthesis methods and underlying growth mechanisms. In **2nd chapter**, synthesis process and characterization techniques have been explained in details with their working and characterization process. The **3rd chapter** deals with the synthesis of carbon nanostructures on dehydrated limonite laterite as catalyst carried out via CVD route under methane flux the phase transformation from FeOOH to Fe_2O_3 was carried out successfully in the reducing Ar atmosphere, which was used as a catalyst source. The diameter of the carbon nanotubes was found to vary between 10 and 100 nm, and to increase with the CVD chamber temperatures. Furthermore, the **4th chapter**, reports a detailed study on the synthesis of growth of carbon nanostructures on natural limonite laterite iron ore with low-Ni content under ethylene flux, and a comparative study as a function of the temperature as well as of the $\text{H}_2/\text{C}_2\text{H}_4/\text{Ar}/\text{O}_2$ flux ratio supplied on the catalyst. Before the catalytic tests, iron existed as Fe_2O_3 (limonite laterite after dehydration). During the catalytic tests, Fe_2O_3 has been reduced to Fe_3O_4 , FeO , or Fe as the deposition temperature increase from 700 to 800 and 900 °C. Another interesting behaviour of the as synthesized carbon nanostructures is that it starts forming a carbon nanospheres when the deposition temperature increases.. The **5th chapter** concerns the synthesis of carbon nanotubes on the natural drill core siliceous breccia powder

containing mainly quartz and some traces of hematite and goethite. Furthermore, comparative studies by varying the H_2/C_2H_4 flux ratio supplied on the catalyst. The **6rd chapter** deals with two cases of drilled core organic matter rich black shale samples. In the first case, the results of combined spectroscopic analyses, performed on an organic matter rich black carbon sample, are considered. The aim of the work was to detect the major mineral component phases. Further, in the second case, black shale carbon powders, mainly containing quartz and dolomite, were exploited to obtain coating layers, on Cu substrates. Finally, in the **7th chapter**, the results of the investigation of vibrational properties of silicon oxycarbide powders, doped with different amounts of boron, produced from sol-gel-derived poly(boro)siloxanes are reported and discussed. The evolution of Raman spectra of the different samples, annealed at 1200 °C and 1400 °C, has been investigated in order to get insights about the effects of Boron-doping on the nanostructure of the studied materials.

CONTENTS

Chapter	Description	Page No.
	Abstract	iv-v
1.	State of the art about carbon nanostructures and natural materials as catalysts: historical background, definition, and their potential applications	1-29
	<hr/>	
	1.1 Introduction	1
	1.2 Carbon materials and their classifications	2
	1.2.1 Diamond	2
	1.2.2 Graphite	3
	1.2.3 Fullerene	4
	1.2.4 Carbon nanotubes	5
	1.2.4.1 Discovery	5
	1.2.4.2 Structure	7
	1.2.4.3 Classification of carbon nanotubes	8
	1.2.5 Carbon nanopearls	12
	1.2.5.1 Difference between carbon nanopearls and other carbon structures	16
	1.2.6 Carbon spheres	17
	1.3 Natural materials as catalysts for nano carbon synthesis	20
	1.4 Structural and vibrational spectroscopy characterizations of carbon nanostructures synthesized using mineral oxides: objective of present work.	25
	1.5 References	27

2.	Experimental technique for carbon nanostructures synthesis, structural/ microstructural characterization and vibrational spectroscopy of both natural and as-processed minerals	30-53
	<hr/>	
	2.1 Introduction	30
	2.2 Chemical Vapour Deposition (CVD) technique	30
	2.3 Structural/microstructural analysis techniques	32
	2.3.1 X-ray diffraction techniques	32
	2.3.1.1 Principle of XRD	33
	2.3.1.2 Working of XRD	34
	2.3.2. Environmental Scanning Electron Microscope (ESEM)	36
	2.3.2.1 Construction and working of SEM	37
	2.3.2.2 Essential components of SEM	38
	2.3.2.3 Equipment details	39
	2.4 Spectroscopic analysis	40
	2.4.1 Fourier Transforms Infrared Spectroscopy (FT-IR)	40
	2.4.1.1. Principle of FTIR spectroscopy	40
	2.4.1.2. Working of FTIR spectrometer	42
	2.4.2 Micro Raman spectroscopy	44
	2.4.2.1 Brief remarks about Raman scattering	45
	2.4.2.2 Working of micro-Raman spectrometer LabRam HR800	47
	2.5 References	51
3.	Growth of carbon nanostructures using natural limonite laterite as catalyst via methane decomposition	54-69
	<hr/>	
	3.1 Introduction	54

	3.2 Synthesis of MWCNTs by chemical vapour deposition	54
	3.2.1 Catalyst preparation and methane decomposition	55
	3.3 Structural and spectroscopic characterization of calcined Ni-containing iron ore laterite powders and of synthesised MWCNTs	57
	3.4 Results and discussions	59
	3.4.1 Structural / microstructural characterizations	59
	3.4.1.1 Gross structural characterization	59
	3.4.1.2 Surface morphology	60
	3.4.2 Spectroscopic Analysis of raw natural low Ni containing iron ores before and after dehydration and of the synthesised MWCNTs	63
	3.4.2.1 Micro-Raman investigations on both raw Ni containing iron ore laterite sample and the as synthesized MWCNTs	63
	3.4.2.2 FT-IR (Fourier transform infrared spectroscopy) analysis of natural limonite laterite powder	67
	3.5 Conclusions	68
	3.6 References	69
4.	Growth of carbon nanostructures using limonite laterite as catalyst via ethylene decomposition	70-86
	<hr/>	
	4.1 Introduction	70
	4.2 Synthesis of carbon nanostructures by chemical vapour deposition	70
	4.2.1 Catalyst preparation and ethylene decomposition	70
	4.3 Structural and spectroscopic characterization of synthesised carbon nanostructures	72
	4.4 Results and discussions	73

	4.4.1 Structural / microstructural characterizations	73
	4.4.1.1 Gross structural characterization	73
	4.4.1.2 Surface morphology	75
	4.4.2 Spectroscopic analysis of synthesised carbon nanostructures	81
	4.5 Conclusions	85
	4.6 References	86
5.	Growth of carbon nanostructures using siliceous breccia powder as catalyst via ethylene decomposition	87-102
	<hr/>	
	5.1 Introduction	87
	5.2 Synthesis of carbon nanostructures by chemical vapour deposition	87
	5.2.1 Sample preparation and carbon nanostructures formation	90
	5.3 Characterization of natural drill core siliceous breccia and synthesized carbon nanostructures	91
	5.4 Results and discussions	92
	5.4.1 Structural / microstructural characterizations	92
	5.4.1.1 Gross structural characterization	92
	5.4.1.2 Surface morphology	94
	5.4.2 Spectroscopic analysis of natural siliceous breccia powder and synthesised carbon nanostructures	97
	5.4.2.1 Micro Raman spectroscopic analysis	97
	5.4.2.2 FTIR (Fourier transform infrared spectroscopy) of siliceous breccia	101
	5.5 Conclusions	102
	5.6 References	102

6.	Combined analysis & growth graphitic layers on cu substrate from drill core organic matter rich black shale carbon powder as precursor	103-121
	<hr/>	
	6.1 Introduction	103
	6.2 Organic matter rich black shale material origin, specification & synthesis of graphitic layers	104
	6.2.1 Sample Preparation and graphitic layers formation	106
	6.3 Characterization of natural black shale carbon powder and grown graphitic layers	109
	6.4 Results and discussions	110
	6.4.1 Structural / microstructural characterizations	110
	6.4.1.1 Gross structural characterization	110
	6.4.1.2 Surface morphology	112
	6.4.2 Spectroscopy analysis	114
	6.4.2.1 Micro Raman spectroscopic analysis	114
	6.4.2.2 FTIR (Fourier transform infrared spectroscopy) analysis	119
	6.5 Conclusions	120
	6.6 References	121

7.	Micro-Raman spectroscopy investigations on B-doped Silicon OxyCarbide [SiOC(B)] powders underwent thermal treatments at high-temperature	122-128
	7.1 Introduction	122
	7.2 Synthesis of the B-doped polymer derived Si(B)OC ceramics with different pyrolysis temperature	123
	7.3 Characterization of the B-doped polymer derived Si(B)OC ceramics with different pyrolysis temperature	124
	7.4 Results and discussions	124
	7.5 Conclusions	127
	7.6 References	128
8.	Conclusions, potential outcomes and future road map	129-131

List of Figures and Tables

Chapter 1:

Figure 1.1 Unit cell of diamond.

Figure 1.2 Structure of graphite.

Figure 1.3 Buckminsterfullerene (C₆₀) molecule.

Figure 1.4 High Resolution Transmission Electron Microscope (HRTEM) image of first observed MWCNTs by Iijima in 1991.

Figure 1.5 Computer generated image of a multi-walled carbon nanotubes (MWCNTs).

Figure 1.6 Computer generated image of a single-walled carbon nanotubes (SWCNTs).

Figure 1.7 HRTEM (top) and computer generated (bottom) images of single-walled carbon nanotubes.

Figure 1.8 Distance between two nanotubes of MWCNTs is nearly same as the interlayer distance of graphite.

Figure 1.9 STM images of carbon nanotubes (a), (c) zigzag , and (b) armchair.

Figure 1.10 (a) The chiral vector OA or $Ch = na_1 + ma_2$ is defined on the honeycomb lattice of carbon atoms by unit vectors a_1 and a_2 and the chiral angle θ with respect to the zigzag axis. Along the zigzag axis $\theta = 0^\circ$. Also shown are the lattice vector $OB = T$ of the 1D nanotube unit cell and the rotation angle ψ and the translation τ which constitute the basic symmetry operation $R = (\psi | \tau)$ for the carbon nanotube. The diagram is constructed for $(n, m) = (4, 2)$. (b) Possible vectors specified by the pairs of integers (n, m) for general carbon nanotubes, including zigzag, armchair, and chiral nanotubes. Below each pair of integers (n, m) is listed the number of distinct caps that can be joined continuously to the carbon nanotube denoted by (n, m) . The encircled dots denote metallic nanotubes while the small dots are for semiconducting nanotubes.

Figure 1.11 Classification of carbon nanotubes: (a) armchair, (b) zigzag, and (c) chiral nanotubes. From the figure it can be seen that the orientation of the six membered ring in the honeycomb lattice relative to the axis of the nanotube can be taken almost arbitrarily.

Figure 1.12: TEM image of carbon nanopearl illustrating 3D arrangement of carbon nanopearls.

Figure 1.13 HRTEM images of carbon nanopearls having concentrically-oriented nano-sized graphitic flakes.

Figure 1.14: A diagram of the theoretical synthesis process of carbon nanopearls.

Figure 1.15 (a) Hexagon ring carbon structure with zero curvature, (b) pentagon ring structure with curvature around $+60^\circ$, (c) heptagon ring structure with outward curvature around -60° .

Figure 1.16: HRSEM image of carbon nanopearls via CVD process.

Figure 1.17: Carbon nanopearls grown over a Ni foil catalyst, using autoclave process.

Figure 1.18: Field emission data taken from CNPs.

Figure 1.19 A TEM images of CSs that have aggregated to form a necklace

Figure 1.20 Schematic representation of carbon black. (a) Carbon onion like structure; (b) aggregate of carbon-onion like structures (arrow indicates 'neck' between carbononions).

Figure. 1.21 Sketch indicating radial, concentric and random carbon layer orientations in CSs.

Figure. 1.22 Model showing cutaway of a single carbon black particle with concentric layers. Parallel orientation of ordered layer groupings and diminishing graphitic order near particle centre.

Chapter 2:

Figure 2.1 CVD system facility at Bar Ilan University.

Figure 2.2 Bragg's Law: $n\lambda = 2d\sin\theta$.

Figure 2.3 Schematic of the X-ray diffraction by a crystal.

Figure 2.4 A schematic representation of X-ray diffraction

Figure 2.5 X-ray Diffractometer process. DS=Divergence Slit, SS=Scatter Slit, RS=Receiving Slit, RSM= Receiving Slit Monochromator.

Figure 2.6 Six modes of SEM.

Figure 2.7 Components of SEM.

Figure 2.8 ESEM facility at Bar Ilan University, Israel.

Figure 2.9 (a) Schematic diagram of FTIR and (b) FTIR instrument.

Figure 2.10 Main Components of the Jobin Yvon HR800 micro-Raman instrument facility at University of Verona, Italy.

Figure 2.11 Example representations of the Rayleigh, Stokes and anti-Stokes components.

Indicates also the correspondence between the wavelength and wavenumbers with specific reference to wavelength = 5145 Å corresponding to 19436 cm⁻¹.

Figure 2.12 Optical layout of the Jobin Yvon HR800 micro-Raman instrument.

Figure 2.13 Resolution of the micro-Raman spectrograph for a slit width of 100 μm and the 1800 g/mm grating.

Figure 2.14 Response of the notch filter with the 10X objective and 1800 g/mm grating.

Chapter 3:

Table 3.1 Average elemental compositions of the natural low Ni containing iron ores used in this study.

Figure 3.1 EDX spectrum of the natural low Ni containing iron ores laterite powder.

Figure 3.2 Schematic diagram of the CVD equipment.

Figure 3.3 Schematic diagram for protocol of the synthesis MWCNTs.

Figure 3.4 XRD patterns of the natural low Ni containing iron ores limonite laterite powder before and after dehydration.

Figure 3.5 ESEM images of limonite laterite before dehydration (A); and after dehydration (B).

Figure 3.6 ESEM images of the synthesised MWCNTs at (a-b) 700 °C, (c-d) 800 °C and (e-f) 900 °C.

Figure 3.7 Typical Raman spectra recorded from different micro-regions of the natural low Ni containing iron (T Vol with 1.5 – 1.7 wt%-Ni) ore laterite powders: before dehydration (top panel), and after dehydration (bottom panel). In the upper panel the reference spectra, taken from RRUFF database, are also reported.

Figure 3.8 Raman spectrums of MWCNTs grown on dehydrated limonite laterite powder

Figure 3.9 FTIR spectrum of natural low Ni containing iron ore limonite laterite powder

Chapter 4:

Figure 4.1 Protocol for the synthesis of carbon nanostructures under ethylene flux.

Figure 4.2 XRD patterns of the carbon nanostructures grown on dehydrated limonite laterite at (a) 700 °C, (b) 800 °C and (c) 900 °C.

Figure 4.3 ESEM images of the carbon nanostructures at (a-b) 700 °C, (c-d) 800 °C and (e-f) 900 °C.

Figure 4.4 EDX analysis on the carbon spheres grown at 800 and 900 °C.

Figure 4.5 ESEM micrograph of flakes deposited on the quartz at 800 and 900 °C depicting carbon spheres bundles.

Figure 4.6 ESEM images of MWCNTs grown with Ar/H₂, 100/400 sccm for 15 min along with C₂H₄ flow 100 sccm for 30 min at 700 °C.

Figure 4.7 ESEM images of MWCNTs deposited via (a) The ethylene, C₂H₄ + Ar/H₂ + Ar/O₂ 100 sccm and (b) C₂H₄ + Ar/H₂ at the temp. of 770 °C in the first zones and 750 °C in the third zone.

Figure 4.8 Micro Raman spectrums of carbon nanostructures on limonite laterite powder ore after dehydration (DH) via C₂H₄ decomposition.

Figure 4.9 Micro Raman spectra of MWCNTs grown with Ar/H₂, 100/400 sccm for 15 min along with C₂H₄ flow 100 sccm for 30 min at 700 °C.

Figure 4.10 Micro Raman spectra of MWCNTs deposited via flow of ethylene, C₂H₄ with Ar/H₂ and Ar/O₂ 100 sccm (above) and C₂H₄ with Ar/H₂ (below) at the temp. of 770 °C in the first zones and 750 °C in the third zone.

Chapter 5:

Figure 5.1 Sketch of the sample preparation for the surface roughness analyses.

Figure 5.2 Optical images Sonic drilled cores siliceous breccia (left) and the powdered sample (< 80 µm) of the breccia (right).

Table 5.1 Average elemental Compositions of the natural siliceous breccia powder used in this study.

Table 5.2 Experimental diffraction angles and corresponding d-spacing of the siliceous breccia powder used in this study.

Figure 5.3 ESEM Micrograph for the EDX spectrum of the natural drill core siliceous breccia powder.

Figure 5.4 EDX spectrum of the natural drill core siliceous breccia powder.

Figure 5.5 Protocol for the synthesis MWCNTs.

Figure 5.6 XRD patterns of the natural drill core siliceous breccia.

Figure 5.7 ESEM micrographs on the natural siliceous breccia powder with different magnifications.

Figure 5.8 ESEM images of MWCNTs; (a), ESEM images of MWCNTs via C_2H_4/H_2 100/30 sccm flown at the temp. of 700 °C for 30 min; (b), ESEM images of MWCNTs via C_2H_4 100 sccm flown at the temp. of 700 °C for 30 min.

Figure 5.9 Raman spectrum of natural siliceous breccia powder.

Figure 5.10 Micro Raman Spectrum of MWCNTs grown via C_2H_4/H_2 100/30 sccm flown at 700 °C for 30 min.

Figure 5.11 Micro Raman Spectrum of MWCNTs grown via C_2H_4 100 sccm flown at the temp. 700 °C for 30 min.

Figure 5.12 (A) & (B) Comparison of Micro Raman Spectrum of MWCNTs grown via C_2H_4 with and without H_2 mixing flown at the temp. 700 °C for 30 min.

Figure 5.13 FTIR spectrum of siliceous breccia powder.

Chapter 6:

Figure 6.1 Optical image of the organic matter rich black shale (BC6).

Figure 6.2 Optical images Sonic drilled cores black shale (left) and the powdered sample ($< 80 \mu m$) of the carbon shale (right).

Figure 6.3 ESEM Micrograph for the EDX spectrum of the natural black carbon powder

Table 6.1 Table of average elemental composition from EDX analysis of the natural drill core organic matter rich black carbon powder.

Table 6.2 Experimental diffraction angles and corresponding d-spacing of the natural black carbon powder used in this study.

Figure 6.4 Quantitative analysis of the BC4 drill core organic matter rich black shale carbon powder on the basis of EDX analysis.

Figure 6.5 Protocol for the synthesis graphitic layers/Cu.

Figure 6.6 XRD patterns of the natural rich black shale carbon powder.

Figure 6.7 SEM image of the central region of the BC6 sample and EDX spectrum and relevant composition on black grain (A) and clear grain (B).

Figure 6.8 HRSEM micrographs on the natural organic matter rich black carbon powder with different magnifications.

Figure 6.9 HRSEM micrograph of graphitic layers/Cu substrate at 800 °C from drill core organic matter rich black shale carbon powder.

Figure 6.10 Raman spectra recorded on the black shale carbon sample.

Figure 6.11 Raman spectrum of natural black shale carbon powder.

Figure 6.12 Raman spectrum of graphitic layers deposited over Cu.

Figure 6.13 Raman spectrum comparisons of natural black shale carbon powder and the graphitic layers/Cu.

Figure 6.14 FTIR spectrum of BC4-106.80m powder.

Chapter 7:

Fig. 7.1 Raman spectra recorded on the SiOC and Si(B)OC powders pyrolyzed at: (A) 1200 °C and (B) 1400 °C.

LIST OF ABBREVIATIONS

Abbreviation	Particulars
nm	Nanometer
μm	Micrometer
FT-IR	Fourier Transform Infra-Red
HRSEM	High Resolution Scanning Electron Microscope
ESEM	Environmental Scanning Electron Microscope
XRD	X-rays Diffraction
CNT	Carbon Nanotube
MWCNT	Multi Walled Carbon Nanotube
SWCNT	Single Walled Carbon Nanotube
CS	Carbon Sphere
FPD	Flat Panel Display
UV	Ultra-Violet

CHAPTER: 1

State of the art about carbon nanostructures and natural materials as catalysts: historical background, definition, and their potential applications

1.1 Introduction

The novelty of the low dimensional nanomaterials brings the rapid growth in the area of nanomaterials. Evolving the controllable production and commercial applications of nanomaterials for sustainable society are of high concern. Herein, carbon nanostructures such as carbon nanotubes (CNTs)/ carbon nanofibers (CNFs)/ carbon nanopearls (CNPs)/ carbon spheres (CSs) with sp^2 carbon bonding, excellent mechanical, electrical, thermal, as well as transport properties are model nanomaterials to demonstrate the road of nanomaterials towards industry. The mass production of nano carbon has always been a matter of unease for its majority application for nanocomposites and energy storage.

The basic knowledge of growth mechanisms, efficient and controllable routes for carbon nanomaterials production, the environmental and safety issues, and the commercialization models are still inadequate. The gap between the basic scientific research and industrial development should be connected by multidisciplinary scientific research for the rapid and mass growth of nano carbon industry.

In this chapter we aim to focus on the background of the subsequent carbon and the natural materials, in which the nature of their sub materials will be discussed in details. It will be appropriate to consider the classification and structural information of carbon nanomaterials as well of the natural materials. The regularly used metal-based catalysts show good performance, however, they have some problems; (i) it is expensive because they consist of rare metals, (ii) metal particles on the catalysts should be nanosized and a lot of processes are needed such as impregnation, drying, and calcination, and (iii) when carbon is

deposited on the surface of the catalysts, the catalytic performance decreases and they cannot be used anymore.

We have been focused on the synthesis of carbon nanomaterials using low Ni containing iron laterite ores, siliceous breccia, as a catalyst and black carbon powder as a precursor. Further, we have been concerned in details with the literature related to the growth of carbon nanomaterials using natural mineral oxides. The phenomenological aspects about them are reported below.

1.2 Carbon Materials and their classifications

Carbon, is one of the important elements, and is the strategic element for a large variety of condensed matter systems. Pure carbon materials have always been interested for the scientist community. Carbon exists in various polymorphic forms, and can show sp^1 , sp^2 or sp^3 hybridization. Although, it is very difficult to classify the pure carbon materials. In fact, graphite, one of the carbon forms, consists of a layered structure while the crystal structure of diamond, another carbon form, is similar to that of zinc blende. In this section, we shall explain the classification of various carbon materials and its present research interest to the scientific world.

1.2.1 Diamond

Diamond, is an attractive material for its exquisiteness and properties. At room temperature and atmospheric pressure, it is a metastable carbon polymorph. Its crystal structure is known as the diamond cubic crystal structure. (Figure 1.1) The physical properties of diamond make this material an extremely attractive. It is the hardest known material, has a very low electrical conductivity, and before CNTs discovery/synthesis, diamond was known to be the best thermal conductors; these characteristics are due to its crystal structure and the strong interatomic covalent bonding. Due to its physical and mechanical properties, diamond fascinates the scientists for many research areas.

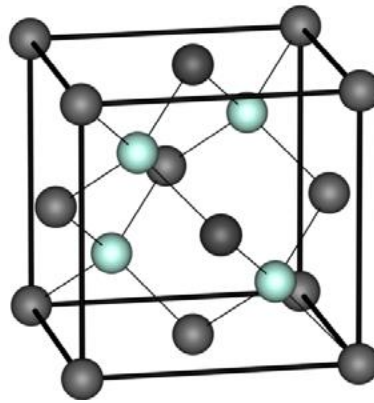


Figure 1.1 Unit cell of diamond.

The diamond films, synthesized via CVD, have polycrystalline structure and it may consist of very small and/or relatively large grains; in addition, amorphous carbon and graphite may also be present. The mechanical, electrical, and optical properties of diamond films reach those of the bulk diamond material. These properties have to be continued to be exploited for the production of better products. For example, the surfaces of drills, dies, bearing surfaces, knives, and other tools have been coated with diamond films to escalate the surface hardness; some lenses have been made tougher while remaining transparent by applying the diamond coatings. Potential applications for these films include surface coating of machine components such as gears and bearings, as well as of semiconductor devices, etc. [1].

1.2.2 Graphite

Graphite is a another polymorph of carbon; is also more stable than diamond at ambient temperature and pressure as well as it has a crystal structure distinctly different from that of diamond. The structure of graphite is composed of hexagonally arranged carbon atom layers; within the layers, each carbon atom is bonded to three coplanar neighbouring atoms through strong covalent bonds. The fourth bonding electron joins in a weak van der Waals type of bond between the layers. As a result of these weak inter-planar bonds, inter-planar cleavage is facile, which gives excellent lubricative properties of graphite. Furthermore, in crystallographic directions parallel to the hexagonal sheets, the electrical conductivity is relatively high. High strength and good chemical and mechanical

stability at elevated temperatures, low coefficient of thermal expansion, high thermal conductivity and high resistance to thermal shock, high adsorption of gases, are some other important properties of graphite.

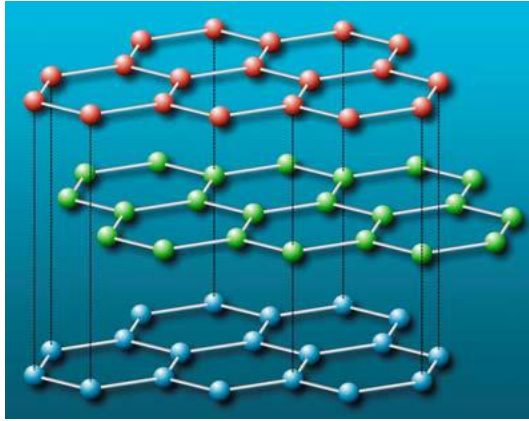


Figure 1.2 Structure of graphite.

Graphite is regularly used as heating elements for electric furnaces, in metallurgical crucibles, for high-temperature refractories and insulations, as electrodes for arc welding, , in casting moulds for metal alloys and ceramics, in rocket nozzles, in chemical reactor vessels, as electrodes in batteries, and in air purification devices. [1]

1.2.3 Fullerene

As polymorphic form of carbon, fullerene has been a newly discovered material, in 1985 [2]. In 1985, Harry Kroto of the University of Sussex in England and a team at Rice University, Texas, led by Richard Smalley, discovered C₆₀ (buckminsterfullerene) molecule while experimenting a laser ablation system for the vaporization of graphite by laser beams and depositing them on a copper substrate [2]. For this, in 1996 Nobel Prize in chemistry was awarded to Smalley, Kroto and colleague Robert Curl. As that carbon atoms could conglomerate spontaneously into this complicated structure was astonishing, and the new perspectives were opened up. But until 1990, not enough investigations were made of it to study it properly or do anything useful with it and by that time researchers at Heidelberg in Germany and Tucson in the USA reported a method for producing large quantities of the C₆₀ molecule known as arc discharge

method [3]. Discovery of this material has shown that the formation of extraordinary structures which carbon is capable of. Fullerene exists in discrete molecular form, and consists of a hollow spherical cluster of 60 carbon atoms; a single molecule is symbolized as C₆₀. Individual molecule is composed of groups of carbon atoms that are bonded together to form both hexagon (six-carbon atom) and pentagon (five-carbon atom) configurations. (Figure 1.3) One such molecule consists of 20 hexagons and 12 pentagons, which are arrayed such that no two pentagons share a common side. The structure of a C₆₀ molecule is known as Buckminsterfullerene, named in honour of R. Buckminster Fuller, who invented the geodesic dome; each C₆₀ is basically a molecular facsimile of such a dome, which is often referred to as "buckyball" in short [1].

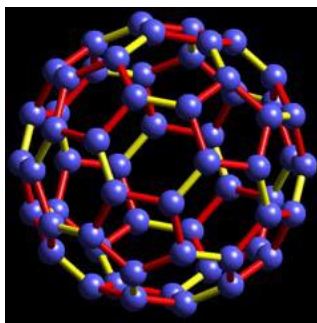


Figure 1.3 Buckminsterfullerene (C₆₀) molecule.

1.2.4 Carbon Nanotubes

1.2.4.1 Discovery

In the 1970's and 1980's, very small diameter (< 10 nm) carbon filaments were prepared through the synthesis of vapour grown fibers by the decomposition of hydrocarbons at high temperatures using transition metal catalyst particles of <10 nm diameter. However, in these early years, no detailed systematic studies of such very thin filaments were reported.

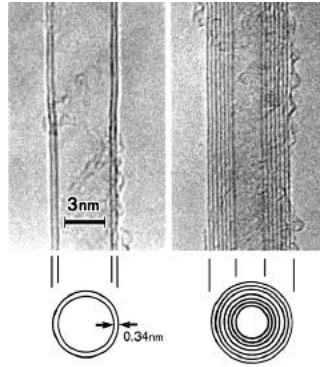


Figure 1.4 High Resolution Transmission Electron Microscope (HRTEM) image of first observed MWCNTs by Iijima in 1991[4].

In 1991, Iijima experimented with the arc discharge method that had enabled the scientists working on C₆₀ to produce their new form of carbon in large quantities. Iijima, by passing electrical sparks between two closely spaced graphite rods was able to condense the vaporized carbon atoms in a sooty mass. But upon looking the soot through the microscope, he found something altogether unexpected. Amongst the debris, C₆₀, there were tiny tubes of pure carbon, just of few nanometers in diameter. These 'nanotubes' were hollow and multi layered: tubes inside tubes, similar to the nested Russian dolls (figures 1.4 - 1.5), their ends were sealed with conical caps [4]. These CNTs are called multi-walled carbon nanotubes (MWCNTs). However, in 1993, nearly at the same time Bethune et al. [5] and Iijima et al. [6] reported that single-walled carbon nanotubes (SWCNT) (figure 1.6) have been produced using metal catalysts (Co) through an arc discharge system. In 1999 Iijima et al. reported a new kind of SWCNT called nanohorn that is SWCNT with conical tube ends (figure 1.7) [7].

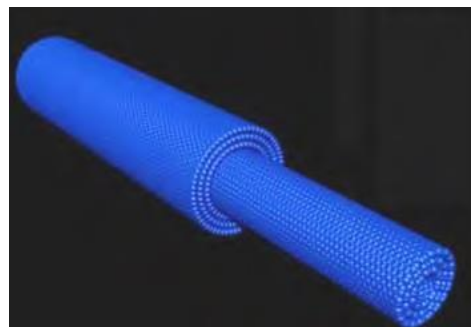


Figure 1.5 Computer generated image of a multi-walled carbon nanotube (MWCNT).

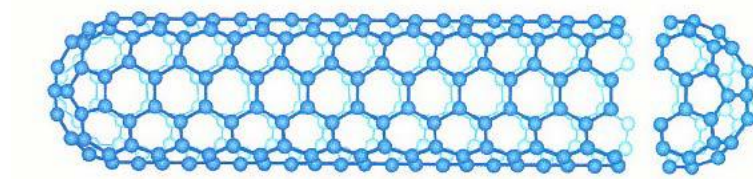


Figure 1.6 Computer generated image of a single-walled carbon nanotubes (SWCNTs).

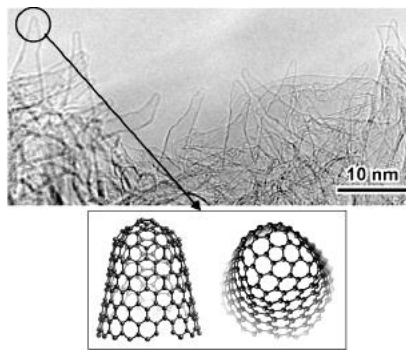


Figure 1.7 HRTEM (top) [7] and computer generated (bottom) images of SWCNTs [8].

1.2.4.2 Structure

The easiest way to record the structure of carbon nanotubes is to study the conformal mapping of a finite number of two-dimensional (2D) layers of graphite sheet (graphene layers) onto themselves. Generally, two different types of nanotubes exist, depending upon whether the tube walls are made of one layer (graphene tubes) or more than one layer (graphitic tubes) [9]. The graphitic nanotubes are known as multishell or multiwalled carbon nanotubes consist of two or more concentric cylindrical shells of graphene sheets coaxially arranged around a central hollow, like Russian dolls, with a constant separation between the layers which is nearly equal to that of the graphite layer spacing (0.34 nm; about 3-5% larger than single-crystal graphite spacing) [8]. These usually have diameters ranging from 2–25 nm and lengths reaching up to several microns. The second kind consists of tubes made of single layers of graphene cylinders with a very narrow distribution in size range (0.7-2 nm) and lengths extending up to several microns. Due to rotational disorder between layers and topology, the interlayer correlations that give anisotropic physical properties to graphite is clearly absent in the single-wall nanotubes (they are also mostly absent in multi-wall tubes) but this is not so obvious as isolated graphene layers make up the

tubes. A single-wall nanotube can be considered in close correspondence to a large fullerene molecule (closest is a C₂₄₀ with a diameter of about 1.2 nm) which has been bisected, separated and joined with a tube 1 monolayer thick and having a similar diameter. However, both single and multi-wall nanotubes ensure the physical characteristics of solids, and must be understood as micro crystals and not as molecular species. Though they have different chain lengths but they are resonant of typical chain polymerization reactions resulting in large molecular-weight structures. From a different point of view, carbon nanotubes are closely related to certain types of carbon nanofibers which also have a similar cylindrical layered structure but the CNTs are much more faultless. As the SWCNTs contain all of the in-plane graphite strength, it can be supposed of as the ultimate carbon fiber of molecular dimensions [9].

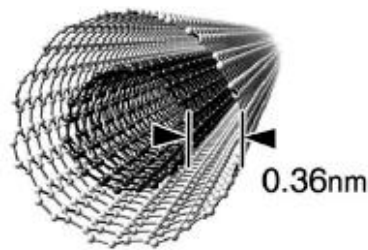


Figure 1.8 Distance between two nanotubes of MWCNTs is nearly same as the interlayer distance of graphite [7].

1.2.4.3 Classification of carbon nanotubes

The structure of CNTs has been sightseen and recorded via high resolution TEM and Scanning Tunneling Microscopy (STM) techniques (Figure 1.9), yielding direct confirmation that the nanotubes are seamless cylinders derived from nearly 0.34 nm honeycomb lattice representing a single atomic layer of crystalline graphite, called a graphene sheet, (Figure 1.10). Generally, the diameter of a SWCNTs about 0.7–10.0 nm, though most of the observed single-walled nanotubes have diameters less than 2 nm [10]. If the two ends of CNTs are neglected and focusing on the large aspect ratio of the cylinders (i.e., length/diameter), these nanotubes can be deliberated as one-dimensional nanostructures.

A remarkable and important fact about the CNT structure is the orientation of the six-membered carbon ring (hexagon) in the honeycomb lattice relative to the axis of the nanotube. Three examples of SWCNTs are presented in figure 1.11. From this figure, it can be perceived that the direction of the 6-membered ring in the honeycomb lattice, except for the distortion due to the curvature of the carbon nanotube, can be taken almost arbitrarily, without any distortion of the hexagons. This information provides many possible structures for CNTs, even though the basic shape of the CNT wall is a cylinder. In figure 1.11, the ends of each of the three CNTs are also shown. The ends are frequently called caps or end caps and consist of a "hemisphere" of a fullerene. Each cap contains 6 pentagons and an appropriate number and placement of hexagons that are selected to fit perfectly to the long cylindrical section.

The primary symmetric classification of a carbon nanotube is as either being an achiral or a chiral. An achiral carbon nanotube is defined by a carbon nanotube whose mirror image has a similar structure to the original one. There are only two cases of achiral nanotubes; armchair and zigzag nanotubes, as shown in figure 1.11 (a) and (b), respectively. The names of armchair and zigzag arise from the shape of the cross-sectional ring, as is shown at the edge of the nanotubes in figure 1.11 (a) and (b), respectively. Chiral nanotubes reveal a spiral symmetry whose mirror image cannot be superposed on to the original one. This tube is called a chiral nanotube, since such structures are called axially chiral in the chemical nomenclature [10].

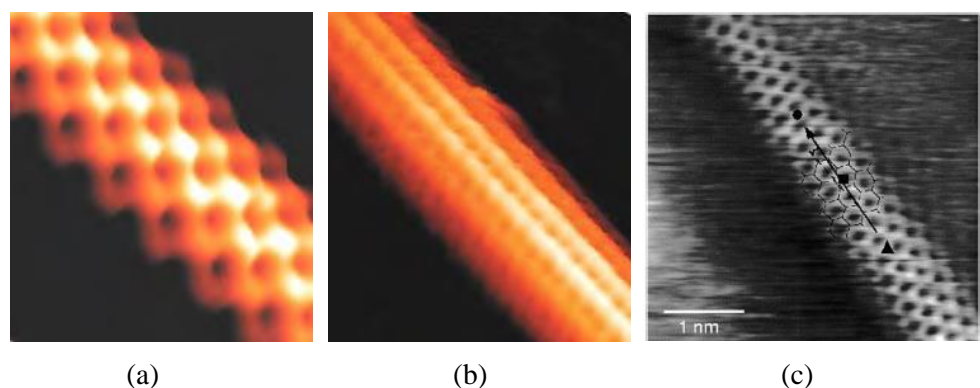


Figure 1.9 STM images of carbon nanotubes (a), (c) zigzag [11], and (b) armchair.

The structure of a SWCNT is conveniently explained in terms of its one dimensional (1D) unit cell, defined by the vectors C_h and T in figure 1.10 (a). The circumference of any CNT is stated in terms of the chiral vector $C_h = na_1 + ma_2$ which connect two crystallographic equivalent sites on a 2D graphene sheet (Figure. 1.10 (a)). The construction in Figure 1.10 (a) depends exclusively only on the pair of integers (n, m) which stipulate the chiral vector. Figure 1.10 (a) illustrate the chiral angle θ between the chiral vector C_h and the "zigzag" direction ($\theta = 0$) and the unit vectors a_1 and a_2 of the hexagonal honeycomb lattice of the graphene sheet.

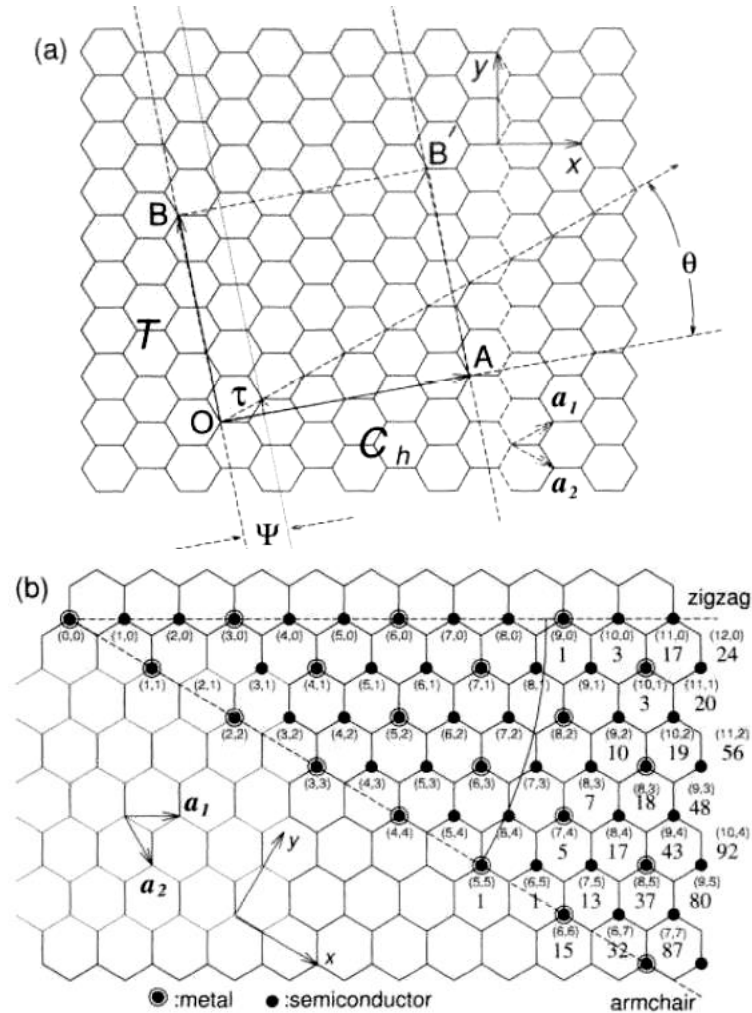


Figure 1.10 (a) The chiral vector OA or $C_h = na_1 + ma_2$ is defined on the honeycomb lattice of carbon atoms by unit vectors a_1 and a_2 and the chiral angle θ with respect to the zigzag axis. Along the zigzag axis $\theta = 0^\circ$. Also shown are the lattice vector $OB = T$ of the

1D nanotube unit cell and the rotation angle ψ and the translation τ which constitute the basic symmetry operation $R = (\psi | \tau)$ for the carbon nanotube. The diagram is constructed for $(n, m) = (4, 2)$. (b) Possible vectors specified by the pairs of integers (n, m) for general carbon nanotubes, including zigzag, armchair, and chiral nanotubes. Below each pair of integers (n, m) is listed the number of distinct caps that can be joined continuously to the carbon nanotube denoted by (n, m) . The encircled dots denote metallic nanotubes while the small dots are for semiconducting nanotubes [9].

Three distinct types of carbon nanotube structures can be produced by rolling up the graphene sheet into a cylinder as described below and shown in Figure 1.11. The zigzag and armchair nanotubes, respectively, correspond to chiral angles of $\theta = 0$ and 30° , and chiral nanotubes correspond to $0 < \theta < 30^\circ$. The intersection of the vector OB (which is normal to C_h) with the first lattice point determines the fundamental one-dimensional (1D) translation vector T . The unit cell of the 1D lattice is the rectangle denned by the vectors C_h and T (figure 1.10 (a)) [9].

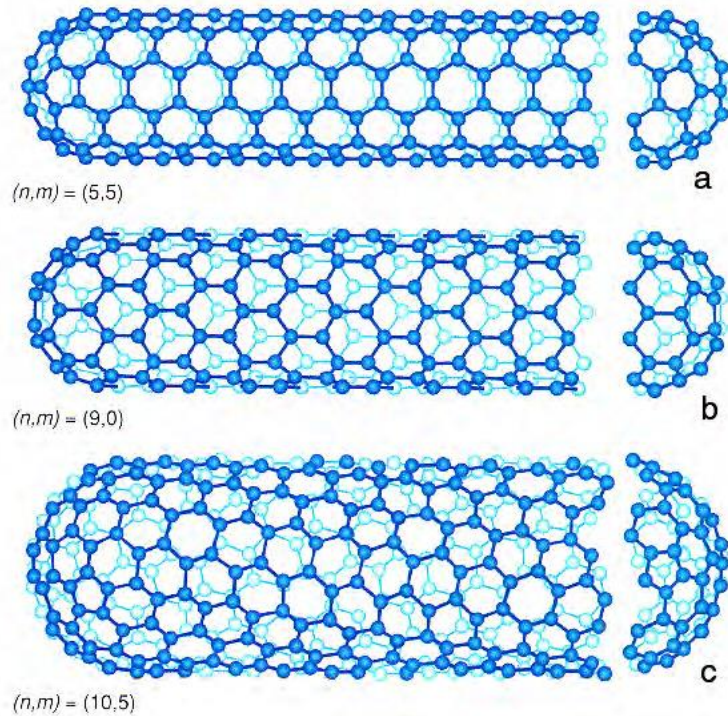


Figure 1.11 Classification of carbon nanotubes: (a) armchair, (b) zigzag, and (c) chiral nanotubes. From the figure it can be seen that the orientation of the six membered ring in the honeycomb lattice relative to the axis of the nanotube can be taken almost arbitrarily.

1.2.5 Carbon Nanopearls

The carbon nanopearl term was coined by a team of researchers at the University of Lyon in 2004. However, carbon nanopearls are similar to the carbon nanospheres that have been studied for quite some time. The only major difference is the synthesis methods used and the diameter sizes. As mentioned earlier, these carbon spheres of graphene flakes are reported to have diameter sizes ranging from 60-2000 nm [2,4,12–17]. Carbon nanopearls are demarcated as monodisperse nanospheres of nanocrystalline carbon that form a three dimensional (3D) arrangement analogous to a string of pearls (figure 1.12) [16]. These sp^2 hybridized carbon spheres are made up of 2D concentrically-oriented nano-sized graphitic flakes (figure 1.13).

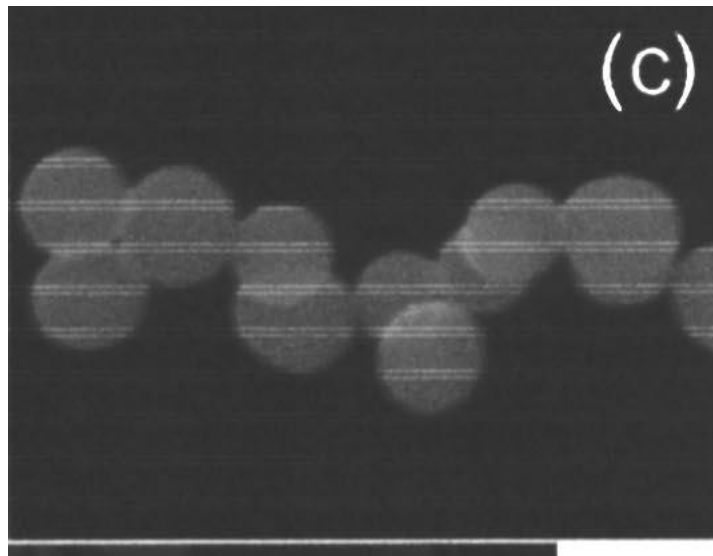


Figure 1.12: TEM image of carbon nanopearl illustrating 3D arrangement of carbon nanopearls [16].

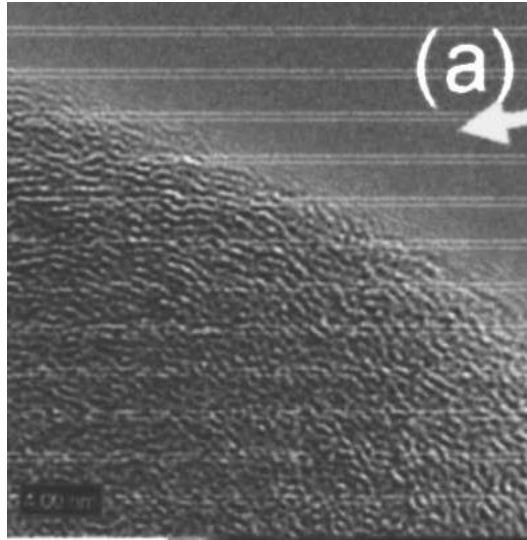


Figure 1.13 HRTEM image of carbon nanopearls having concentrically-oriented nano-sized graphitic flakes [16].

A. Levesque et al., describes carbon nanopearls synthesis process: upon decomposition of acetylene gas into atomic carbon (figure 1.14), a wavy 2D structure of graphene flakes are formed, and the flakes are clustered together in the layered formation manner resulting a spherical shape [16]. As Reported, these 2D flakes are of around 4 nm in diameter size (figure 1.14). Furthermore, it is reported that there are some amorphous areas are also present between the layered flakes. Levesque et al., further propose that the spherical shape is derived from the combination of pentagonal and heptagonal rings having a planar hexagonal structure, which make up the wavy two dimensional spherical flakes.

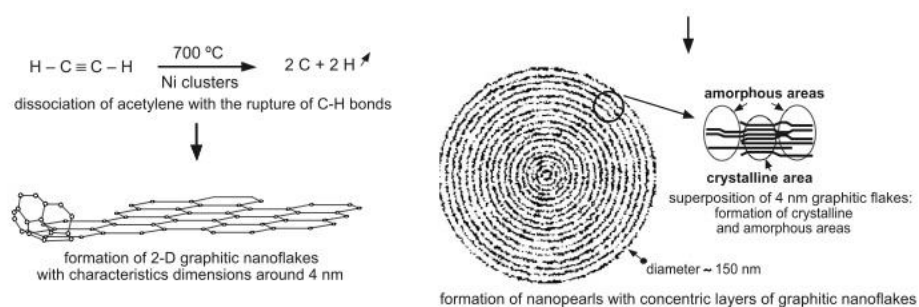


Figure 1.14: A diagram of the theoretical synthesis process of carbon nanopearls [16].

The structure of each graphitic flake (assembling up the sphere) consists of graphitic carbon rings (e.g., hexagon, pentagon, and heptagon), and the curvature of the sphere is due to the modulation of the graphitic lattice (see figure 1.15 for graphitic rings) [18]. Hexagonal carbon rings results in making a flat sheet (i.e., graphene). The inward curve ($+60^\circ$), is forced by pentagonal rings on the hexagonal rings. Heptagonal rings do the reverse of pentagonal rings. The heptagonal rings force the hexagonal lattice to curve outward (-60°). If there were no heptagonal carbon rings present, the pentagonal carbon rings would form a faceted polyhedron [18]. As a result, the presence of both a pentagonal and heptagonal ring in a hexagonal lattice results in a carbon sphere, with a reduction in the curvature of the structure. There are 12 pentagonal carbon rings required to form a closed structure (without the presence of heptagonal and octagonal rings) [19, 20].

If there are heptagons rings present (in the case of the carbon nanopearls), this number of pentagons require changes. For each heptagon, an extra pentagon is needed to close the structure [18]. The more heptagons, the more pentagons (twice as many), which results to an increase in the overall diameter size of the sphere.

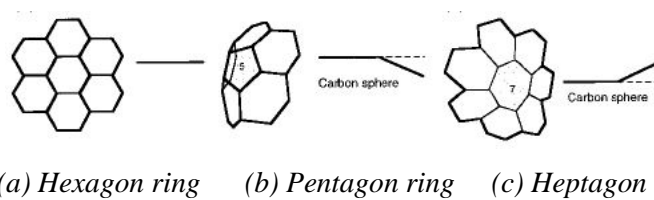


Figure 1.15 (a) Hexagon ring carbon structure with zero curvature, (b) pentagon ring structure with curvature around $+60^\circ$, (c) heptagon ring structure with outward curvature around -60° [18].

According to Wang et al., this growth process is ideal for all carbon nanospheres (regardless of the growth method). As mentioned, carbon nanopearls can be synthesised using various methods. Some of these methods include: growth from glucose using hydrothermal conditions [12], non-catalytic chemical vapour deposition (CVD) preparation [13], de-oiled asphalt [14], direct pyrolysis of hydrocarbons [15], arc discharge and autoclave methods [21], and CVD growth of

carbon nanopearls using Ni catalyst [16]. The chemical vapour deposition process has been extensively explained in chapter 2. A. Levesque et al. reported the use of CVD technique for carbon nanopearls synthesis. In their experimental process, they used Ni catalyst 100 nm in size, a gas mixture of 20 % C_2H_2 / 80 % N_2 at a flow rate of 80:400 sccm (respectively), and a growth temperature of 700 °C. As a result, the authors report carbon nanopearls having a diameter size of 150 nm (figure 1.16). Carbon nanopearls that have been synthesised using other methods have different sizes. For example, He et al; used the arc discharge method to grow what they referred to as carbon balls [47]. In their setup [47], the anode was a carbon rod having both Fe and Ni, and the graphitic rod as cathode. They reported sphere diameter sizes that were between 50-100 nm. Carbon spheres have also been produced by carbonization of acetone at 550 °C, on Ni foil, in an autoclave [21]. These spheres were reported to be 4–5 μm (figure 1.17).



Figure 1.16: HRSEM image of carbon nanopearls via CVD process [7].

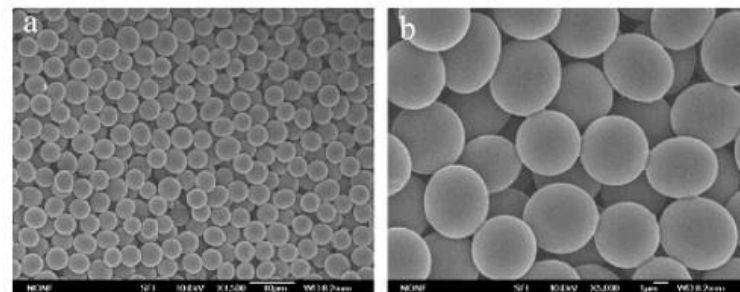


Figure 1.17: Carbon nanopearls grown over a Ni foil catalyst, using autoclave process [21].

CNPs demonstrate field emission properties that would be ideal for cathode materials [22]. The small radius of curvature (~ 75 nm), and the dangling bonds from the unclosed graphitic flakes, makes carbon nanopearls appealing applicant for the cathode materials. When compared to CNTs, CNPs are better for cathode materials as a result of there being no requirement for structural orientation. A. Levesque et al; reported field emission results of carbon nanopearls. Their measurements data shows carbon nanopearls obtained currents up to $50 \mu\text{A}$ under continuous emission (see figure 1.18 for Levesque et al., field emission results) [16].

Apart from, CNPs field emission properties, recently there have been reports supporting evidence of CNPs as potential tribological coatings and lubricant additives [22]. There has also been some research being done on CNPs as potential transporters of proteins, nucleic acids, and drug molecules in the nuclear membrane and across the cell membrane [23].

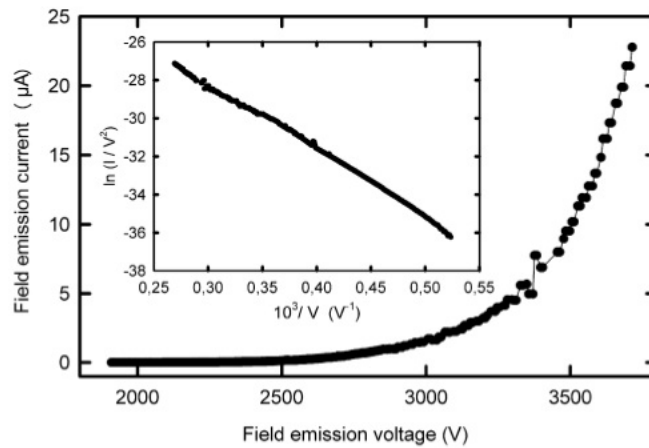


Figure 1.18: Field emission data taken from CNPs [16].

1.2.5.1 Difference between carbon nanopearls and other carbon structures

There are a few variances between carbon nanopearls and other carbon structures (such as graphene, buckyballs, carbon nanotubes and carbon nano-onions). These differences are found basically in structure and properties. Carbon nanopearls have a spherical structure, consists of hexagonal sheets with pentagonal and heptagonal rings (to permit bending of the structure). Like CNPs, carbon nano-onions are also spherical. However, carbon nano-onions have multiple “buckyball like” spheres. Their structure consists of pentagons and

hexagons only and not heptagonal. Carbon nano-onions are frequently referred to as multiple buckyballs. Carbon nanotubes have a cylindrical structure, consisting of single or multiple layered graphene sheets. CNTs are field emitters; however, they are restricted to emitting from the end of the tube. However, carbon nanopearls are not dimension restricted when used as field emitters.

1.2.6 Carbon Spheres

A wide variety of carbon spheres, CSs have been synthesized and a brief summary morphology of the spheres is much needed. The diameter sizes of CSs are known to range from a few nanometers (as found in onions) to many microns (as synthesised by polymerization reactions). In most instances in a synthesis procedure a wide range of diameters are produced and it is becoming more general to demonstrate this in literature reports in terms of bar graphs or by a statement about the sphere diameters and their standard deviation. The surface areas of CSs fluctuate from very low values ($<2 \text{ m}^2\text{g}^{-1}$) to very high ones ($>1200 \text{ m}^2\text{g}^{-1}$). These values can be made-to-order by the synthesis procedures with hard spheres being associated with low surface area carbons.

The less in diameter size CSs, typically made by CVD procedures, generally are found in necklace form, i.e. the spheres are linked together typically in a 2D strand that can extend over tens of spheres (figure 1.19). It seems that the sphere linkages appear early in the synthesis process and implicate the graphite layers encapsulating spheres in the necklace. Thus, the spheres are chemically linked together. Larger spheres generally form as discrete carbon structures that can interact with other spheres through van der Waals bonding.

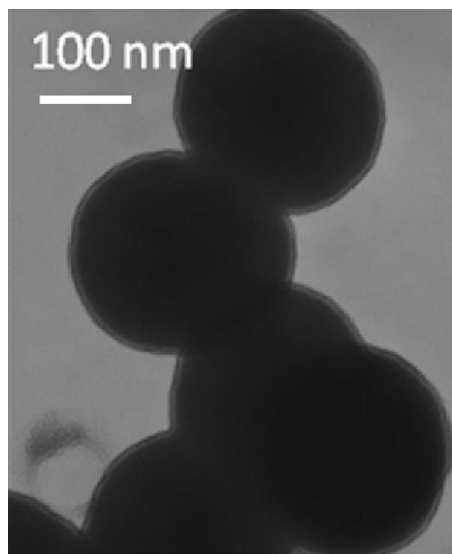


Figure 1.19 A TEM image of CSs that have aggregated to form a necklace

Figure 1.20 depicts the effect of heating the discrete carbon spheres (a) to form amalgamated structures via sphere coalescence (b) that can occur at high temperatures. Indeed, it has been shown that when carbon balls (CBs) are used as an electrode in an arc discharge reaction that the spheres accrete at high temperature to eventually form MWCNTs [24]. A model involving defects and heptagon/pentagon structures was used to explicate the transformation. Theoretical and experimental investigations on spherical objects that form accreted structures have recently been reported. These studies suggest that carbon necklaces could be produced with specific geometries and sizes (Fig. 1.20) [25].

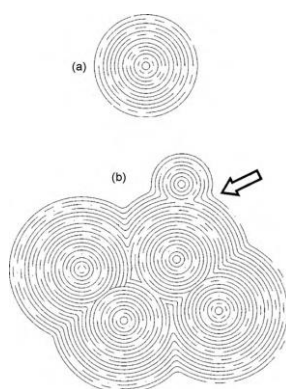


Figure 1.20 Schematic representation of carbon black. (a) Carbon onion like structure; (b) aggregate of carbon-onion like structures (arrow indicates 'neck' between carbononions)[24].

Random orientation Concentric orientation Radial orientation



Figure. 1.21 Sketch indicating radial, concentric and random carbon layer orientations in CSs.

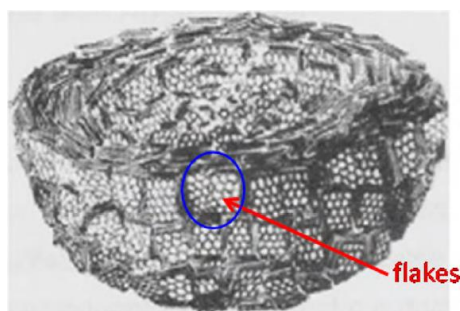


Figure. 1.22 Model showing cutaway of a single carbon black particle with concentric layers. Parallel orientation of ordered layer groupings and diminishing graphitic order near particle center [26].

As mentioned above spheres can be formed with their carbon chains/layers/flakes perpendicular or parallel to the carbon core (figure 1.21). The arrangement of the layers has a major influence on the chemical and physical properties of the CSs. Diagram showing the carbon flakes arranged parallel to the carbon core is shown in figure 1.22 [26]. The flakes typically have diameter sizes in the range of 2–10 nm. The size of the flakes can be determined by TEM or XRD studies. Pyrolysis of the CSs generates a more graphitic structure in which the flakes grow in size with hollow and filled spheres. Hollow spheres can be made by a number of standard approaches, the most popular being a templating process. In the template procedure a spherical material is covered by a carbon containing material that is permitted to self-assemble and following C–C bond formation on the surface of the sphere a filled core–shell structure is synthesized. The interior of the sphere can have materials that have properties that may be exploited. For example, if the core is made of a magnetic material then magnetic fields can be used to manipulate the CSs [27, 28].

Alternatively, the core can be detached, usually thermally, to generate a hollow sphere. The template is hence foregone in the synthesis. Polyelectrolyte capsules and related materials also consent for synthesis of hollow spheres, but in this synthesis method growth within the cavity rather than in the shell to give parachute like morphologies takes place [29].

1.3 Natural Materials as Catalysts for Nano Carbon Synthesis

The mass production of CNTs in a fluidized-bed reactor is a complex route, from the precise catalyst control at the atomic level and CNT agglomerate growth at the mesoscopic scale to the continuous mass-production process on a macroscopic scale [30]. Atomic-scale catalyst design can control and modulate the structure of CNTs and other carbons nanostructures. For mass production, the catalyst is considered as the most key factor for growth of CNTs. The transition metals, Fe, Co, Ni, V, Mo, La, Pt, and Y, are active for CNT synthesis and production [31]. These active metal elements can be loaded onto a catalyst carrier (mostly alumina, which is commercially available) by impregnation, co-precipitation, and by other loading methods widely used in petroleum and chemical processes.

These metal particles are then activated by calcination and reduction procedures before or during CVD treatment. The resulting metal nanoparticles are the catalytically active species, functioning simultaneously as activators for hydrocarbon deposition and as structural patterns for the resulting carbon nanomaterials [32]. Any effective mass production process that leads to a large drop in costs of production will lead to a breakthrough of CNT applications. Investigations and studies into new inexpensive feedstocks as well as more efficient catalyst/ support combinations suitable for the mass production of CNTs are required by keeping in mind the today's scenario of dependency of human kind on the nanoscience and advanced technologies.

Metals or metal oxides, in small or even trace amounts, can be easily found in nearly all natural materials even in plants or biomass. These metals or metal oxides are commonly present in the form of small natural nanoscale material particles which makes them as the ideal form for use as catalysts for CNT

synthesis. Humankind has been using the natural materials for their needs and requirements since its existence. The inhomogeneous distribution of natural materials on this planet allows us to use them for the desirable needs and requirements for applications for the betterment of humankind. Further, use of natural materials in the production of nanoscience and nanotechnology could play a vital role in the coming years.

There are enormous amounts of natural materials, such as rocks and stones, literally lying around that could be useful in nanoscience and nanotechnology. This is reported in numerous recent studies in which natural minerals are used as catalyst and support for the synthesis of CNTs and carbon nanofibers (CNFs), which are the topics discussed in well detail in this chapter. Many minerals have a layered structure with unit layers very thin nearly as 1 nm and sizes ranging from several nanometres to several micrometres. For case in point, clay which is a natural product can be found and obtained in large amounts at very low cost and is been used for a wide range of applications. Clay which has large surface area, strong acidity, and strong adsorption and ion-exchange ability, thus because of this, it has been used as a catalytic support for the synthesis of CNTs by CVD, which has demonstrated to be a cost efficient way of mass-producing CNTs [33].

There have been reports in which researchers used the natural materials as a catalyst for the synthesis of nano carbon. As reported, nano carbon was synthesised using Mount Etna lava as a catalyst and support [34], further the same group of researchers has tried to use red soil as a catalyst and support for the synthesis of nano carbons and was used as carbon source for the CNT growth through a CVD process [35].

Further, Garnet which is a naturally occurring gem mineral with uniform physical, chemical, and microstructural properties was also tried by Endo and his group and used garnet sand pulverized from natural garnet stones (Ube Sand Kogyo, 1.4 \$ US dollars per kg), as a catalyst and support for the synthesis of MCNTs [36].

Bentonite which is an absorbent aluminium phyllosilicate, which is an impure clay consisting mostly of montmorillonite. Rinaldi et al. used bentonite

(Winston Company, Germany, sold as Katzenstreu, cat sand) as a support and catalyst for the production of CNTs [37].

Natural minerals such as forsterite, diopside, silica, magnesite, and brucite have also been used as catalysts and supports for the synthesis of single-walled carbon nanotubes (SWCNTs) [38]. In an investigation, to know whether SWCNTs can be formed in nature through geophysical process, Kawasaki et al. demonstrated that SWCNTs can grow on magnesite crystals by pyrolysis of methane [38]. They cast-off five crystal samples of natural minerals in the experiments: forsterite (USA), diopside (Pakistan), quartz (Japan), magnesite (Brazil), and brucite (USA). Forsterite and diopside are very common magnesium silicates. Forsterite characterizes the Mg end-member of the olivine group, and diopside is a Ca-Mg pyroxene ($\text{CaMgSi}_2\text{O}_6$). Quartz is one of the polymorphs of SiO_2 . Magnesite (MgCO_3) and brucite ($\text{Mg}(\text{OH})_2$) were used as potential sources for the formation of the MgO mineral phase. X-ray fluorescence (XRF) measurements confirmed Fe to be a major impurity in all samples [38]. The mineral samples were crushed in an agate mortar and the obtained powder was used for the CVD process. Methane gas diluted with argon was used as the carbon source for the decomposition. After CVD treatment, only a small amount of amorphous carbon was deposited on the forsterite, diopside, and quartz samples. In the case of the magnesite sample, however, SWCNTs with diameters of about 1.0–1.8 nm were achieved. Typically, the tubes form bundles with diameters sizes in the range of 5–20 nm. Double-walled CNTs were also observed inside the bundles. SWCNTs could also be grown on natural brucite. The high quality of the SWCNT product was confirmed by micro Raman spectroscopy and thermogravimetric experiments [38]. While it could be expected that no CNTs could be grown on quartz, because of the insufficient Fe content, it was surprising that in this work forsterite and diopside could not catalyse the growth of CNTs, even after having high concentrations of iron. One explanation could be that the Fe species in these two minerals are not accessible to the hydrocarbon during the CVD process. Because SWCNTs have only one wall and require smaller particles of the catalyst rather than MWCNTs, it seems that the trace amounts of Fe in magnesite and brucite allow the formation of small catalyst particles that catalyse

the growth of SWCNTs on them. If the trace amounts of metal in natural minerals are too small to be used for carbon nanomaterials growth, they can be used as a catalyst support. Catalysts can be mixed to enhance or to primarily lead the CVD process. For example, clay minerals are hydrous alumino–silicates and are mostly classified as phyllosilicates, or layered silicates, while they also comprise other minerals that impart plasticity to clay, and which harden upon drying and thermal treatment [39]. Phyllosilicates is made of a combination of tetrahedral and octahedral sheets [39]. Si atom in silicates coordinates four oxygen atoms to the tetrahedron plane. Cation substitutions in tetrahedron plane are limited to Al, Fe³⁺, and Ti⁴⁺. In the phyllosilicates, the substitution of Al for the Si in the tetrahedron is necessary for the charge balance of the mineral. Equally in the octahedral where the Mg or Al are present, there may be different cationic substitutions such as Fe²⁺, Fe³⁺, Ti⁴⁺, etc. The tetrahedron (T) and octahedrons (O) planes are the building units of the phyllosilicates and different stacking sequences of these layers can be found in the different types of phyllosilicates. The minerals of the clay have stacking sequence TOT (2:1). Intercalation of molecular species into layered inorganic clays produces ordered inorganic/organic assemblies with unique microstructure controls [40, 41]. Due to their unique swelling, ion-exchange, and intercalation properties clays can be easily, uniformly, and reproducibly loaded with metal ions or metal oxide clusters that function as catalysts for the growth of CNTs in high quantity.

Smectite clay (sodium-montmorillonite) from the island Milos (Greece) was primarily used by Gournis et al. for the synthesis of a novel clay-CNT hybrid by catalytic decomposition of hydrocarbon (acetylene) over iron-catalyst centers supported on the clay by Fe III ion-exchange [42]. This bring about tubes exhibited various orientation configurations and bridges between different clay platelets. The clay in the carbon-modified solid maintained its exchange properties, making the generation of valuable CNT–organic clay derivatives possible. Bakandritsos et al. optimized the process by an additional impregnation of Fe ion-exchanged smectite with altered amounts and types of metal salt catalyst precursors (FeCl₃·6H₂O, Fe(NO₃)₃·H₂O, Ni(NO₃)₂·6H₂O, and Co(NO₃)₂·6H₂O) [43]. Nitrate metal salts impregnated on montmorillonite as catalyst precursors

produced CNTs almost free of metal carbide impurities. Unfortunately, only unsystematic CNTs were produced on separated clay sheets and the periodic layer structure of the original substrate was completely gone astray. The effect of the nature of the catalytic centres and of the type of alumina-silicate layers in the morphology, quality, and structure on the final products was recently studied by Tsoufis et al. [44]. Different ionic forms of montmorillonite and laponite containing transition metals (Cr, Mn, Fe, Co, Ni, Cu, and Zn) were synthesised. The synthesis of carbon nanostructures was carried out at 700 °C using an acetylene/nitrogen mixture. Fe, Co, Ni, and Mg-exchanged clays showed to be effective catalysts for the production of CNTs, whereas acetylene decomposition over copper-exchanged clays resulted in the creation of carbon spheres. Chrome- and zinc-exchanged clay catalysts did not turn out/result in the formation of any graphitic deposits under the same reaction conditions.

Outstanding work has been reported to prepare hybrid composites consisting of alternating, vertically aligned CNTs between inorganic layers [45, 46]. Zhang et al. prepared metal catalysts by ion-exchange of iron into naturally existing layered vermiculites (from PR China). To increase the ion exchange, they initially exfoliated the vermiculites; the ion-intercalated vermiculites were dried at 110 °C for 12 h and calcined at 400 °C for 4 h. CVD growth was carried out using diluted ethylene as the carbon source in a quartz reactor at 650 °C. This method could be generalized to synthesize a family of CNT composites with similar structure using various catalytic ions (such as Ni, Co, and Cu), gas precursors (e.g., methane, ethylene, propylene, and liquefied petroleum gas), and layered compounds (e.g., mica and layered alumina) [45]. It is interesting annotation that the intercalated CNTs were vertically aligned. This phenomenon may be because of the unique chemical environment of the layered compounds. For example, vermiculite exhibits a high-ion exchange capability [46]. A higher number of the catalytic ions may be exchanged and absorbed within the layers, leading to a higher density of catalytic particles within the layers. A high density of catalytic particles generally supports the synchronous aligned CNTs growth [47]. The length and density of the aligned CNT arrays between the sheets can be controlled, which allows for a periodic and hierarchical macrostructure with

tailored interlayer distances. The CNT arrangements remains well-aligned even after vermiculite layers were removed by acid treatment [48].

In the work on the clay-CNT hybrids, the layered structures with enhanced ion-exchange properties, rather than trace metal content, are accountable for their performance. Therefore, the objective of using clays in the composites is not just to lower the CNT production costs, but also to use the unique structure characteristics of these natural inorganic compounds.

Clay is also widely used as a host material for organic species to transform into carbonaceous nanocomposites via thermal treatment [40, 41]. Polymer-clay and biopolymer-clay composites have been synthesized using contacting polymers, such as polyaniline (PANI) and polypyrrole (PPy), and using biopolymers, such as polysaccharides, polypeptides, proteins, and nucleic acids [49-55]. These types of polymer-clay composites have been used for many applications such as sensors or electrodes [54, 55].

Recent studies have shown that natural materials can be used for the synthesis of nanomaterials, aimed at developing low cost, environmental friendly and resource-saving processes for large-scale production. The presence of trace metals in natural materials is a pre-requisite for this development and it is clear that nearly ubiquitous rock, sand, mineral, and biomass materials should be explored as valuable catalytic materials for the rapid production of nanomaterials for the benefit of human kind.

1.4 Structural and vibrational spectroscopy characterizations of carbon nanostructures synthesized using mineral oxides: objective of present work.

The main objective of this project is to synthesize the carbon nanomaterial growth from natural geo-materials as catalyst/precursor using simple chemical vapour deposition technique and to investigate their vibrational properties. Another interesting part of this project is to explore the gross structural analysis, surface morphologies, and microstructural characterizations of these synthesised carbon nanostructures using XRD, SEM, and vibrational spectroscopic techniques.

Highlights of present investigations are listed below:

1. To investigate the scope of natural minerals, especially, low Ni containing iron ore, siliceous breccia and organic matter rich black carbon powders as a catalyst and precursor for the synthesis of carbon nanostructures.
2. To explore the existing mechanisms behind the growth of carbon nanostructures on naturally occurring geological minerals and find out the improved one to satisfy all the characteristics observed for carbon nanostructures growth.
3. To synthesize and characterize carbon nanostructures like MWCNTs, CNFs, carbon nanopearls, carbon nanospheres and graphitic layers.
4. To find out the effects of various technical parameters like use of flux, synthetic conditions (calcinations temperature, time, atmosphere etc.), for the better growth of carbon nanostructures.
5. To search the possibility of further growth of carbon nanostructures from other kind of natural minerals.
6. To explore the potential applications of the as synthesised carbon nanostructures.

1.5 References

1. D. William Callister, Jr, "Materials Science and Engineering: An Introduction", New York, John Wiley & Sons, 2002
2. H.W. Kroto, J.R. Heath, S.C. O'Brien, R.F. Curl, R.E. Smalley, *Nature*, 1985, 318, 162.
3. W. Krätschmer, L.D. Lamb, K. Fostiropoulos, D.R. Huffman, *Nature*, 1990, 347, 354.
4. S. Iijima, *Nature*, 1991, 354, 56.
5. D. S. Bethune, C. H. Klang, M. S. De Vries, G. Gorman, R. Savoy, J. Vazquez, R. Beyers, *Nature*, 1993, 363, 605.
6. S. Iijima, Ichihashi, T., *Nature*, 1993, 363, 603.
7. S. Iijima, *Chem. Phys. Lett.*, 1999, 309, 165.
8. S. Iijima, *Physica B*, 2002, 323, 1.
9. M.S. Dresselhaus, G. Dresselhaus, Ph. Avouris, "Carbon Nanotubes: Synthesis, Structure, Properties, and Applications", *Topics in Applied Physics*, Springer, New York, 2001.
10. R. Saito, M.S. Dresselhaus, G. Dresselhaus, "Physical Properties of Carbon Nanotubes", Imperial College Press, London, 1998.
11. M. L. Cohen, *Materials Science and Engineering C*, 2001, 15, 1.
12. X. Sun, Y. Li, *Angewandte Chemie International Edition*, 2004, 43, 597.
13. H. Qian, F. Han, B. Zhang, Y. Guo, J. Yue, B. Peng, *Carbon*, 2004, 42, 761.
14. Y. Fan, G. Liu, X. Liu, B. Xu, *Journal of Material Science*, 2006, 41, 5242.
15. Y.Z. Jin, C. Gao, W.K. Hsu, Y. Zhu, A. Huczko, M. Bystrzejewski, M. Roe, C.Y. Lee, S. Acquah, H. Kroto, D.R.M. Walton, *Carbon*, 2005, 43, 1944.
16. A. Levesque, V.T. Binh, V. Semet, D. Guillot, R.Y. Fillit, M.D. Brookes, T.P. Nguyen, *Thin Solid Films*, 2004, 464-465, 308.
17. S. Houston, G.J. Brown, T. Murray, S. Fairchild, K. Eyink, A. Smetana, *Journal of Electronic Materials*, 2009, 38, 737.
18. Z.L. Wang, Z.C. Kang, *The Journal of Physical Chemistry*, 1996, 100, 17725.
19. M. Terrones, G. Terrones, H. Terrones, *Structural Chemistry*, 2002, 13, 373.
20. T.W. Ebbesen, *American Institute of Physics*. 1996, S-0031- 9228-960M20-6.
21. A.A. Deshmukh, S.D. Mhlanga, N.J. Coville, *Materials Science and Engineering R*, 2010, 70, 1.
22. J.Y. Miao, D.W. Hwang, K.V. Narasimhulu, P.I. Lin, Y.T. Chen, S.H. Lin, L.P. Hwang, *Carbon*, 2004, 42, 813.

23. B.R. Selvi, D. Jagadeesan, B.S. Suma, G. Nagashankar, M. Arif, K. Balasubramanyam, M. Eswaramoorthy, T.K. Kundu, *Nano Letters*, 2008, 8, 3182.
24. D.B. Buchholz, S.P. Doherty, R.P.H. Chang, *Carbon*, 2003, 41, 1625.
25. A.R. Studart, H.C. Shum, D.A. Weitz, *J. Phys. Chem. B*, 2009, 113, 3914.
26. M. Wissler, *J. Power Sources*, 2006, 156, 142.
27. V.G. Pol, S.V. Pol, J.M. Calderon-Moreno, M.G. Sung, S. Asai, A. Gedanken, *Carbon*, 2006, 44, 1913.
28. V.G. Pol, S.V. Pol, A. Gedanken, M.G. Sung, S. Asai, *Carbon*, 2004, 42, 2738.
29. S.J. Ding, C.L. Zhang, M. Yang, X.Z. Qu, Y.F. Lu, Z.Z. Yang, *Polymer*, 2006, 47, 8360.
30. F. Wei, Q. Zhang, W.Z. Qian, H. Yu, Y. Wang, G. H. Luo, G. H. Xu, D. Z. Wang, *Powder Technol.* 2008, 183, 10.
31. A. C. Dupuis, *Prog. Mater. Sci.* 2005, 50, 929.
32. P. J. F. Harris, *Carbon Nanotubes and Related Structures: New Materials for the Twenty-First Century*, Cambridge University Press, Cambridge, UK, 1999.
33. R. Andrews, D. Jacques, D. Qian, T. Rantell, *Acc. Chem. Res.* 2002, 35, 1008.
34. D. S. Su, Chen, *Angew. Chem.* 2007, 119, 1855; *Angew. Chem. Int. Ed.* 2007, 46, 1823.
35. Istrian red soil (15 g) was placed in a rotating furnace (60 rpm) throughout the CVD process. The temperature was raised to 700°C at 10 °C min⁻¹ in He (100 mLmin⁻¹) and red soil was reduced by 75% H₂/ He (100 mLmin⁻¹) for 1 h. At reduction, a mixture of C₂H₄ (60 mLmin⁻¹) and H₂ (150 mLmin⁻¹) was introduced into the reactor for 1 h.
36. M. Endo, K. Takeuchi, Y. A. Kim, K. C. Park, T. Ichiki, T. Hayashi, T. Fukuyo, S. Iino, D. S. Su, M. Terrones, M. S. Dresselhaus, *Chem Sus Chem*, 2008, 1, 820.
37. A. Rinaldi, J. Zhang, N. Wang, R. Schlägl, D. S. Su, *Chem. Commun.* 2008, 6528.
38. S. Kawasaki, M. Shinoda, T. Shimada, F. Okino, H. Touhara, *Carbon*, 2006, 44, 2139.
39. S. Guggenheim, R. T. Martin, *Clay Clay Miner.* 1995, 43, 255.
40. M. Ogawa, A. Ishikawa, *J. Mater. Chem.* 1998, 8, 463.
41. S. C. Tjong, *Synthesis and Structure–Property Characteristics of Clay– Polymer Nanocomposites Nanocrystalline Materials*, Elsevier, UK, 2006, 311.

42. D. Gournis, M. A. Karakassides, T. Bakas, N. Boukos, D. Petridis, *Carbon*, 2002, 40, 2641.
43. A. Bakandritsos, A. Simopoulos, D. Petridis, *Chem. Mater.* 2005, 17, 3468.
44. Th. Tsoufisa, L. Jankovic, D. Gournis. , P. N. Trikalitis, Th. Bakas, *Mater. Sci. Eng. B*, 2008, 152, 44.
45. Q. Zhang, M. Zhao, Y. Liu, A. Cao, W. Qian, Y. Lu, F. Wei, *Adv. Mater.* 2009, 21, 2876.
46. S. Petit, D. Righl, J. Madejova, *Appl. Clay Sci.* 2006, 34, 22.
47. Q. Zhang, W. P. Zhou, W. Z. Qian, R. Xiang, J. Q. Huang, D. Z. Wang, F. Wei, *J. Phys. Chem. C*, 2007, 111, 14638.
48. Q. Zhang, M. Q. Zhao, J. Q. Huang, Y. Liu, Y. Wang, W. Z. Qian, F. Wei, *Carbon*, 2009, 47, 2600.
49. M. Darder, M. Colilla, E. Ruiz-Hitzky, *Chem. Mater.* 2003, 15, 3774.
50. M. Darder, P. Aranda, E. Ruiz-Hitzky, *Adv. Mater.* 2007, 19, 1309.
51. E. Ruiz-Hitzky, M. Darder, P. Aranda, *J. Mater. Chem.* 2005, 15, 3650.
52. E. Ruiz-Hitzky, *Adv. Mater.* 1993, 5, 334.
53. A. Gomez-Aviles, M. Darder, P. Aranda, E. Ruiz-Hitzky, *Angew. Chem.* 2007, 119, 941; *Angew. Chem. Int. Ed.* 2007, 46, 923.
54. M. Darder, M. Lopez-Blanco, P. Aranda, A. J. Aznar, J. Bravo, E. Ruiz- Hitzky, *Chem. Mater.* 2006, 18, 1602.
55. P. Aranda, M. Darder, R. Fernandez-Saavedra, M. Lpez-Blanco, E. Ruiz- Hitzky, *Thin Solid Films*, 2006, 495, 104.

CHAPTER: 2

Experimental technique for carbon nanostructures synthesis, structural/ microstructural characterization and vibrational spectroscopy of both natural and as-processed minerals

2.1 Introduction

This chapter focuses on the experimental techniques used for structural and spectroscopic characterizations of synthesized carbon nanostructures using natural materials. The synthesis on natural materials is done via chemical vapour deposition technique under various ambient atmospheres. This chapter also describes the techniques which have been used in carrying out the investigations described in chapter 3rd, 4th, 5th, 6th, 7th, and 8th for studying the natural and synthesized carbon nanostructures on natural minerals as well for other project activities optimization.

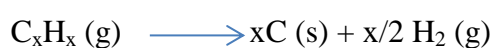
2.2. Chemical Vapour Deposition (CVD) technique

The CVD process is simple in concept and consists of a furnace, which can be heated in a controlled manner to the required temperature. A mixture of hydrocarbon (CH_4 , C_2H_2 , C_2H_4 or C_6H_6) and H_2 or inert gas (He, Ar) is passed over small transition metal particles (Ni, Co, Fe) or over a flat substrate with a thinly deposited layer of the transition metal onto the substrate (Si, Steel etc.) A catalytic chemical reaction occurs on the surface of the particle or flat substrate with the reaction rate being accelerated by the catalyst. A high definition image of the CVD system facility at Bar Ilan University is shown in figure 2.1.



Figure 2.1 CVD system facility at Bar Ilan University.

Cracking of the hydrocarbon occurs onto the surface giving carbon. The below diagram offers a summary of the process:



The carbon containing processor transfer other gases such as CO or CO₂



The growth characteristic of CNTs is dependent upon the process parameters entailing the pressure, catalyst, (type and size) of reactor, temperature, gas composition and flow rate. The stages involved in the CVD process are as follows:

- Transport of gas mixture to the surface where the catalyst is present (particle or flat substrate).
- Adsorption of the gases onto the surface.
- Chemical reaction (decomposition) on the surface and subsequent growth of CNT.
- Desorption of unwanted by products such as H₂ and unreacted species.
- Transport of products away from the surface and eventually out of the reactor.

A critical parameter in growing CNTs is the size and distribution of the catalytic nanoparticles. Control over the size is crucial and condensing in large clusters is highly undesirable. Condensation into large clusters is prevented by using support materials, such as FeO(OH), Fe₂O₃, Al₂O₃, SiO₂, MgAl₂O₄, MgO and occasionally graphite. Generally, a low concentration of catalyst is required to limit the coalescence of the metal particles.

As the catalyst is a critical component in the CVD process it is informative to look at the myriad of ways in which this can be produced. Several methods are documented including impregnation which involves:

- The salt solution (nitrate, chloride) containing the metal impregnates, the support material.
- Dry and calcination of the supported catalyst to obtain the metal oxide.
- Reduction in a H₂ atmosphere to make metal nanoparticles.

2.3 Structural/microstructural characterization

2.3.1 X-ray diffraction

X-ray single-crystal diffraction is a technique used to solve the complete structure of crystalline materials, ranging from simple inorganic solids to complex macromolecules. Thin film diffraction and grazing incidence x-ray diffraction may be used to characterize the crystallographic structure and preferred orientation of substrate-anchored thin films.

X-ray powder diffraction (XRD) is a rapid analytical technique used for phase identification of a crystalline material and can provide information on unit cell dimensions. It can be exploited to evaluate the crystallite size (grain size), and the preferred orientation in polycrystalline or powdered solid samples. Powder diffraction is commonly used to identify unknown substances, by comparing the experimental patterns with respect to a database maintained by the International Centre for Diffraction Data. It may also be used to characterize heterogeneous solid mixtures to determine relative abundance of crystalline compounds and, when coupled with lattice refinement techniques, such as Rietveld refinement, can provide structural information on unknown materials. Powder diffraction is also a common method for determining strains in crystalline materials. An effect of the

finite crystallite sizes is seen as a broadening of the peaks in an X-ray diffraction which is explained by the Scherer Equation. High-resolution XRD is used to characterize thickness, crystallographic structure, and strain in thin epitaxial films. It employs parallel-beam optics.

The x-ray diffraction pattern of a pure substance is like a fingerprint of the substance. The powder diffraction method is thus ideally suited for characterization of polycrystalline phases. The main use of powder diffraction is to identify components in a sample by a match procedure. Furthermore, the areas under the peak are related to the amount of each phase present in the sample. X-ray diffraction finds the geometry or shape of a molecule using x-rays. The direction and intensity of the scattered (diffracted) beams depends on the orientation of the crystal lattice with respect to the incident beam. These re-emitted wave fields interfere with each other either constructively or destructively, producing a diffraction pattern on a detector or film [1].

Any face of a crystal lattice consists of parallel rows of atoms separated by a unique distance (d-spacing), which are capable of diffracting x-rays. In order for a beam to be 100% diffracted, the distance it travels between rows of atoms at the angle of incidence must be equal to an integral multiple of the wavelength of the incident beam. The d-spacing's which are greater or lesser than the wavelength of the directed x-ray beam at the angle of incidence will produce a diffracted beam of less than 100% intensity. Hence, the interference is constructive when the phase shift is proportional to 2π .

2.3.1.1 Principles of XRD

Bragg gave a mathematical equation to establish a relationship between the wavelengths of the incident x-ray, the distance between the layers and the angle of diffraction.

$$n\lambda = 2d \sin\theta$$

Here, λ = wavelength of x-ray used

θ = Angle between incident X-rays and plane of the crystal. The diffracted beam makes an angle 2θ .

d = distance between planes of the constituent particles in a crystal.

n = an integer (1, 2, 3, 4 ...etc) which labels the serial order of diffracted spots.

Bragg's equation can be used to calculate the distances between repeating planes of the particles in a crystal. Conversely, if interplanar distances are given, the wavelengths of the incident beam of x-ray can be calculated. This condition can be expressed by Bragg's law as shown in figure 2.2.

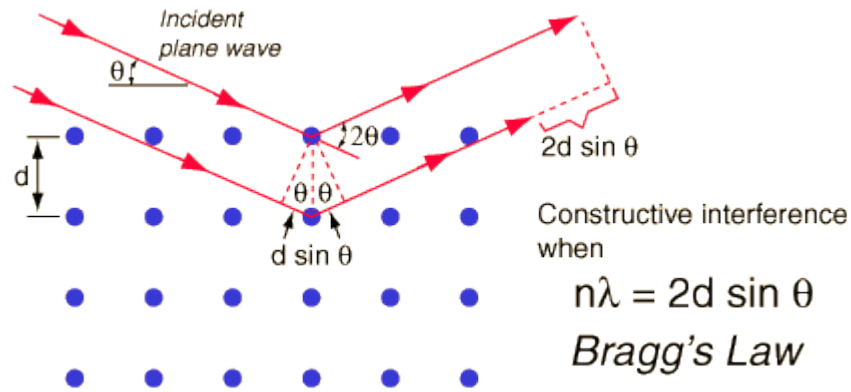


Figure 2.2 Bragg's Law: $n\lambda = 2d \sin \theta$

In case of small particles, with reduction in the size of the particles, the XRD lines get broadened, which indicates clearly that particle size has been reduced. Information of the particle size is obtained from the full width at half maximum (FWHMs) of the diffraction peaks. The FWHMs (β) can be expressed as a linear combination of the contributions from the wavelength (λ) and particle size (τ) through the Scherrer equation:

$$\beta = \frac{K\lambda}{\tau \cos \theta}$$

2.3.1.2 Working of XRD

A typical powder XRD instrument consist of four main components such as: x-ray source, specimen stage, receiving optics and x-ray detector. A schematic representation of a x-ray diffraction setup by a crystal is shown in figure 2.3. The source and detector with its associated optics lie on the circumference of focusing

circle and the sample is placed at the centre of the circle. The angle between the plane of the specimen and the direction of the incident x-ray beam is θ (Bragg's angle) and the angle between the incident x-ray beam and the detector is 2θ . For the XRD analysis, powder specimens can be mounted on the sample holder and the powder was assumed to consist of randomly oriented crystallites. When a x-ray beam is incident on the sample, x-rays are scattered by each atom in the sample. If the scattered beams are in phase, they interfere constructively and one gets the intensity maximum at a particular 2θ angle. The atomic planes from where the x-rays are scattered are referred to as 'reflecting planes'. A schematic representation of x-ray diffraction is sketched in figure 2.4.

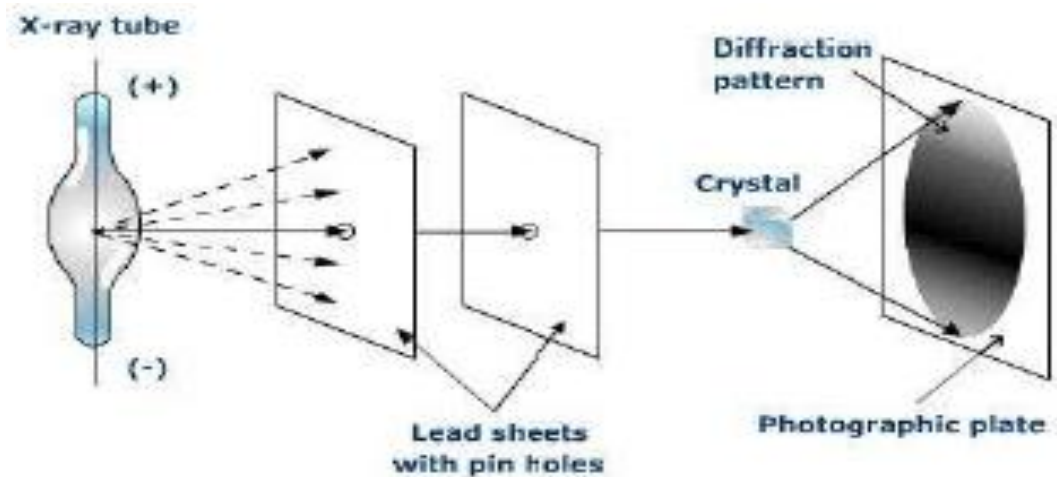


Figure 2.3 Schematic of the X-ray diffraction by a crystal.

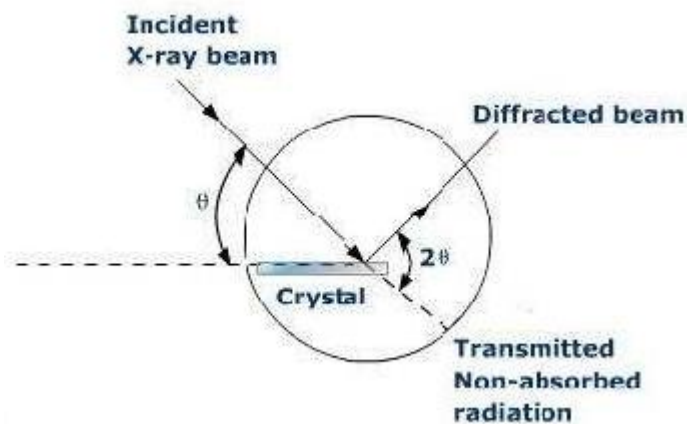


Figure 2.4 A schematic representation of X-ray diffraction

X-ray diffraction is especially valuable to the study of epitaxial layers and other thin film materials. Using precision lattice parameter measurement methods, the lattice mismatch of an epitaxial layer and its substrate can be determined with great precision. This lattice parameter match or mismatch is an important parameter for the epitaxial devices. Another interesting use of XRD for materials is that the coefficient of thermal expansion can be determined by plotting lattice parameters versus temperature using a high temperature diffractometer as shown below in figure 2.5.

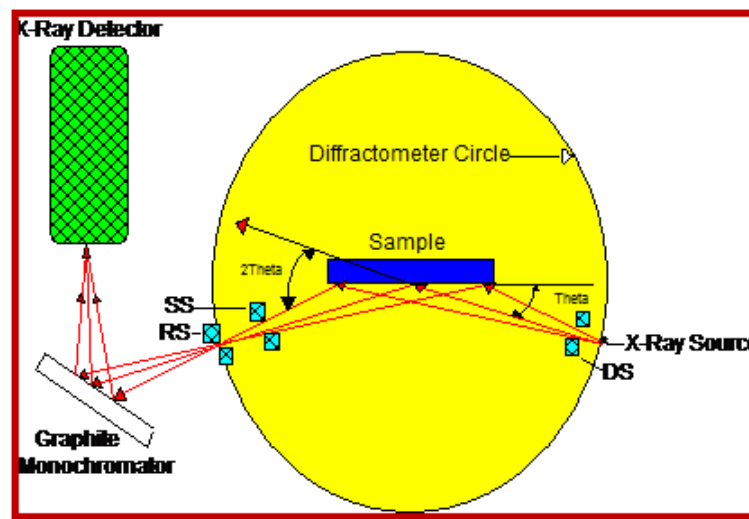


Figure 2.5 X-ray diffractometer process. DS=Divergence Slit, SS=Scatter Slit, RS=Receiving Slit, RSM= Receiving Slit Monochromator.

2.3.2 Environmental Scanning Electron Microscope (ESEM)

An electron microscope is a type of microscope that uses electrons to illuminate and create an image of a specimen. It has much higher magnification and resolving power than a light microscope, allowing it to see smaller objects and greater detail in these objects. In light microscopes, the maximum resolution that one can image is determined by the wavelength of the photons that are being used to probe the sample. Visible light has wavelengths of 400–700 nanometres; larger than many objects of interest. Ultraviolet rays can also not be used because it suffers from absorption predicament. Even shorter wavelengths, such as x-rays, exhibit a lack of interaction: both in focusing (nothing interact strongly enough to act as a lens) and actually interacting with the sample. On the other hand, the

wavelength of electrons, which is dependent on their energy, can be tuned by adjustment of accelerating fields, and can be much smaller than that of light. Yet, they can interact with the sample due to their electrical charge, this interaction can be exploited to obtain an image of the sample [2,3,4].

The scanning electron microscope (SEM) is a type of electron microscope capable of producing high-resolution images of a sample surface. SEM images, due to the manner in which they are created, have a characteristic three-dimensional appearance and are useful for judging the surface morphology of the sample.

2.3.2.1 Construction and working of SEM

Though the SEM and TEM both uses electrons to image a sample surface, the construction and working of an SEM are different from that of the TEM. Precisely, the working of SEM can be described as below:

A beam of electrons is generated in the electron gun, located at the top of the column; this beam is attracted through the anode, condensed by a condenser lens, and focused as a very fine point on the sample by the objective lens. The scan coils are energized (by varying the voltage produced by the scan generator) and create a magnetic field which deflects the beam back and forth in a controlled pattern. The varying voltage is also applied to the coils around the neck of the cathode-ray tube (CRT) which produces a pattern of light deflected back and forth on the surface of the CRT. The pattern of deflection of the electron beam is the same as the pattern of deflection of the spot of light on the CRT. The electron beam hits the sample, producing secondary electrons from the sample. These electrons are collected by a secondary detector or a backscatter detector, converted to a voltage, and amplified. The amplified voltage is applied to the grid of the CRT and causes the intensity of the spot of light to change. The image consists of thousands of spots of varying intensity on the face of a CRT that correspond to the topography of the sample.

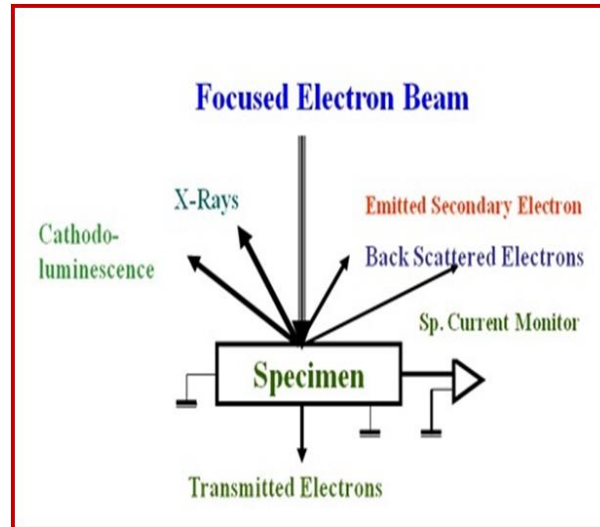


Figure 2.6 Six modes of SEM

2.3.2.2 Essential components of SEMs

Electron Source (“Gun”)

Electron Lenses

Sample Stage

Detectors for all signals of interest

Display / Data output devices

Infrastructure Requirements:

Power Supply

Vacuum System

Cooling system

Vibration-free floor

Room free of ambient magnetic and electric fields

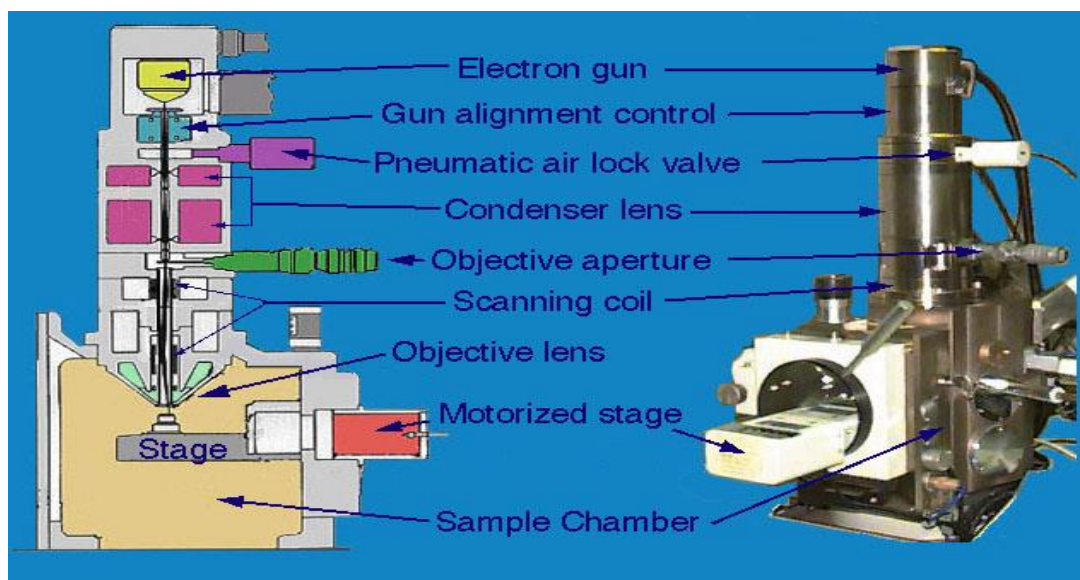


Figure 2.7 Components of SEM

SEMs always have at least one detector (usually a secondary electron detector), and most have additional detectors. The specific capabilities of a particular instrument are critically dependent on which detectors it accommodates. Figure 2.7 shows all the essential components of SEM.

2.3.2.3 Equipment Details

Model	: Quanta FEG 250
Resolution	: 1.2 nm
Signal	: SECONDARY ELECTRON
Detectors	SE, BSED, vCD, EDS, STEM
Magnification	: 4 X TO 100,000 X
Accelerating Voltage	: 200 V – 30 kV
Specimen Stage	: 5 – AXIS MOTORIZED
Specimen Chamber	: 310 mm × 220 mm
Vacuum System	: Turbo Molecular Pump
Stage Control	: Joystick and Mouse Control
Max Specimen Height	: 100 mm
X-ray Analysis	: 8.5mm AWD and 35° take off angle
Pressure Range	: 10–400 Pa



Figure 2.8 ESEM facility at Bar Ilan University, Israel.

2.4 Spectroscopic analysis

2.4.1 Fourier Transforms Infrared Spectroscopy (FT-IR)

An FT-IR Spectrometer is an instrument which acquires broadband NIR to FIR spectra. Unlike a dispersive instrument, i.e. grating monochromator or spectrograph, FTIR spectrometer collects all wavelengths simultaneously. This feature is called the Multiplex or Fellgett Advantage. An FT-IR (Fourier Transform InfraRed) is a method of obtaining infrared spectra by first collecting an interferogram of a sample signal using an interferometer, and then performing a Fourier Transform (FT) on the interferogram to obtain the spectrum. An FT-IR spectrometer collects and digitizes the interferogram, performs the FT analysis, and displays the spectrum.

2.4.1.1 Principle of FTIR spectroscopy

Infrared spectroscopy is non-destructive technique for materials analysis and used in the laboratory for over seventy years. Infrared absorption spectroscopy is the study of interaction of infrared radiation with matter as a function of photon frequency. Fourier Transform Infrared Spectroscopy (FTIR) provides specific information about the vibration and rotation of the chemical bonding and molecular structures, making it useful for analyzing organic materials and certain inorganic materials. An infrared spectrum represents a

fingerprint of a sample with absorption peaks which correspond to the vibrational frequencies of the atoms making up the material. Because each different material is a unique combination of atoms, no two compounds produce the exact same infrared spectrum. Therefore, infrared spectroscopy can result in a positive identification (qualitative analysis) of every different kind of material. In addition, the intensity of the peaks in the spectrum is a direct indication of the amount of material present. With modern software algorithms, infrared is an excellent tool for quantitative analysis.

The IR region is commonly divided into three smaller windows: near-IR (NIR: $400\text{--}10\text{ cm}^{-1}$), mid-IR (MIR: $4000\text{--}400\text{ cm}^{-1}$), and far-IR (FIR: $14000\text{--}4000\text{ cm}^{-1}$). Infrared photons of proper energy can be absorbed by a molecule which therefore undergoes vibrational transition. Like electronic transitions, these vibrational transitions correspond to distinct energies, and molecules absorb infrared radiation only at certain wavelengths and frequencies. Chemically bonded ions (i.e.: dipoles) vibrate at characteristic frequencies, and when exposed to infrared radiation, they absorb the radiation at frequencies that match their vibration modes. Measuring the radiation absorption as a function of frequency produces a spectrum that can be used to identify functional groups and compounds. Some impurities produce their own characteristic bands in the IR region. Spectral intensities of these bands are used to determine concentration of the impurities and their bonding with the host materials. In order to make identification, the measured interferogram signal cannot be interpreted directly. A means of “decoding” of the individual frequencies is required. This can be accomplished via a well-known mathematical procedure called the Fourier transformation. This transformation is performed by the computer which then presents the user with the desired spectral information for analysis.

2.4.1.2 Working of FTIR spectrometer

The basic instrument design is quite simple. Figure 2.9 (a) illustrates the schematic diagram and (b) a typical FTIR spectrometer.

The normal instrumental process is as follows:

1. *The Source*: Infrared energy is emitted from a glowing black-body source. This beam passes through an aperture which controls the amount of energy presented to the sample (and, ultimately, to the detector).
2. *The Interferometer*: The beam enters the interferometer where the “spectral encoding” takes place. The resulting interferogram signal then exits the interferometer.
3. *The Sample*: The beam enters the sample compartment where it is transmitted through or reflected off of the surface of the sample, depending on the type of analysis being accomplished. This is where specific frequencies of energy, which are uniquely characteristic of the sample, are absorbed.
4. *The Detector*: The transmitted/reflected beam finally passes to the detector for final measurement. The detectors used are specially designed to measure the special interferogram signal.
5. *The Computer*: The measured signal is digitized and sent to the computer where the Fourier transformation takes place. The final infrared spectrum is then presented to the user for interpretation and any further manipulation.

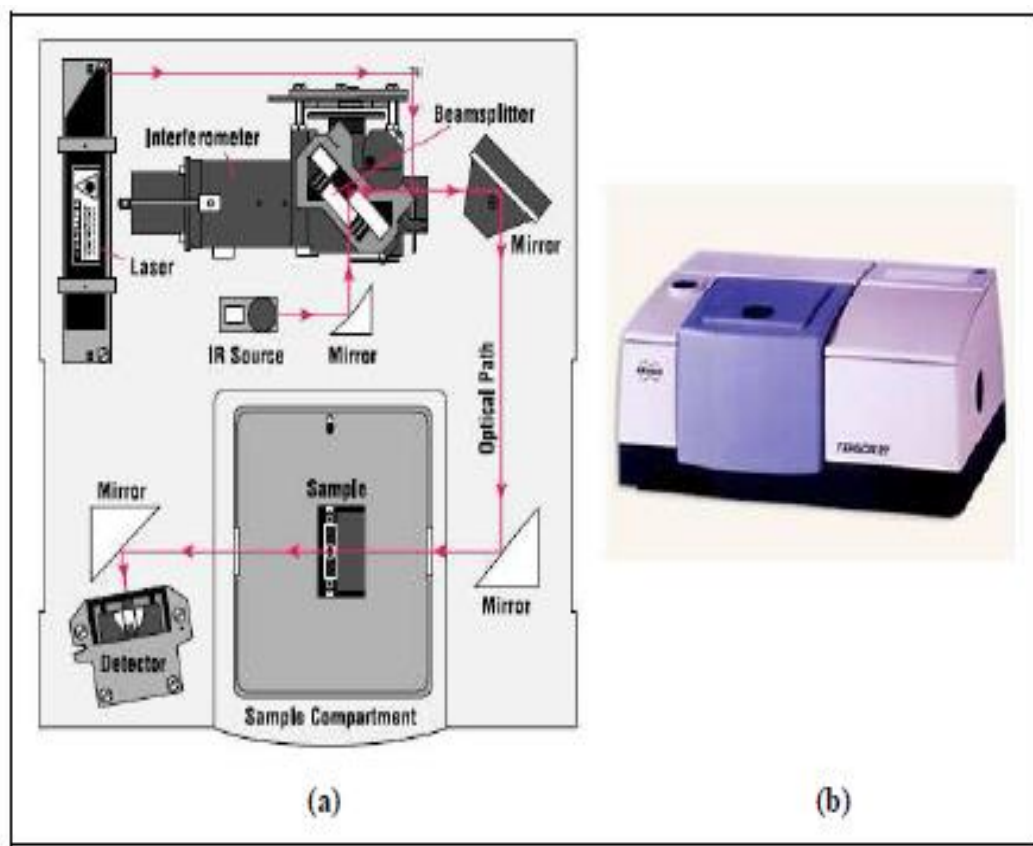


Figure 2.9 (a) Schematic diagram of FTIR and (b) FTIR instrument

Because there needs to be a relative scale for the absorption intensity, a background spectrum must also be measured. This is normally a measurement with no sample in the beam. This can be compared to the measurement with the sample in the beam to determine the “percent transmittance.” This technique results in a spectrum which has all of the instrumental characteristics removed. Thus, all spectral features which are present are strictly due to the sample. A single background measurement can be used for many sample measurements because this spectrum is characteristic of the instrument itself [5-9].

2.4.2 Micro- Raman spectroscopy

The Raman spectroscopy is the powerful and non-invasive technique named after Sir C.V. Raman, for the evaluation of vibrational, rotational and other low frequency modes in the materials [9,10]. It provides information complementary to FTIR. For a Raman active vibrational mode in a molecule, it must be associated with changes in the polarization as well sensitive to symmetrical molecules. This process is based on the inelastic scattering and can occur with a change in vibrational, rotational or electronic energy of a molecule. It is used for the vibrational analysis in single crystals due to their anisotropic nature.

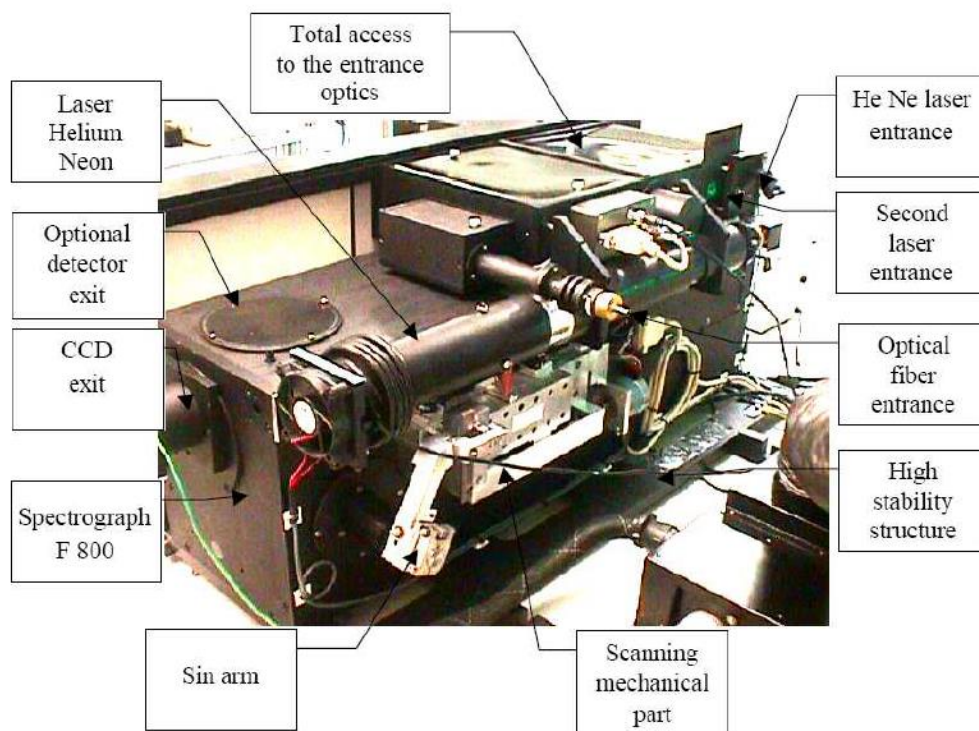


Figure 2.10 Main Components of the Jobin Yvon HR800 micro-Raman instrument facility at University of Verona, Italy.

2.4.2.1 Brief remarks about Raman scattering

When monochromatic light impinges on a molecular system interacts with it either elastically or inelastically. The inelastic part of the scattered radiation gives rise to a set of lines or bands shifted in energy, which, all together, provide the Raman (both Stokes and anti-Stokes) scattering of the system. The energy shift of each line is equal to the energy of a particular molecular vibration and is often called Raman shift. The electric field 'E' of the incident electromagnetic radiation distorts the electron cloud of molecule and induces dipole moment 'P' via relation

$$P = \alpha E,$$

where α is the electronic polarizability of the molecule.

But the molecular vibration changes the molecular polarizability (α) and thereby the energy of the scattered electromagnetic radiation gets changed. The Raman shift (ν) in cm^{-1} is given by the relation

$$\nu = 1/\lambda_{\text{incident}} - 1/\lambda_{\text{scattered}}$$

in which $\lambda_{\text{incident}}$ and $\lambda_{\text{scattered}}$ are the wavelengths of incident and Raman scattered photons in cm. The plot of intensity of scattered light vs. energy difference in cm^{-1} gives the Raman spectrum. The features (peak position, intensity, width etc.) of spectra of the materials are very sensitive to chemical composition, functional groups, structural phase, but also to defects and impurities. The selection rules are very sensitive to the local and global symmetries. In crystalline solids, the Raman Effect deals with phonons, instead of molecular vibrations. The fundamental requirement of a phonon to be Raman active is that the first derivative of the polarizability with respect to the vibrational normal coordinate should be a non-zero value. The Raman spectra of particular material consists the specific characteristics features and variation in these features depict the changes in the molecular/structural symmetry of materials [12,13].

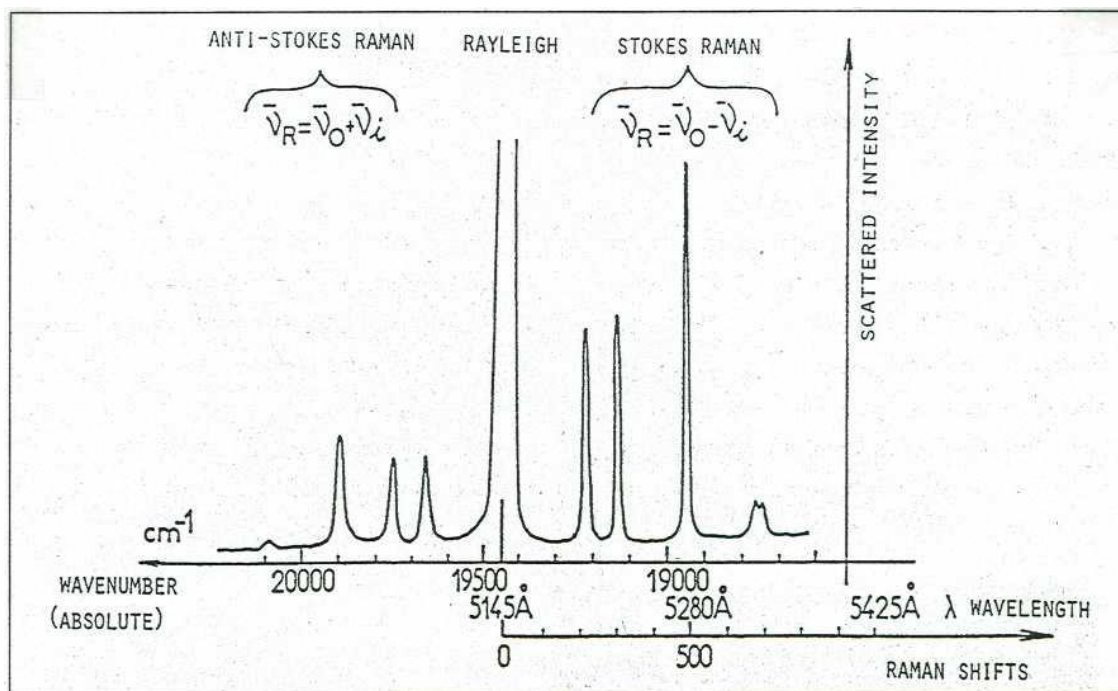


Figure 2.11 Example representations of the Rayleigh, Stokes and anti-Stokes components. Indicates also the correspondence between the wavelength and wavenumbers with specific reference to $\lambda = 5145 \text{ Å}$ corresponding to 19436 cm^{-1} .

As can be observed in Figure 2.11, the Raman lines have much smaller intensity of the Rayleigh line, and the lines Raman lower frequency ($\nu_0 - \nu_i$) (Stokes components), are more intense than the lines at higher frequency ($\nu_0 + \nu_i$) (anti-Stokes components). The elastic scattering and inelastic therefore depends on the chemical nature of the molecules responsible of the scattering. Normally the Rayleigh scattering has an intensity that is several orders of magnitude (6-9) higher than that of the Raman scattering. From figure 2.11 can be seen that the frequencies of Raman lines can be measured with reference to that of the excitation. Thus, the origin of the abscissa scale in figure 2.11 can just as well be placed at the position of the excitation frequency and the Raman frequencies will then appear at $\pm\nu_v$. In experimental spectroscopy, since a typical vibrational frequency has a value of the order of 12^{12} s^{-1} , the frequency values of Raman lines are usually divided by the velocity of light and are expressed in wavenumber (i.e; in cm^{-1}). When a photon with energy $E=h\nu$ passes through a molecular system, being not absorbed, it can interact with the molecule to the second order of the

perturbation theory. This process of interaction leads to the creation of a vibrational or rotational excitation, with transfer of energy from the incident photon to the molecule (Stokes process), and contextual scattering of a second photon with energy less than that incident. Alternatively the interaction with the incident photon can lead to the destruction of a quantum of vibrational or rotational energy and the concomitant diffusion of a second photon having energy greater than that of the incident photon (anti-Stokes process). It is evident that in a spectrum of scattered radiation will appear a very intense line with energy corresponding to the elastic scattering, and Raman peaks at energies where correspond to the frequencies of active excitations in the Raman processes. Raman shifts are therefore characteristic of the target species, as determined by the energy of excitation of vibrational or rotational transitions of the system. So, analysing the photons inelastically scattered by a molecule means testing its elementary excitations: the Raman spectrum reflects the rotational or vibrational spectrum of the target molecule. In the case of photon absorption, the situation becomes more intriguing due to concomitant emission of light (luminescence) that it is a first order process of radiation-matter interaction in the perturbation theory. The light emission is much more intense than the light scattering and therefore the luminescence signal can mask the Raman effect. On the other hand the resonance condition between the incident light and electronic transitions of the molecule (absorption) can produce an increase of the Raman scattering by several orders of magnitude [12-16].

2.4.2.2 Working of micro-Raman spectrometer LabRam HR800

In figure 2.12, the optical layout of the micro-Raman apparatus ***LabRam HR800*** is shown, from which it is possible to get some characteristics of the instrument. The He-Ne laser beam is polarized vertically (perpendicular to the plane of the picture of figure 2.12) and can be alternatively filtered by six neutral filters with optical density 0.3, 0.6, 1, 2, 3 and 4 which are placed before a first mirror and are driven by the software.

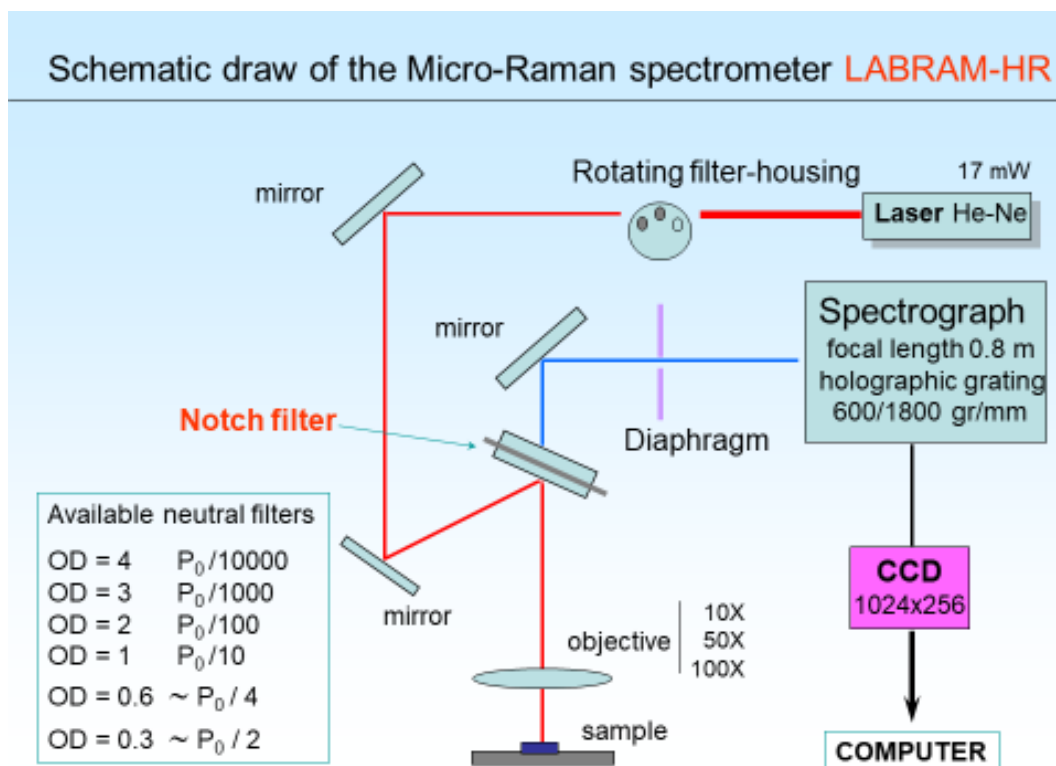


Figure 2.12: Optical layout of the Jobin Yvon HR800 micro-Raman instrument.

After that the laser beam is serially reflected by a system composed by a second mirror and by the notch filter (a narrow band reflecting filter). Finally, it is focussed on the sample surface by the microscope objective. The scattered radiation is collected by the same microscope objective in back scattering configuration and follows the same way back: the elastic part (Rayleigh component) of the scattered light is reflected again by the notch filter, while the inelastically scattered one (i.e.: Raman signal) passes through and is properly guided to entrance slit of the LaRabRam HR800 spectrograph.

The microscope is the high stability BX 40 model of Olympus with a focus graduation of about 1 μm , and is equipped with three objectives: 10X (numerical aperture, NA= 0.25), 50X (NA= 0.7), 80X (NA=0.75) and 100X (NA= 0.9). A colour camera is coupled to the microscope for the observation of the sample surface.

LabRam HR800 [16] spectrograph is of the asymmetric Czerny-Turner type, equipped with two grating of 1800 g/mm and 600 g/mm respectively, mounted on kinematic interchangeable holders. The scanning range of the

spectrograph is 950 nm with the 1800 g/mm grating, and 2850 nm with the 600 g/mm grating. The latter, less dispersing grating is about 3 times more luminous than the former. In figure 2.13 the resolution of the system is shown, for a slit width of 100 μm and using the 1800 g/mm grating.

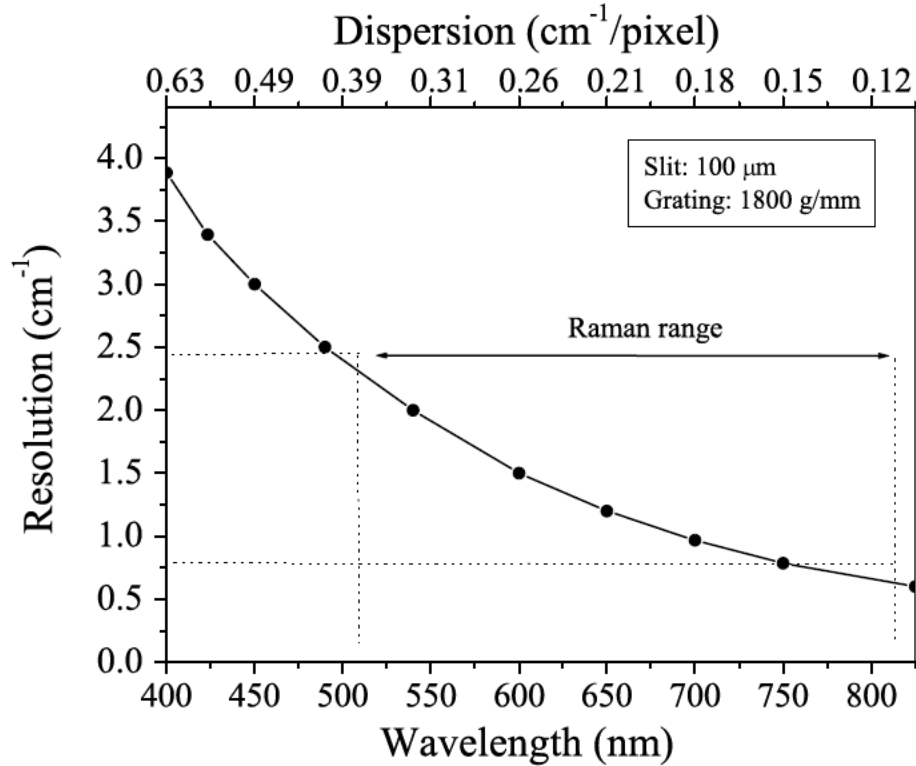


Figure 2.13: Resolution of the micro-Raman spectrograph for a slit width of 100 μm and the 1800 g/mm grating.

From the graph, we can note that, in this condition, the resolution of the spectrograph is always $< 2.5 \text{ cm}^{-1}$ and the dispersion of the grating changes by about a factor 6, between 400 and 800 nm. Moreover, in the range 450-850 nm, the wavenumber accuracy is $\pm 1 \text{ cm}^{-1}$ with the 1800 g/mm grating, and under normal condition of temperature stability ($\pm 1 \text{ }^{\circ}\text{C}$).

The calibration of the instrument is daily controlled by positioning the spectrograph to at 520.5 cm^{-1} and running a Raman spectrum acquisition of crystal silicon sample; if this line is outside the tolerance, the zero point parameter is corrected. In figure 2.14, the characteristics of the notch filter are reported; this graph has been obtained by positioning the spectrograph to 0 cm^{-1} and using the white lamp of the microscope (objective 10X and 1800 g/mm grating). The notch

filter is specific for the 632.8 nm laser exciting wavelength and we can note from figure 2.14 that its cut-off is often asymmetrical, to achieve a lower edge of transmission in the Stokes range. Moreover, it is clear that the lowest scattered energy that can be measured reliably is around 100-120 cm^{-1} [17-48].

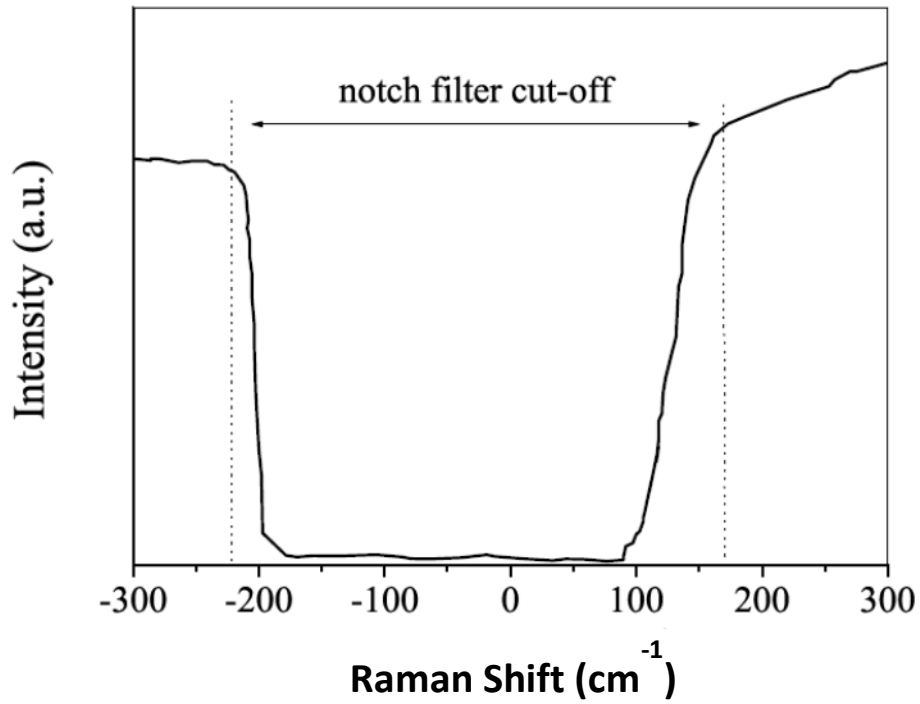


Figure 2.14: Response of the notch filter with the 10X objective and 1800 g/mm grating.

2.5 References

1. B.D. Cullity, Elements of X-ray Diffraction, Addison Wesley Publishing Co; London, 1967.
2. J.W. Heal, J.T. Sparrow, P.M. Cross, in use of the Scanning Electron Microscopy, Pergamon Press, Oxford, 1972.
3. W.R. Wenk, Electron microscopy in mineralogy, Springer Verlag, Berlin Heidelberg, Germany, 1976.
4. P.B. Hirsch, A. Howie, P.B. Nicholson, D.W. Pashley, M.J. Whelan, Electron Microscopy of thin crystals, Butterworths, London, 1957.
5. H. Gunzler, H.U. Gremlich, IR Spectroscopy: An Introduction, Wiley-VCH, Weinheim, Germany, 2002.
6. J.M. Hollas, Basic Atomic and Molecular Spectroscopy, Wiley, Chichester, UK, 2002.
7. D. Steele, 'Infrared Spectroscopy: Theory', in Handbook of Vibrational Spectroscopy, Vol. 1, Chalmers, J. M. and Griffiths, P. R. (Eds), Wiley, Chichester, UK, 2002, 44.
8. G.M. Barrow, Introduction to Molecular Spectroscopy, McGraw-Hill, New York, 1962.
9. J.M. Hollas, Modern Spectroscopy, 3rd Edn, Wiley, Chichester, UK, 1996.
10. A. Smekal, Naturwissenschaften, 1923, 43, 873.
11. C.V. Raman, K.S. Krishnan, Nature, 1928, 121, 501.
12. J.R. Ferraro, K. Nakamoto, Introductory Raman Spectroscopy, Academic Press, San Diego, 1994.
13. P. Hendra, C. Jones, G. Warnes, FT Raman Spectroscopy, Ellis Horwood Ltd, Chichester, 1991.
14. N.B. Colthrup, L.H. Daly, S.E. Wiberley, Introduction to Infrared and Raman Spectroscopy. 3rd Edition, Academic Press, San Diego, 1990.
15. D. Lin-Vien, N.B. Colthrup, W.G. Fateley, J.G. Grasselli, The Handbook of Infrared and Raman Characteristic Frequencies of Organic Molecules, John Wiley & Sons, New York, 1991.

16. <http://www.horiba.com/scientific/products/raman-spectroscopy/raman-spectrometers/raman-microscopes/hr-evolution/labram-hr-evolution-17309/>
17. P. Hendra, C. Jones, G. Warnes, FT Raman Spectroscopy, Ellis Horwood Ltd, Chichester, 1991.
18. B.T. Bowie, D.B. Chase and P. Griffiths, Appl. Spectrosc., 2000, 54, 200A.
19. M.V. Pellow-Jarman, P.J. Hendra, R.J. Lehnert, Vib. Spectrosc., 1996, 12, 257.
20. H. Wang, C.K. Mann, J.V. Vickers, Appl. Spectrosc., 2002, 56, 1538.
21. C.H. Chio, S.K. Sharma, P.G. Lucey, D.W. Muenow, Appl. Spectrosc., 2003, 57, 774.
22. B. Schrader, G.Z. Bergmann, Anal. Chem., 1967, 225, 230.
23. P.J. Hendra, IJVS, 1, edition 1, section 1 (www.ijvs.com).
24. G. Dent, Spectrochim. Acta A, 1995, 51, 1975.
25. Y.D. West, IJVS, 1, edition 1, section 1 (www.ijvs.com).
26. K.J. Asselin, B. Chase, Appl. Spectrosc., 1994, 48, 699.
27. G. Dent, F. Farrell, Spectrochim. Acta A, 1997, 53, 21.
28. C. Petty, Vib. Spectrosc., 1991, 2, 263.
29. N. Everall, J. Raman Spectrosc., 1994, 25, 813.
30. N. Everall, J. Lumsdon, Vib. Spectrosc., 1991, 2, 257.
31. J.S. Church, A.S. Davie, D.W. James, W.-H. Leong, D.J. Tucker, Appl. Spectrosc., 1994, 48, 813.
32. D. Loudon, in: Laboratory Methods in Vibrational Spectroscopy, H.A. Willis,
33. J.H. van der Mass, R.J. Miller (eds), John Wiley & Sons, Inc., New York, 1987.
34. M. Fleischmann, P.J. Hendra, A.J. McQuillan, Chem. Phys. Lett., 1974, 26, 163.
35. J.R. Lewis, P.R. Griffiths, Appl. Spectrosc., 1996, 50, 12A.

36. S.M. Angel, T.F. Cooney, H. Trey Skinner, in: *Modern Techniques in Raman Spectroscopy*, J.J. Laserna (ed.), Ch. 10, John Wiley & Sons, Inc., New York, 2000.
37. D.A. Smith, S. Webster, M. Ayad, S.D. Evans, D. Fogherty, D. Batchelder, *Ultramicroscopy*, 1995, 61, 247.
38. L. Song, S. Liu, V. Zhelyaskov, M.A. El-Sayed, *Appl. Spectrosc.*, 1998, 52, 1364.
39. S.D. Schwab, R.L. McCreery, *Appl. Spectrosc.*, 1987, 41, 126.
40. W. Xu, S. Xu, Z. Lu, L. Chen, B. Zhao, Y. Ozaki, *Appl. Spectrosc.*, 2004, 58, 414.
41. N.J. Everall, *Appl. Spectrosc.*, 2000, 54, 1515.
42. N.J. Everall, *Appl. Spectrosc.*, 2000, 54, 773.
43. B.R. Wood, S.J. Langford, B.M. Cooke, F.K. Glenister, J. Lim, D. McNaughton, *FEBS Lett.*, 2003, 554, 247.
44. R.L. McCreery, *Raman Spectroscopy for Chemical Analysis*, Ch. 10, John Wiley & Sons, Inc., New York, 2000.
45. D.A. Carter, W.R. Thompson, C.E. Taylor, J.E. Pemberton, *Appl. Spectrosc.*, 1995, 49, 11.
46. A.W. Fountain III, C.K. Mann, T.J. Vickers, *Appl. Spectrosc.*, 1995, 49, 1048.
47. K.G. Ray, R.L. McCreery, *Appl. Spectrosc.*, 1997, 51, 108.
48. B.T. Bowie, D.B. Chase, P. Griffiths, *Appl. Spectrosc.*, 2000, 54, 164.

CHAPTER: 3

Growth of carbon nanostructures using natural limonite laterite as catalyst via methane decomposition

3.1 Introduction

The first part of this chapter deals with the catalyst preparation and the synthesis of multi walled carbon nanotubes (MWCNTs) on natural low Ni containing lateritic iron ore powders via methane decomposition.

In the second part it reports on the results of morphology investigations, micro-structural properties characterization and vibrational spectroscopic behaviour of the synthesized MWCNTs.

3.2 Synthesis of MWCNTs by chemical vapour deposition

In this study, we have used two natural lateritic iron ores (known as limonite) with low Ni content containing (T Vol with 1.5 - 1.7 wt%-Ni). These samples were in form of powders having particle size less than 1 mm and come from New Caledonia mines. Further, Table 1 shows the elemental composition of the natural lateritic iron ores with low Ni content (T Vol with 1.5 - 1.7 wt%-Ni). All lateritic iron ores contain chemically bound water and so they can be dehydrated to produce porous materials. The elemental composition of the raw natural low Ni containing iron ores before was studied using EDS, and the EDX spectrum is shown in figure 3.1. The sample was found to contain Ni, Fe, Mg, Al, Si, Cr, Ti, Au O and C as the elements. The peak for Au and C arose from the C-tape used for the ESEM/EDX analysis and the Au coating done before performing the ESEM/EDX analysis, respectively.

Table 3.1 Average elemental compositions of the natural low Ni containing iron ores used in this study.

Sample/Elements(wt%)	Fe	Ni	Si	Mg	Al	O	Ti	Cr	C	Au
T Vol	37.02	1.46	5.27	1.93	2.29	38.81	0.41	0.63	6.0	6.19

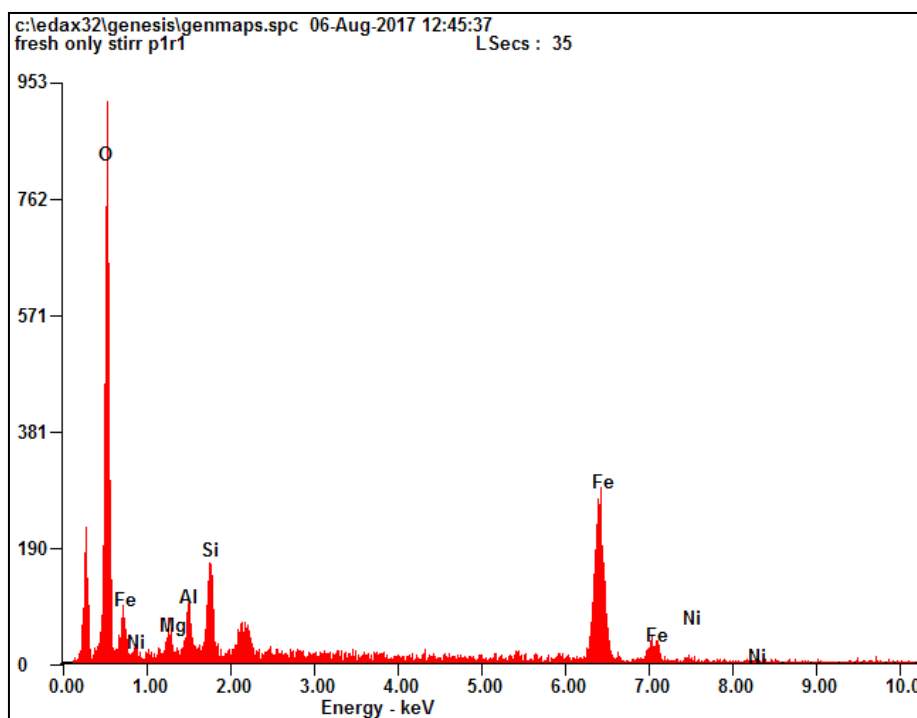


Figure 3.1 EDX spectrum of the natural low Ni containing iron ores laterite powder.

3.2.1 Catalyst preparation and methane decomposition

The as obtained Ni-containing iron ore powders, with < 1 mm size, were dehydrated at 600 °C for 4 h under Ar atmosphere in the chemical vapour deposition (CVD) furnace to obtain iron ore catalysts. The final calcined samples were decomposed with methane in the CVD system. A schematic diagram of the CVD equipment is shown in figure 3.2. The input gases flowed through a quartz tube and passed over a catalytic zone containing an iron ore catalyst. The temperature of the catalytic zone was kept at a programmed temperature by a controlled system using a thermocouple which was equipped with the CVD system. The CVD furnace was heated under Ar gas atmosphere. The calcined sample was weighed and loaded in the quartz boat and was purged with the Ar gas for 30 min. After that, the weighted sample in the quartz boat was moved in the middle of the furnace and the catalyst was reduced in situ with hydrogen (150 sccm) at 600 °C for 60 minutes. After reduction, the furnace was flushed with Ar gas to increase the reduction temperature to the reactor temperature for methane decomposition. In this study, we conducted the reaction at 700, 800 and 900 °C. Once attaining the reaction temperature, the Ar gas flow was closed and undiluted

methane (99.95%, NIG Gases, Malaysia) with a flow rate of 100 sccm was introduced into the furnace. The experiments were then performed for 1 hr on the stream. During the course of the reaction, the outlet gases were collected in bubbler. After the 4 hours of reaction, the quartz tube was shifted out of the furnace and was cooled to room temperature under a low flow of Ar (100 sccm) to collect the carbon deposited over the catalyst for its analysis. The flow of all types of gases was maintained using an electronic mass flow controller (MKS 247D). The summary of protocol for synthesis of MWCNTs is shown in figure 3.3.

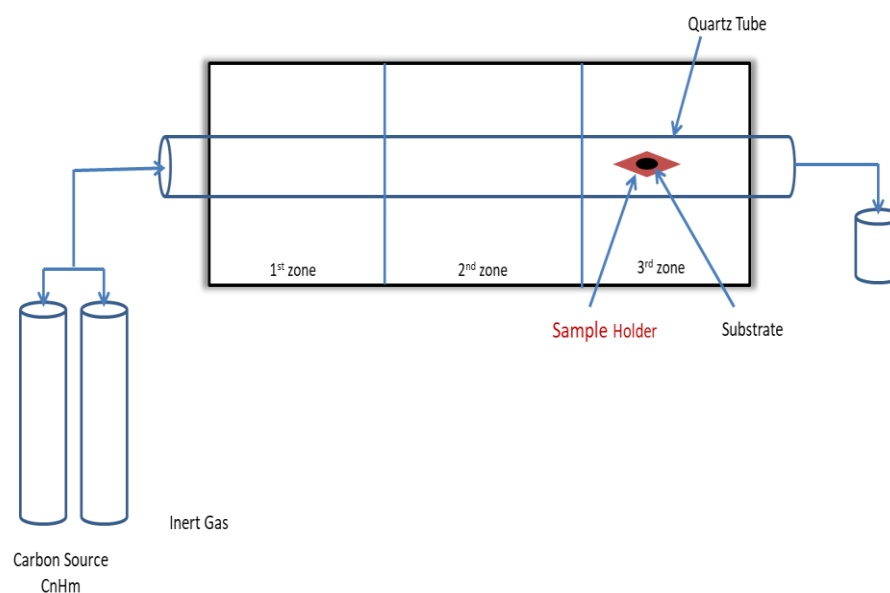


Figure 3.2 Schematic diagram of the CVD equipment.

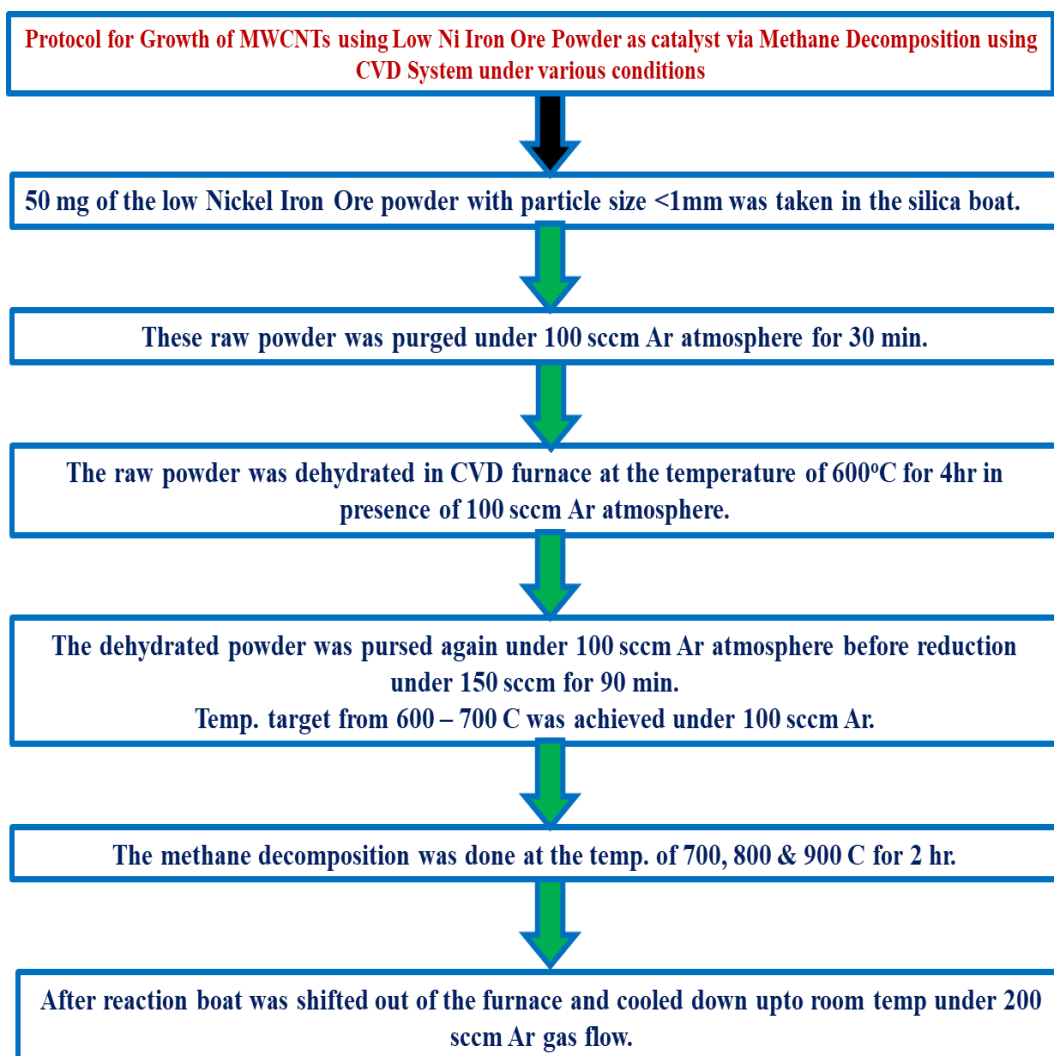


Figure 3.3 Schematic diagram for protocol of the synthesis MWCNTs.

3.3 Structural and spectroscopic characterization of calcined Ni-containing iron ore laterite powders and of synthesised MWCNTs

The raw catalyst and synthesized carbon nanostructures were characterized by using different techniques. The crystal structure and phase purity of the fresh and spent samples were determined by powder X-ray diffraction (XRD) using a Bruker D8 Advance diffractometer with a Cu K α radiation wavelength of 1.54 Å as the X-ray source. The samples were scanned from 20 to 80 degrees (2 θ) with a step size of 0.025 degrees. The mean crystalline size of the oxide phase of the calcined powders was calculated from the full widths at half maximum of the intense X-ray diffraction peaks using Scherrer's equation. The morphology of the

calcined catalyst and of the carbon nanostructures was observed using an environmental scanning electron microscope (ESEM) at an operating voltage of 3 kV equipped with an energy dispersive X-ray (EDX) analyser instrument to determine the elemental composition of the raw and of the as-obtained catalyst after calcination. Further, the vibrational properties of the raw natural low-Ni containing iron ore powders were investigated by means of micro-Raman and FTIR spectroscopies.

Systematic micro Raman measurements on the fresh catalyst after calcination and nano carbon deposited at different temperature were carried out by means of a single stage Horiba-Jobin Yvon spectrometer (model LABRAM HR800) mounting an He-Ne laser as excitation source (wavelength = 632.8 nm) and a notch filter in order to reject the Rayleigh line. Raman spectra were recorded in backscattering geometry over the Stokes-shifted region between 500 and 3000 cm^{-1} under irradiation power at the samples surface lower than 2 mW. The laser beam was focused onto the sample surface through an 80X objective, having a numerical aperture NA=0.75 and providing a surface spot of about 1.5 μm in size. The selection of the sample micro-region worth to be measured was achieved by means of a micro-manipulator operated under direct optical inspection on a colour camera interfaced to the microscope objective used to focus the laser beam onto the sample. The scattered radiation was dispersed by a 600 lines/mm diffraction grating and detected at the spectrograph output by a red-extended multichannel detector, a CCD with 1024X256 pixels, cooled by liquid nitrogen (N_2). The spectral resolution was about 1 cm^{-1} /pixel over the spectral range of interest. The spectral calibration was provided by the emission lines of an Ar lamp. Finally, in order to assess the reproducibility of the recorded spectra, repeated micro-Raman measurements were carried out under the same experimental conditions from different grains of the investigated powders.

FT-IR spectra were obtained at room temperature in the spectral range between 400 cm^{-1} and 4000 cm^{-1} using a JASCO spectrometer model FT/IR-660 plus as described in chapter 2. The IR spectra were recorded in the absorbance mode with a resolution of 4 cm^{-1} , using a KBr pallet as a reference. The number of scans for each spectrum was chosen to ensure an optimal signal-to-noise ratio.

3.4 Results and discussion

The natural raw Ni containing iron ore laterite sample and the as synthesized MWCNTs were characterized by several techniques to assess their phase purity, surface morphology, and microstructural properties. The spectroscopic characterization of natural raw Ni containing iron ore laterite sample and the as synthesized MWCNTs were investigated by micro Raman spectroscopy and FT-IR spectroscopic techniques.

3.4.1 Structural/Microstructural characterizations

The structural and microstructural characterizations along with surface morphology were carried out by X-ray Diffraction (XRD), Environmental Scanning Electron Microscopy (ESEM). The results obtained from above techniques are discussed below:

3.4.1.1 Gross structural characterization

X-ray Diffraction (XRD) technique was used to characterize gross structural analysis as well as phase purity of the natural raw Ni containing iron ore laterite powder as shown in figure 3.4. Before the XRD measurement, the diffractometer was calibrated with silicon powder ($d_{111}=3.1353 \text{ \AA}$). The results indicated that the iron ores mainly contained goethite, FeO(OH) , along with some amount of hematite, $\alpha\text{-Fe}_2\text{O}_3$, before dehydration and mainly hematite, $\alpha\text{-Fe}_2\text{O}_3$, after the dehydration. This means that the decomposition reaction of $2\text{FeO(OH)} \rightarrow \text{Fe}_2\text{O}_3 + \text{H}_2\text{O}$ occurred in low Ni contain iron ore at 600°C under Ar atmosphere with 300 sccm [1,2].

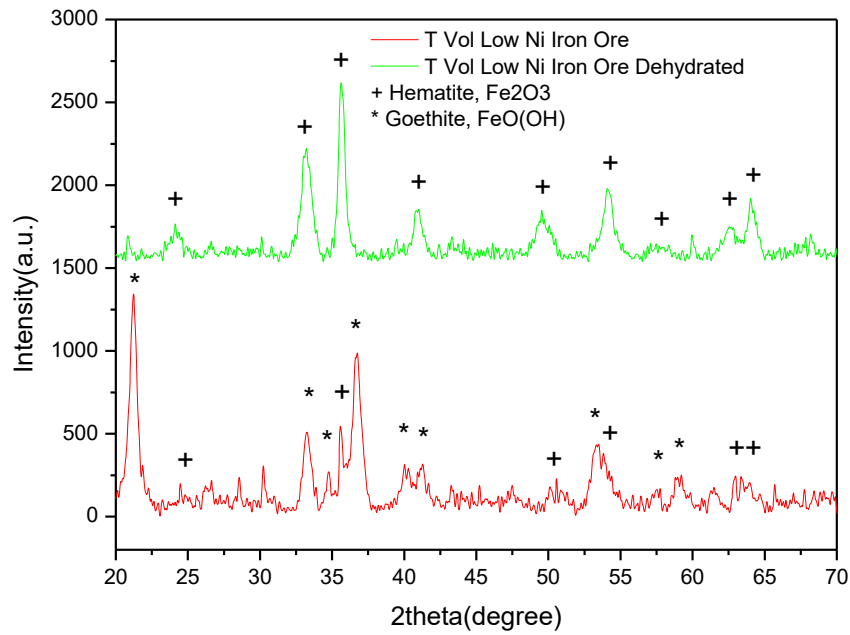


Figure 3.4 XRD patterns of the natural low Ni containing iron ores laterite powder before and after dehydration.

3.4.1.2 Surface morphology

The surface morphology has been carried out by environmental scanning electron microscopy (ESEM) technique. The ESEM images of natural raw Ni containing iron ore laterite with different magnifications before and after dehydration are reported in Figure 3.5. The samples after dehydration, carried out by calcination at 600 °C for 4 hrs under Ar atmosphere using chemical vapour deposition furnace, show clearly crystalline structures connected with each other. The average crystal size was bigger than ~0.5 μm .

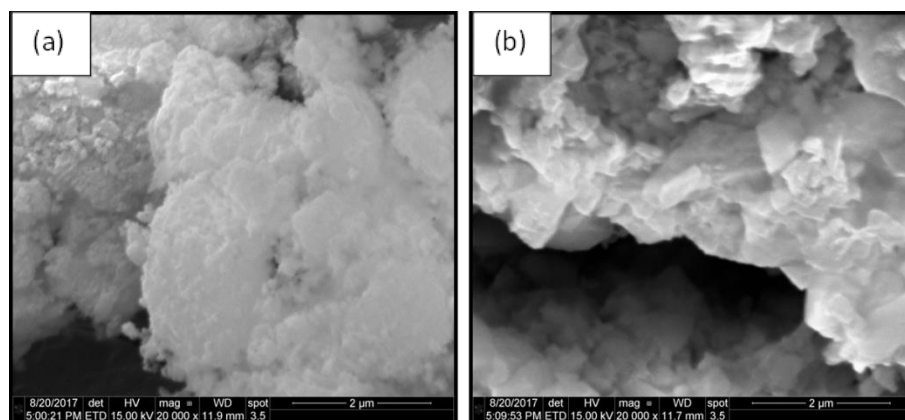


Figure 3.5 SEM images of (A); T Vol natural low Ni containing iron ores laterite powder ore before dehydration (DH), (B); T Vol ore after DH.

Figure 3.6 represents the, ESEM images with different magnifications of the nanostructured materials deposited at (a-b) 700 °C, (c-d) 800 °C and (e-f) 900 °C by methane decomposition for 1 hr with 100 sccm using chemical vapour deposition method. The images show clearly nanotubes like structures connected with each other in a bundle formation. The average diameter of the MWCNTs was found to increase by raising the deposition temperature from 700 to 900 °C. Although the diameter of the nanotubes varies from 10-100 nm and increases with increase in the temperature. That is, as the reaction temperature was increased in this range, the carbon nanomaterials yield significantly increased. This relationship may have been due to the enhanced catalytic activity of the catalyst at high reaction temperatures. The higher the reaction temperature, then the higher the catalytic activity and hence the carbon yield.

Metal-supported carbon particles with a multi walled carbon nanotubes - like morphology were deposited over the catalysts at 700 °C and 900 °C. A mixture of both types of carbons nanostructures was observed at 800 °C. The high catalytic stability of the catalysts at various reaction temperatures was due to the formation of Fe and Ni nanoparticles. The encapsulation of metallic species by carbon nanomaterials caused the lowering of their catalytic efficiency, which could be the reason for the different activity levels at the various reaction temperatures. Moreover, the effect of reaction temperature on the multi walled carbon nanotube's properties was studied: increasing the reaction temperature

from 700 °C to 900 °C resulted in increases of their diameter size and in the formation of graphitic nanostructures.

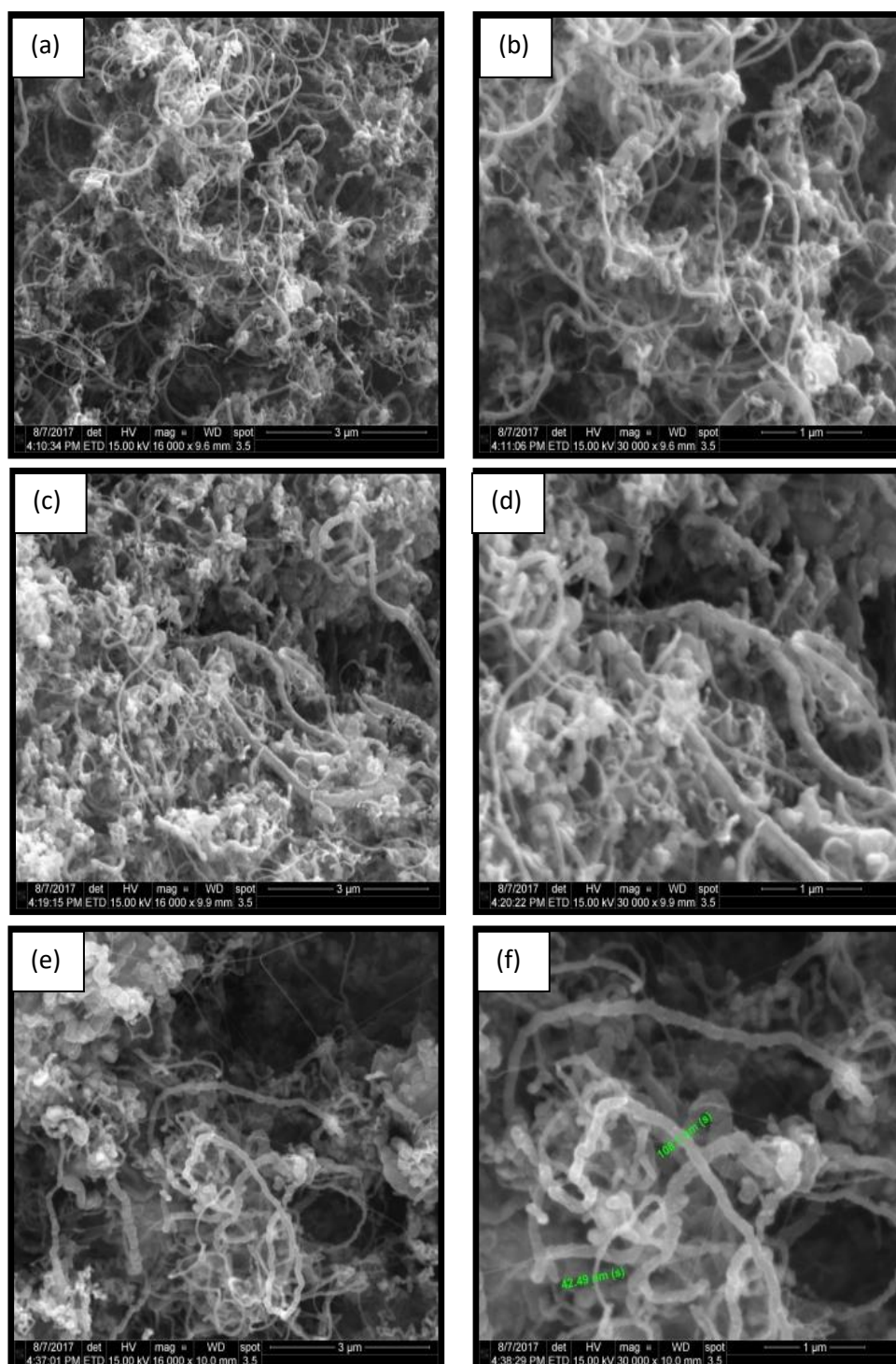


Figure 3.6 ESEM images of the synthesised MWCNTs at (a-b) 700 °C, (c-d) 800 °C and (e-f) 900 °C.

Furthermore, the presence of goethite and hematite in the natural low Ni containing iron ore laterite powders and the growth of high quality MWCNTs were confirmed by vibrational spectroscopy measurements.

3.4.2 Spectroscopic Analysis of raw natural low Ni containing iron ores before and after dehydration and of the synthesised MWCNTs

The spectroscopic characterization of natural raw Ni containing iron ore laterite sample and the as synthesized MWCNTs were investigated by micro Raman spectroscopy and FT-IR spectroscopic techniques.

3.4.2.1 Micro-Raman investigations on both raw Ni containing iron ore laterite sample and the as synthesized MWCNTs

The vibrational properties of the raw natural low Ni containing iron ores before and after dehydration was studied using micro Raman spectroscopy and their Raman spectra are shown in figure 3.7.

Figure 3.7, shows two experimental spectra obtained from the natural low Ni containing iron (T Vol with 1.5 - 1.7 wt% Ni) ores laterite catalysts. In general the as-observed spectra consisted of a well resolved Raman over imposed a broad, continuous luminescence background which was subtracted using the Horiba LabSpec 5 baseline correction. The as-obtained Raman spectra were then compared with reference spectra of the RRUFF database. The peaks of the as-obtained Raman spectrum are well matched with the RRUFF data base for goethite, FeO(OH) and hematite, α -Fe₂O₃. Goethite is the main mineral phase found in this natural limonite laterite. The spectrum of goethite is shows bands at about 147, 231, 301, 389, and 676 cm⁻¹. The strongest band at 301 cm⁻¹ and 389 cm⁻¹ agree with the previous reported literature. The strongest bands at about 301 cm⁻¹ and 389 cm⁻¹ are assigned to the symmetric bending vibration and the symmetric stretching vibration of Fe-OH, and Fe-O-Fe/-OH, respectively [3, 4]. The bands at about 231 and 676 cm⁻¹ are consigned to the Fe-O A_{1g} mode and Fe-O stretching, respectively [5].

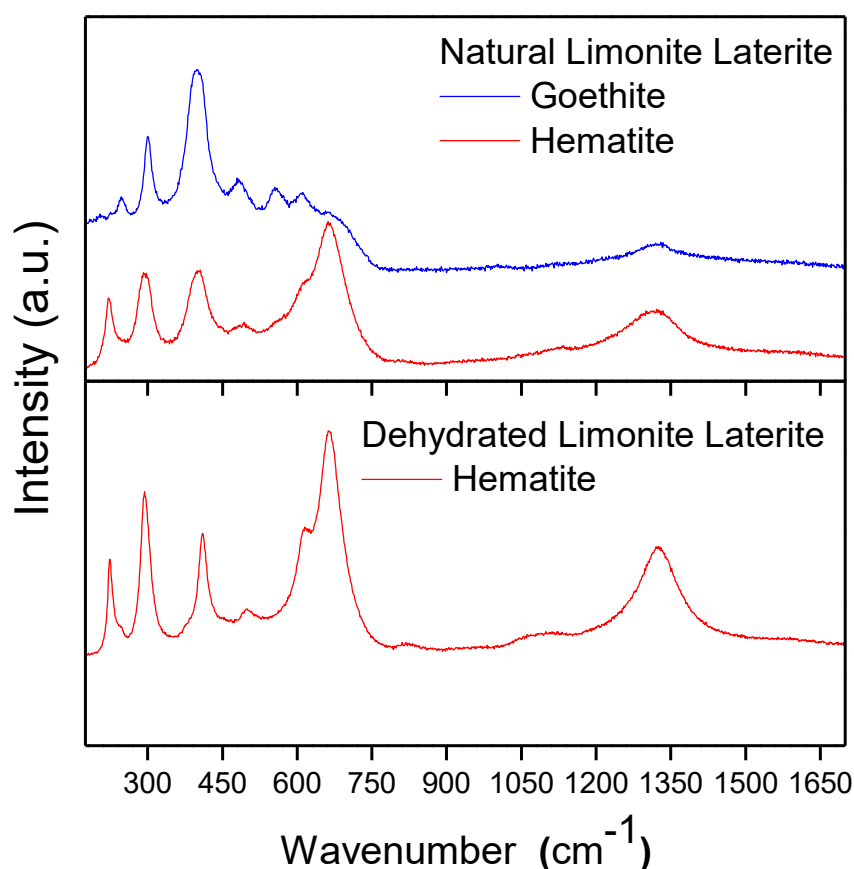


Figure 3.7 Typical Raman spectra recorded from different micro-regions of the natural low Ni containing iron (T Vol with 1.5 – 1.7 wt%-Ni) ore laterite powders: before dehydration (top panel), and after dehydration (bottom panel). In the upper panel the reference spectra, taken from RRUFF database, are also reported.

Further, micro inclusions of hematite mineral phases were also observed in natural limonite laterite. The most intense peaks of the Fe_2O_3 appear in the spectral range $175\text{--}1700\text{ cm}^{-1}$. Fig. 3.7 shows a spectrum acquired from hematite phase present in both natural and dehydrated limonite laterite which contains all the Raman bands corresponding to hematite (220, 243, 296, 405, 490, 607, 654 and 1320 cm^{-1}). Further to the seven Raman active vibrational modes, an additional broad band is observed at 1320 cm^{-1} . A broad medium band recorded near 1320 cm^{-1} , is assigned to a 2nd harmonic vibration. The origin of this band was first attributed to a two-magnon scattering process. Since hematite is an antiferromagnetic

material, upon irradiation with laser light, a collective spin movement can be excited which is termed a magnon. The additional intense broad band at 1320 cm^{-1} was therefore assigned to a two-magnon scattering process. Recently, this band has been re-interpreted as an overtone of a forbidden 660 cm^{-1} (odd symmetry IR-active phonon), probably activated by disorder. Currently, this re-interpretation is preferred by most Raman insiders. The spectrum of a perfect hematite crystal does not contain any signal near 660 cm^{-1} , while this forbidden band appears in many hematite spectra, recorded on different types of materials. The origin of this band has been the object of many works and according to recent literature it may be attributed to lack of long-range order as well as to an impurity phase. Hence very often called “disordered band” [3,6].

As for the synthesised carbon nanostructures, two well-resolved bands were observed in the Raman spectra of all of the samples obtained at each of the reaction temperatures. The first band was centered at about 1325 cm^{-1} (known as the D band) and the second band was centered at about 1572 cm^{-1} (known as the G band). The D band centred at 1325 cm^{-1} has been attributed to the presence of structural disorder of the graphitic carbon. However, in the present case, this band was attributed to the graphitic carbon defects. The G band centered at 1574 cm^{-1} was attributed to in-plane carbon-carbon stretching vibration of two adjacent graphitic layers. In addition to these two bands, a third band was also observed at 1605 cm^{-1} , as a shoulder of the G band. This band is known as the D_0 band and was assigned to graphitic defects on the carbon nanomaterials. In the low-wavenumbers region, at about 200 cm^{-1} there is presence of weak peaks which correspond to Radial Breathing Modes (RBM). Apart from these bands a strong and broad band at about 2645 cm^{-1} corresponding to the 2D peak. The peak positions of these Raman bands were found to be the same irrespective of the reaction temperature but the morphology of the synthesized carbon nanomaterials varied with variation in temperature. However, the relative intensity of one of the Raman bands was found to differ for different reaction temperatures. In fact, as the reaction temperature was increased from 700 to $900\text{ }^{\circ}\text{C}$ the intensity of the D band increases significantly whereas also, an appreciable change in the intensity of the G band was noticed upon increasing the reaction temperature. These results

indicated that the structural imperfections of graphitic carbon increases as the reaction temperature increased. The crystallinity and graphitization degree can be further explained on the basis of I_D/I_G and I_D/I_{2D} values of the carbon nanostructures deposited at various reaction temperatures, since it is an effective tool to assign the crystal-line quality and graphitization degree of the synthesized carbon nanostructures. The calculated I_D/I_G values were found to be 0.54, 0.66 and 0.83 at 700 °C, 800 °C and 900 °C, respectively, whereas the calculated values for I_D/I_{2D} were found to be 0.86, 0.87, 1.43 at 700 °C, 800 °C and 900 °C, respectively. These values of I_D/I_G and I_D/I_{2D} being corresponding with each other with increase of the temperature indicates a consistent crystalline quality and a progressive graphitization of the deposited carbon nanostructures with increase of temperature. However, the presence of RBM was only found in 700 °C and 800 °C with absence in the 900 °C, which further, proves our results regarding the formation of multi walled carbon nanotubes at 700 °C and 800 °C. Thus, a higher graphitization degree was observed for the carbon nanostructures deposited at 900 °C.

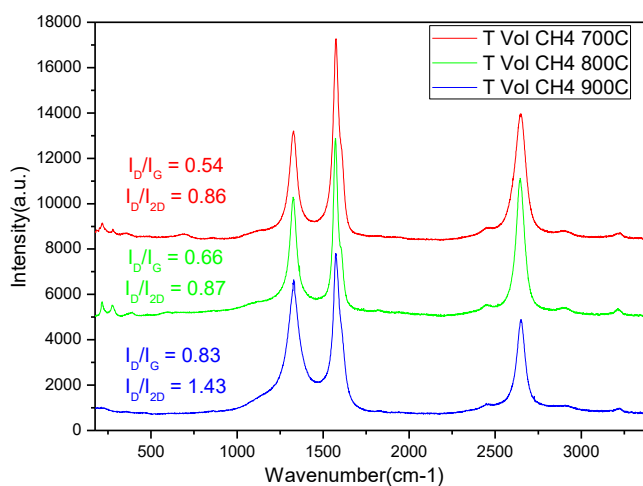


Figure 3.8 Raman spectrums of MWCNTs grown on dehydrated limonite laterite powder

Furthermore, we also employed the FTIR to ensure the quality of the natural low Ni containing iron ore laterite.

3.4.2.2 FT-IR (Fourier transform infrared spectroscopy) analysis of natural limonite laterite powder

The natural low Ni containing iron ore limonite laterite powder was used for FT-IR analysis. Figure 3.9 shows the absorbance spectrum of the natural low Ni containing iron ore laterite powder. Several distinct bands in the 500-4000 cm^{-1} region were observed. This FTIR spectrum exhibits the absorption frequencies of goethite: the peaks at 621 - 632 cm^{-1} are associated to the FeO_6 octahedral lattice vibrations, the peaks at 786 - 791 cm^{-1} , and at 886 - 897 cm^{-1} are assigned to Fe-O-H bending vibrations. There is a small peak around 1650 cm^{-1} that corresponds to bending modes of hydroxyl. The broad peaks centered at about 3190 cm^{-1} correspond to the stretching of goethite hydroxyls and surface H_2O molecules. The obtained result is consistent with earlier results obtained with the other characterization techniques.

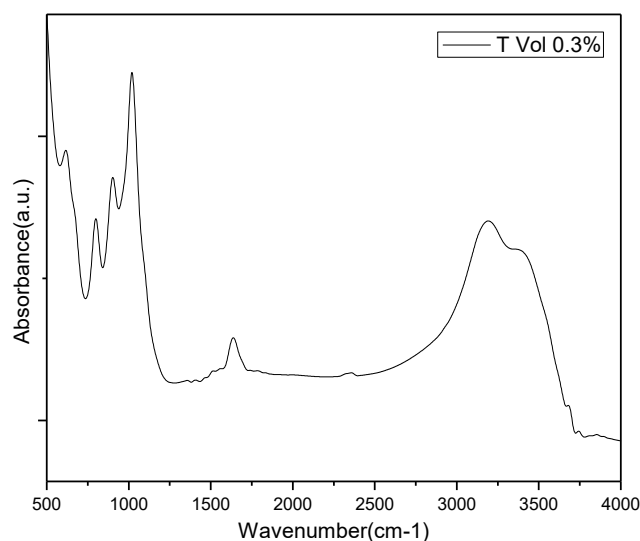


Figure 3.9 FTIR spectrum of natural low Ni containing iron ore limonite laterite powder.

3.5 Conclusions

The salient features of the present investigations are as follows:

We have successfully demonstrated the synthesis of MWCNTs using natural limonite laterite as a catalyst at 700, 800 and 900 °C which can be easily produced in large scale. Our method of synthesis is very simple, effective. The results of XRD micro Raman and FT-IR confirms the presence of goethite and hematite as major mineral phases inside the limonite laterite along with 1.7 % of Ni content as confirmed via EDX analysis. After the dehydration, the XRD and Raman confirm the transformation of goethite into hematite at 600 °C for 4 hrs under Ar atmosphere. The SEM results indicate that the average particle size of limonite laterite before and after dehydration to be about 5µm and most of particles appear in crystalline shape after dehydration. The main mechanism of FeOOH conversion to Fe₂O₃ was carried out successfully in the reducing atmosphere of Ar 100 sccm at 600 °C during 4 hrs. The ESEM images of the as obtained multi walled carbon nanotubes from using natural limonite laterite as a catalyst source and methane gas as carbon source exhibits that good quality of CNTs can be synthesised with diameter of about 10-100 nm. The formation of CNTs was confirmed further with the micro Raman spectroscopy with the characteristic radial breathing mode at about 200 cm⁻¹ and the occurrence of strong D, G and 2D bands. The values of I_D/I_G and I_D/I_{2D} being corresponds with each other with increase in the temperature indicates the consistent crystalline quality and the progressive graphitization of the deposited carbon nanostructures with increase in temperature. However, the presence of RBM was only found in 700 and 800 °C with absence in the 900 °C, which further, proves our results regarding the formation of multi walled carbon nanotubes at 700 and 800 °C. Finally, the highest graphitization degree was observed for the carbon nanostructures deposited at 900 °C.

3.6 References

1. K. Abe, G. Saito, T. Nomura, and T. Akiyama, *Energy & Fuels*, 2016, 30, 8457.
2. S. Gialanella, F. Girardi, G. Ischia, I. Lonardelli, M. Mattarelli, M. Montagna, *J. Therm. Anal. Calorim.*, 2010, 102, 867.
3. D. Faria, S. Silva, M. Oliveira, *J. Raman Spec.* 1997, 28, 873.
4. M. Hanesch, *Geophys. J. Int.* 2009, 177, 941.
5. M.A. Legodi, D. Waal, *Dyes Pigm.* 2007, 74, 161.
6. L. Wang, J. Zhu, Y. Yan, Y. Xie, C. Wang, *J. Raman Spec.* 2009, 40, 998.

CHAPTER: 4

Growth of carbon nanostructures using limonite laterite as catalyst via ethylene decomposition

4.1 Introduction

The first part of this chapter deals with the catalyst preparation and the synthesis of carbon nanostructures on natural lateritic ore powders, and comparative studies by varying the temperature and the ratio of flown gases on the catalyst which changes the formation of carbon nanostructures.

In the second part it reports on the results of morphology investigations, micro-structural properties and vibrational spectroscopy characterizations of the synthesized carbon nanostructures.

4.2 Synthesis of carbon nanostructures by chemical vapour deposition

In this study, we have used two natural lateritic iron ores (known as limonite) with low Ni content containing (T Vol with 1.5 - 1.7 wt%-Ni). These samples were in form of powders having particle size less than 1 mm and come from New Caledonia mines. They are the same samples described in chapter 3 of this thesis.

4.2.1 Catalyst preparation and ethylene decomposition

The as obtained Ni-containing iron ore powders, with < 1 mm size, were dehydrated at 600 °C for 4 h under Ar atmosphere in the chemical vapour deposition (CVD) furnace to obtain iron ore catalysts [1,2]. The final calcined samples were decomposed with ethylene in the CVD system. The input gases flowed through a quartz tube and passed over a catalytic zone containing an iron ore catalyst. The temperature of the catalytic zone was kept at a programmed temperature by a controlled system using a thermocouple which was equipped with the CVD system. The CVD furnace was heated under Ar gas atmosphere. In

the first set of the experiment, the final calcined catalyst sample was decomposed with ethylene in the CVD system. The calcined sample was weighed and loaded in the quartz boat and was purged with the Ar gas (99.9999%, from Gas Technologies) at 100 sccm for 30 min. After that, the weighted sample in the quartz boat was moved in the middle of the furnace and the catalyst was reduced in situ with Ar/H₂ gases (99.9999%, from Gas Technologies) with 100/400 sccm at 600 °C for 15 minutes. After reduction, the furnace was flushed with Ar gas to increase the reduction temperature to the reactor temperature for ethylene decomposition. In this study, we conducted the reaction at 700 °C, 800 °C and 900 °C. Once attaining the reaction temperature, the Ar gas flow was closed and undiluted ethylene (99.9999%, from Gas Technologies) with a flow rate of 100 sccm was introduced into the furnace and the experiment was then performed for 15 min on the stream.

In the second set of the experiment, we have used the calcined catalyst sample, and the calcined sample was weighed and loaded in the quartz boat and was purged with the Ar gas (99.9999%, from Gas Technologies) at 100 sccm for 30 min. after, that, the sample was reduced along with the flow of Ar/H₂ and C₂H₄ with flow rate of 100/400 sccm and 100 sccm for 15 min. And then, the Ar/H₂ flow was closed and the C₂H₄ was again flown for next 15 min.

In the third, set of the experiment, we have performed the experiments, on the natural raw samples without calcination. An argon flow of 100 standard cubic centimeters per minute (sccm) was maintained while gases were heated at 770 °C (the two first zones in the three-zone furnace and the first furnace in the two-furnace system) and the sample was heated at 750 °C (the third zone in the three-zone furnace and the second furnace in the two-furnace system). The raw sample was first purged for 30 min under the Ar gas atmosphere with 100 sccm flow. The raw sample were first reduced for 5 min with Ar/H₂ at the flow rate of 100/500 sccm. Next, for the reaction, we have flown C₂H₄, along with Ar/H₂ mixed with Ar/O₂ at the flow rate of 200, 100/500 and 100 sccm for 30 min. After the growth, C₂H₄ and Ar/O₂ flow was closed and for 1 min Ar/H₂ was kept flown. And the sample was cooled down under the flow of Ar. The same experiment was performed without the flow of Ar/O₂ along with C₂H₄ and Ar/H₂.

During the course of the reactions, the outlet gases were collected in bubbler. After the reaction, the quartz tube was shifted out of the furnace and was cooled to room temperature under a low flow of Ar (100 sccm) to collect the carbon deposited over the catalyst for its analysis. The flow of all types of gases was maintained using an electronic mass flow controller (MKS 247D). The summary of protocol for synthesis of carbon nanostructures is shown in figure 4.1.

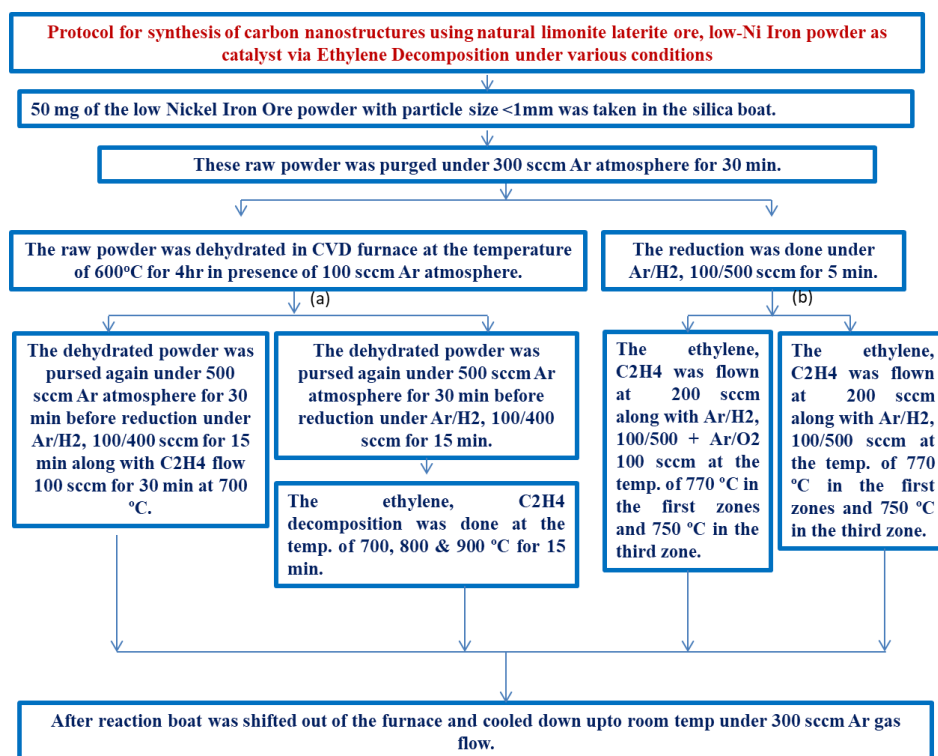


Figure 4.1 Protocol for the synthesis of carbon nanostructures under ethylene flux.

4.3 Structural and spectroscopic characterization of synthesised carbon nanostructures

The morphology of the calcined catalyst and of the synthesized carbon nanomaterials samples was observed using an environmental scanning electron microscope (ESEM) at an operating voltage of 3 kV equipped with an energy dispersive X-ray (EDX) analyser instrument to determine the elemental composition of the raw and of the as-obtained catalyst after calcination. Further,

the vibrational properties of the raw natural Ni containing iron ore powders were investigated by means of micro-Raman and FTIR spectroscopies.

Systematic micro Raman measurements on the fresh catalyst after calcination and synthesised nano carbon at different temperature were carried out by means of the Horiba-Jobin Yvon spectrometer (model LabRaman HR800) operated in the conditions already described in chapter 3.

4.4 Results and discussion

The structural and microstructural characterizations along with surface morphology were carried out by X-ray Diffraction (XRD), Environmental Scanning electron microscopy (ESEM) on the as synthesised carbon nanostructures. The spectroscopic characterizations of on the as synthesized carbon nanostructures were investigated by micro Raman spectroscopy techniques.

4.4.1 Structural/Microstructural characterizations

The as synthesized carbon nanostructures have been characterized by XRD and ESEM techniques. The results obtained from above techniques are discussed below.

4.4.1.1 Gross structural characterization

The crystal structure and phase purity of the raw natural and dehydrated limonite laterite was studied using X-ray diffraction (XRD), and the XRD patterns are shown in chapter 3 of this thesis. Before the XRD measurement, the diffractometer was calibrated with silicon powder ($d_{111}=3.1353 \text{ \AA}$). X-ray Diffraction (XRD) technique was used to characterize gross structural properties as well as phase purity of the CNTs and their transformation into carbon nano spheres on laterite powder as shown in figure 4.2. The diffraction peak centred at the 2Θ value at 25.96, 25.98 and 26.14 degrees for 700, 800 and 900 °C was indexed to the (002) plane and attributed to the formation of graphitic carbon on the surface of the catalyst with few structural imperfections [3]. The peak intensity measurement of the peak from the (002) plane has been reported to be an

effective way for the determination of the degree of graphitization of the deposited carbon nanomaterials [4]. Based on the measurements, for the three temperatures, i.e., 700, 800 and 900 °C, the highest degree of graphitization was observed for the nano carbon deposited over the metal particle at 900 °C, and the lowest for that at 700 °C. Furthermore, the interlayer d-spacing of the crystalline carbon was calculated to be 0.3429 nm, 0.3426 nm and 0.3405 nm at 700, 800 and 900 °C, respectively. These values were found to be quite close to the reported values for the distance between ideal graphitic layers, i.e., 0.3354 nm, which further indicated the excellent crystalline quality of the deposited nano carbon [5,6].

During the catalytic tests, α -Fe₂O₃ which was obtained from dehydration of FeO(OH) in the laterite ore was reduced to Fe₃O₄, FeO, Fe or FeNi alloy as we increase the temperature. The diffraction peaks observed for 900 °C at about 2 θ values of 43.68, 50.89 and 74.83 degrees were due to the presence of FeNi alloy (Fe_{0.68}Ni_{0.32}) with (111), (200) and (220), indexed peaks respectively (ICDD card No. 04-002-1863), which were formed by the reduction of Ni and Fe oxide over hydrocarbon decomposition with increase in temperature [6,7]. These Ni and Fe metal species were responsible for the stability of the catalyst and hence for the continuation of the reaction without any deactivation [6,8,9,10,11]. At 900 °C, in addition to the peaks of crystalline carbon, FeNi alloy phases, other weak peaks were also observed for Fe metal particles at the 2 θ values of 44.63, 64.96 degrees with indices (110) and (200), respectively (ICDD card No. 04-004-2475). These peaks were attributed to the formation of carbon spheres with the reaction of metallic species with carbon at 900 °C. The peaks at 43.68, 50.89, 74.83 degrees were not observed at low reaction temperatures, suggesting the lack of any chemical interaction between the carbon and alloys at low reaction temperatures.

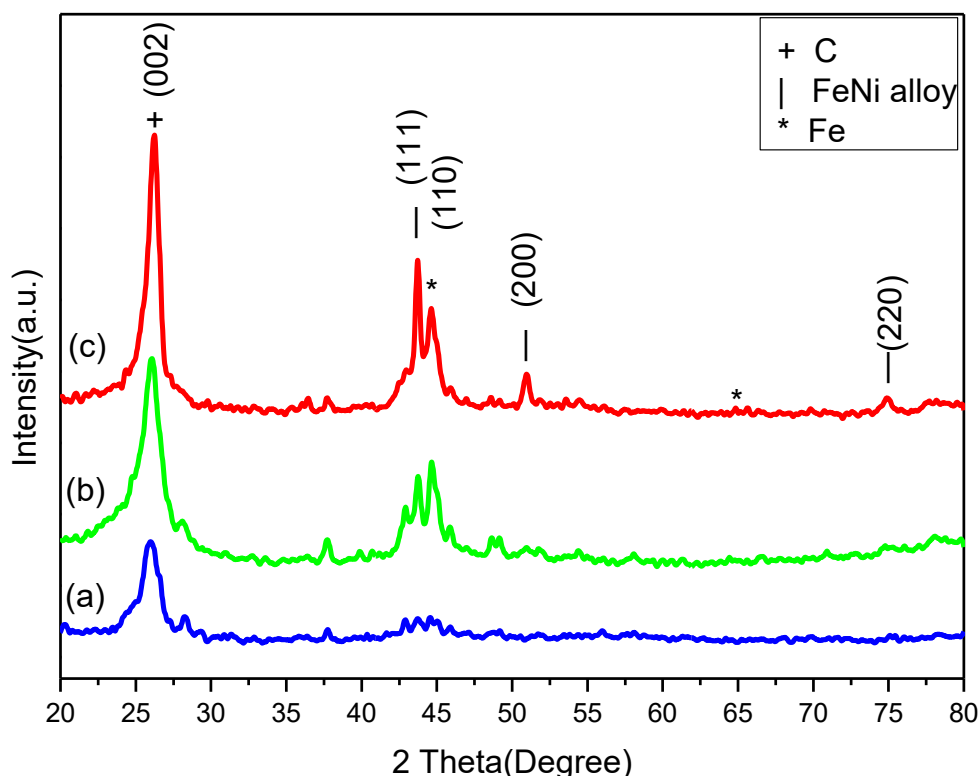


Figure 4.2 XRD patterns of the carbon nanostructures grown on dehydrated limonite laterite at (a) 700 °C, (b) 800 °C and (c) 900 °C.

4.4.1.2 Surface morphology

The surface morphology has been carried out by environmental scanning electron microscopy (ESEM) technique.

Fig. 4.3 represents the ESEM images with different magnifications of the carbon nanostructures over the dehydrated limonite laterite at (a-b) 700 °C, (c-d) 800 °C and (e-f) 900 °C deposited by C_2H_4 decomposition for 15 min with 100 sccm inside the CVD reactor. The images show clearly nanofibers/nanotubes like structures connected with each other in a bundle-like form, even if the diameter of the nanotubes varies from 10-100 nm and, therefore, the carbon yield increases with the increase of the temperature. This outcome is due to the enhanced catalytic activity of the catalyst at higher reaction temperatures. However, metal-supported carbon particles with a multi walled carbon nanotubes-like morphology

at 700 °C starts breaking up in carbon spheres over the range of temperature 800 and 900 °C. A mixture of both types of carbon nanostructures was observed at 800 °C. At 800 °C structural perturbations of CNTs start and at higher temperature turn out into the formation of spheroidal particles. Carbon spheres are formed when CNTs structure collapses into cluster of carbon layers. Figure 4.4, shows that the CNTs are about to break into spheroid particles at the 800 °C temperature. The high catalytic stability of the catalysts at various reaction temperatures is due to the formation of metallic particles. As, the sample was dehydrated and the FeO(OH) was reduced to Fe₂O₃ as shown in XRD data in figure 3.4 in chapter 3. Thus, before the catalytic tests, iron existed as Fe₂O₃ (limonite laterite after dehydration). During the catalytic tests, Fe₂O₃ has been reduced to Fe₃O₄, FeO, or Fe [1] as we increase the temperature, 700, 800 and 900 C. The Ni content in limonite laterite ore is very small. According Tang and Valix, Ni exists as (Fe, Ni)O(OH) in iron matrix of laterite ores, meaning Ni disperses at the atomic level [14]. Ni oxide in T Vol ore also get reduced at higher temperatures. This higher dispersion means a higher surface area of Ni. Nickel existed as oxide during the catalytic tests at 700 °C and changed its form to metal at 800 and 900 °C. And the differences in the catalytic performance and reduction ratio of iron oxides at certain temperatures were observed during the growth of MWCNTS and then transforming into carbon spheres. Initially, the hydrocarbon reaction rate increased with rising temperature and reduced oxides, in this case, Fe and Ni oxides reduced to Fe and Ni, respectively..

Further, the EDS results on the carbon spheres are also shown in figure 4.4 which gives about 98 At% of carbon. Moreover, the effect of reaction temperature on the carbon nanotube was also observed with the flakes deposited on the walled of the quartz as shown clearly in figure 4.5. A very high degree of graphitic carbon was deposited on the side walled of the quartz tube, which gives a very fine carbon spheres with average size of 500-700 nm in diameter, at 800 and 900 °C. So, increasing the reaction temperature from 700 to 900 °C resulted in increases in the crystallinity and in the graphitization degree of nano carbon.

Further, in figure 4.6, ESEM images of well resolved bundle of MWCNTs grown on dehydrated drilled core, which was flown with Ar/H₂, 100/400 sccm for 15 min along with C₂H₄ flow 100 sccm for 30 min at 700 °C. This gives a significant result in the better formation of MWCNTs with the flow of H₂ along with the C₂H₄.

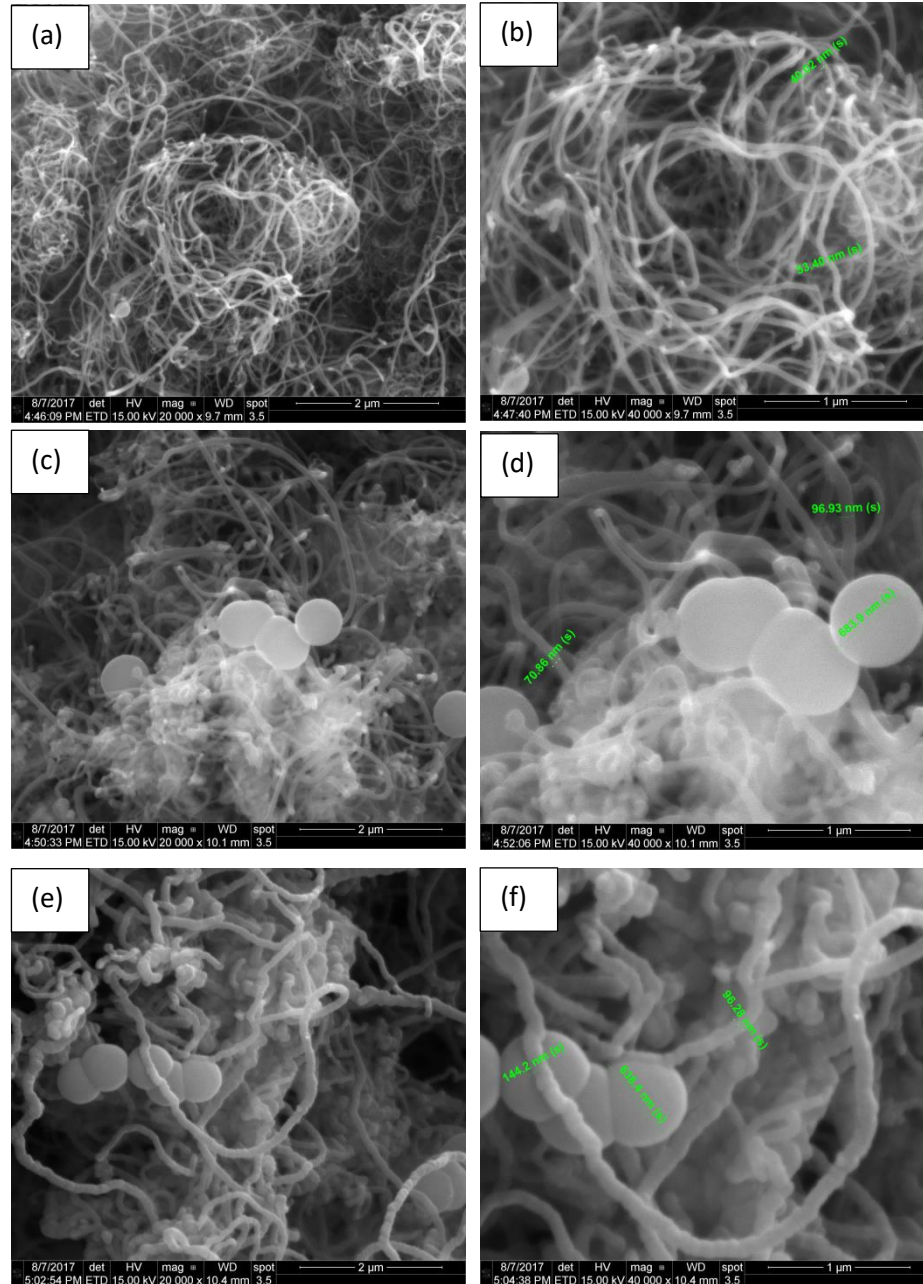


Figure 4.3 ESEM images of the carbon nanostructures at (a-b) 700 °C, (c-d) 800 °C and (e-f) 900 °C.

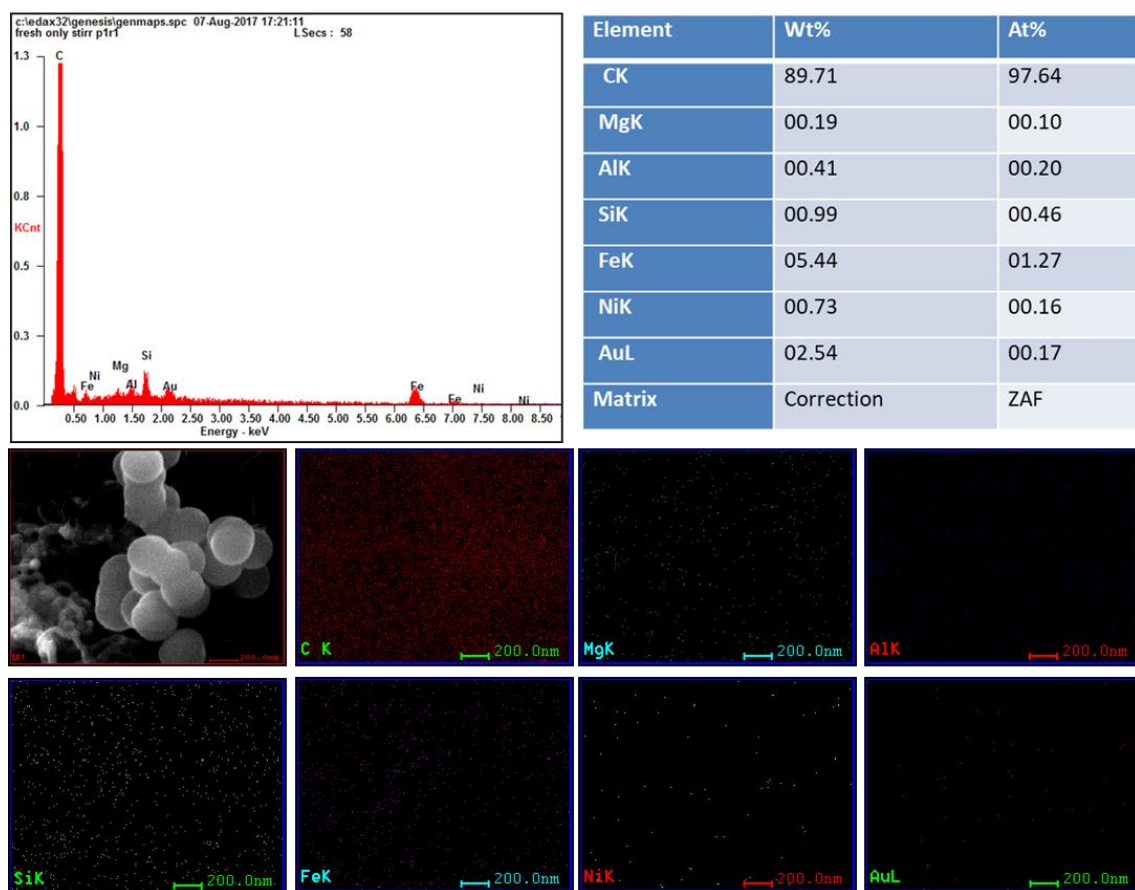


Figure 4.4 EDS analysis on the carbon spheres grown at 800 and 900 °C.

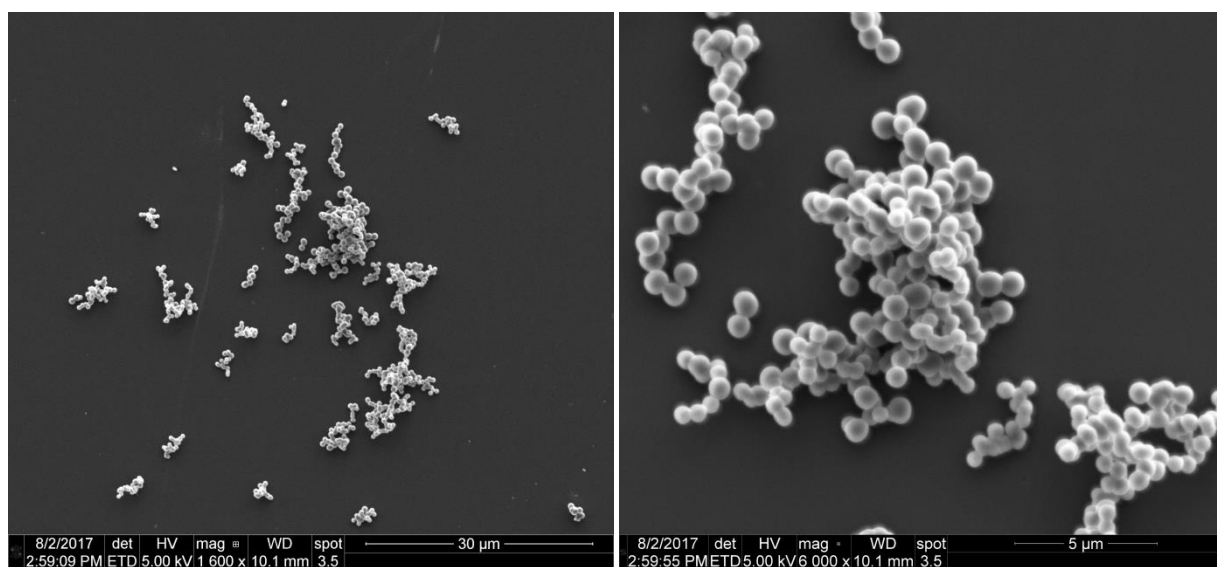


Figure 4.5 ESEM micrograph of carbon nanostructures on the flakes deposited on the quartz tube at 800 °C depicting carbon spheres bundles.

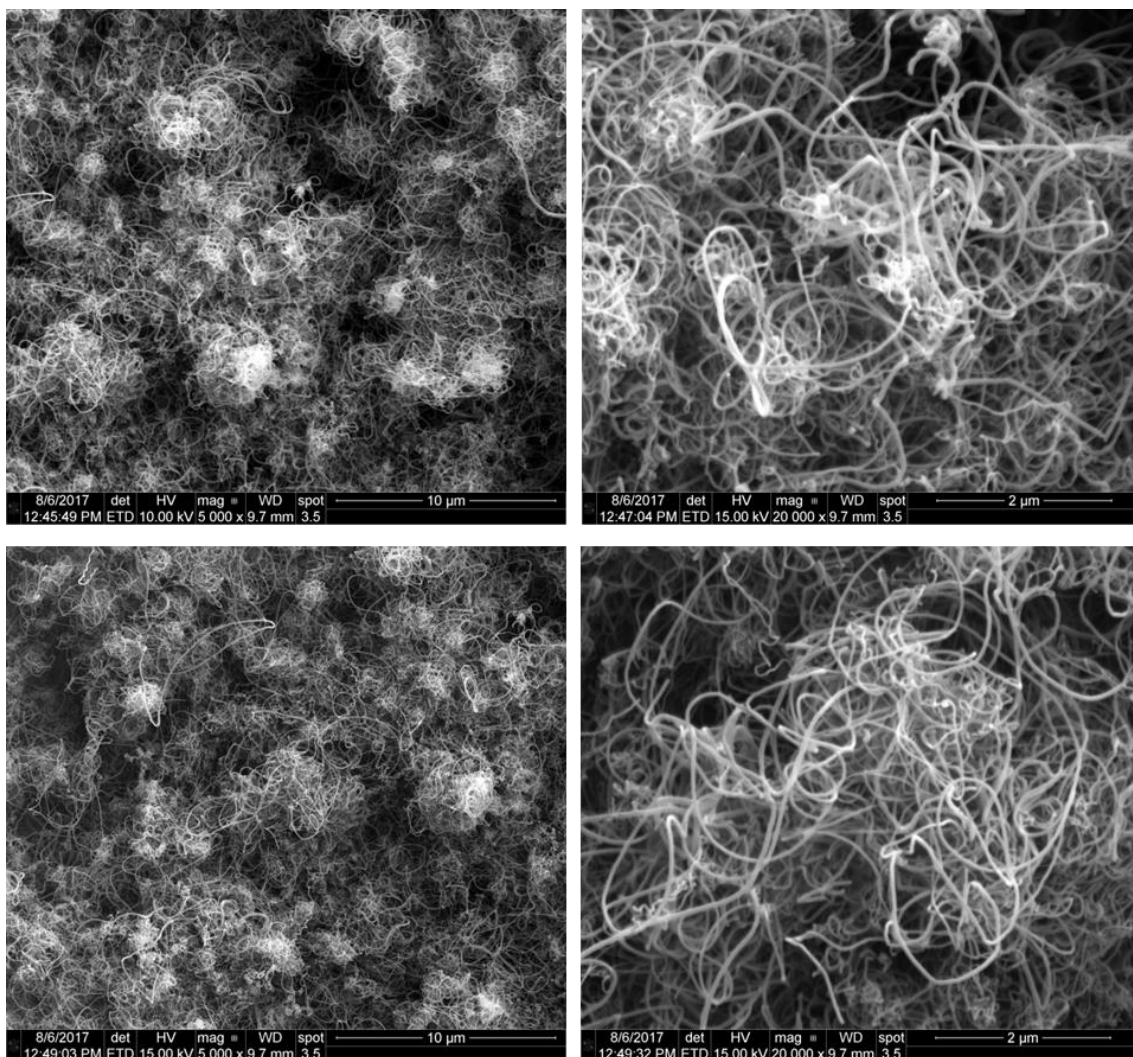


Figure 4.6 ESEM images of MWCNTs grown with Ar/H₂, 100/400 sccm for 15 min along with C₂H₄ flow 100 sccm for 30 min at 700 °C.

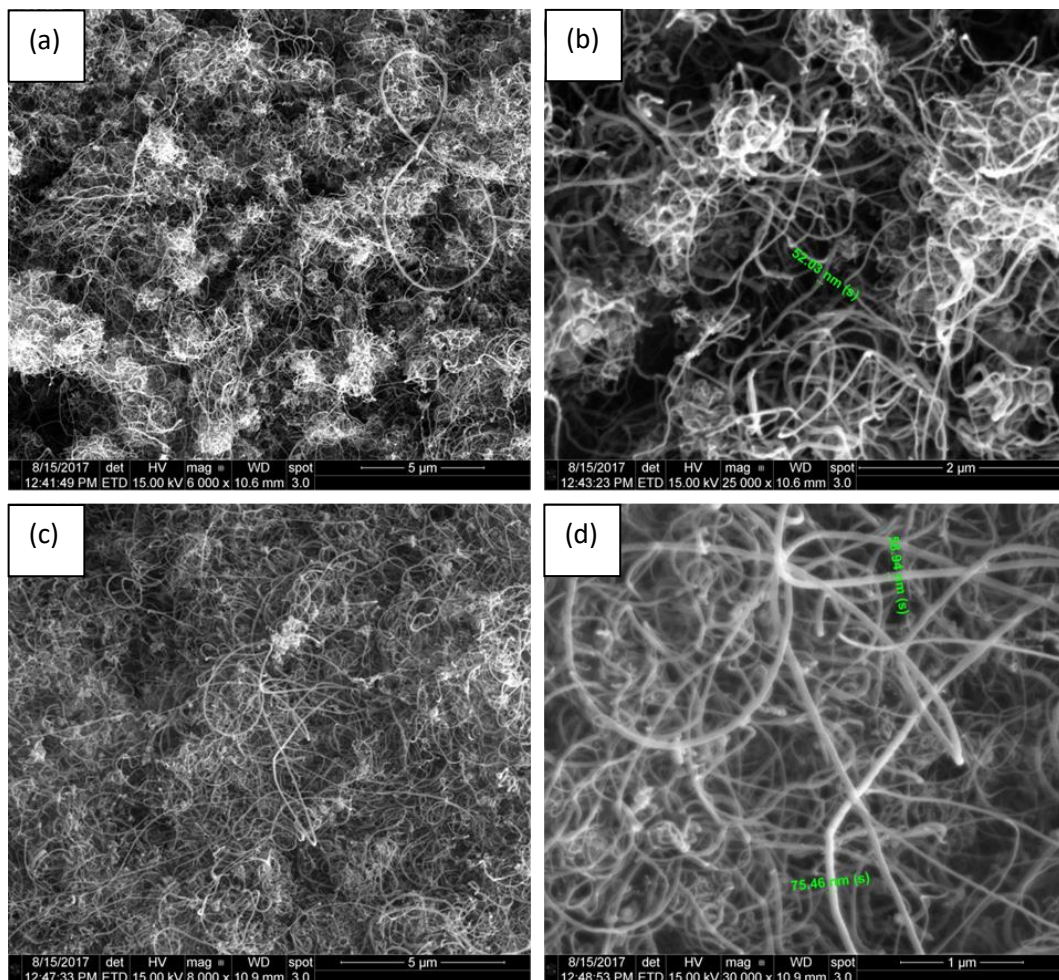


Figure 4.7 ESEM images of MWCNTs deposited via (a) The ethylene, $C_2H_4 + Ar/H_2 + Ar/O_2$ 100 sccm and (b) $C_2H_4 + Ar/H_2$ at the temp. of 770 °C in the first zones and 750 °C in the third zone.

In Fig. 4.7, ESEM images MWCNTs synthesized in the three-zone furnace with adding (a) and without adding (b) Ar/O_2 100 sccm of Ar/O_2 during growth along with $C_2H_4/Ar/H_2$ gases. The addition of this very small flow of Ar/O_2 (1% oxygen, so that the flow of oxygen flow is 10 sccm) led to the better and well resolved formation of MWCNTs.

Furthermore, the presence of growth of carbon nanostructures formation was confirmed by vibrational spectroscopy measurements.

4.4.2 Spectroscopic analysis of synthesised carbon nanostructures

As for the synthesised carbon nanostructures two well-resolved bands were observed in the Raman spectra of all of the samples obtained at all the variations in the technical parameters. The first band was centered at about 1325 cm^{-1} (known as the D band) and the second band was centered at about 1572 cm^{-1} (known as the G band). The D band centered at 1325 cm^{-1} has been attributed to the presence of the structural disorder of the graphitic carbon. However, in the present case, this band was attributed to the graphitic carbon point defects. The G band centered at 1574 cm^{-1} was attributed to the in-plane carbon-carbon stretching vibration of the graphitic layers. In addition to these two bands, a third band was also observed at 1605 cm^{-1} , as a shoulder of the G band. This band is known as the D0 band and was assigned to graphitic defects on the nano carbon. In the low-wavenumbers region, at about 200 cm^{-1} there is presence of weak peaks which correspond to Radial Breathing Modes (RBM). Apart from these bands a strong and broad band at about 2645 cm^{-1} corresponding to the 2D peak. The peak positions of these Raman bands were found to be the same irrespective of the reaction temperature but the morphology of the synthesized carbon nanostructures varied with variation in temperature. However, the relative intensity of one of the Raman bands was found to differ for different reaction temperatures. The crystallinity and graphitization degree can be further explained on the basis of I_D/I_G and I_D/I_{2D} values of the synthesized carbon nanostructures at various reaction temperatures, since it is an effective tool to assign the crystalline quality and graphitization degree of the grown carbon nanostructures as shown in figure 4.8. The calculated I_D/I_G values were found to be 0.95, 1.01 and 1.11 at 700, 800 and 900 °C, respectively, whereas the calculated values for I_D/I_{2D} were found to be 6.38, 8.50, 8.68 at 700, 800 and 900 °C, respectively. The calculated I_D/I_G and I_D/I_{2D} values were found to be 1.04 and 9.35 for the flakes obtained at 900 °C. These values of I_D/I_G and I_D/I_{2D} being corresponding with each other with increase of the temperature indicates a consistent crystalline quality and a progressive graphitization of the synthesized carbon nanomaterials with increase of temperature. Thus, a higher graphitization degree was observed for the nano carbon synthesized at 900 °C. The micro Raman spectroscopic analysis on these

carbon nanomaterials synthesised with increasing temperature are on good agreement with XRD and ESEM results providing the significant evidence about the breakage of CNT in carbon spheres.

In the second case of experiments, in figure 4.9 with C_2H_4 , the intensity of one of the Raman bands was found to differ for different reaction temperatures. At 700 °C it shows the formation of very thick MWCNTs with some intense of the 2D band but as we increase the temperature, the formation of MWCNTs decreases and the more degree of graphitization is obtained, a there is an increase in the intense of the D band and decrease in G band and 2D band nearly disappears. On the flakes, obtained from walled of quartz tube, the Raman spectrum shows the formation graphitic carbon, which was carried on the carbon spheres. Further, in the third case, Raman spectroscopic measurements were carried out on the synthesized, when Ar/ H_2 was flown 15 min along with the C_2H_4 , 30 min at 700 °C at shown in figure 4.10. The calculated I_D/I_G value was found to be 1.02, whereas the calculated value for I_D/I_{2D} was found to be 2.85, respectively. Thus, the flow of H_2 along with the C_2H_4 gives in the better formation of MWCNTs. These results are in good relevance with our ESEM images for these synthesized samples.

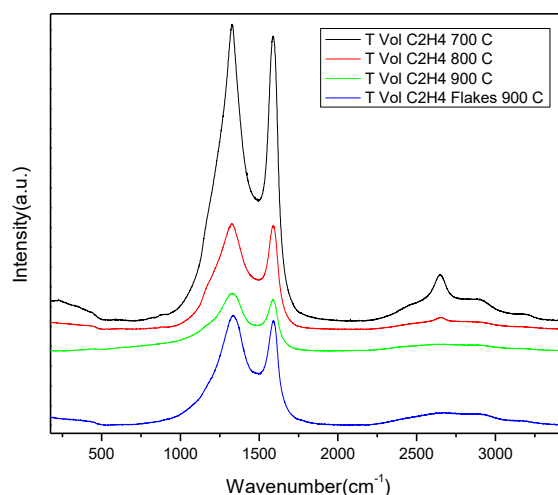


Figure 4.8 Micro Raman spectra of carbon nanostructures on limonite laterite powder ore after dehydration via C_2H_4 decomposition.

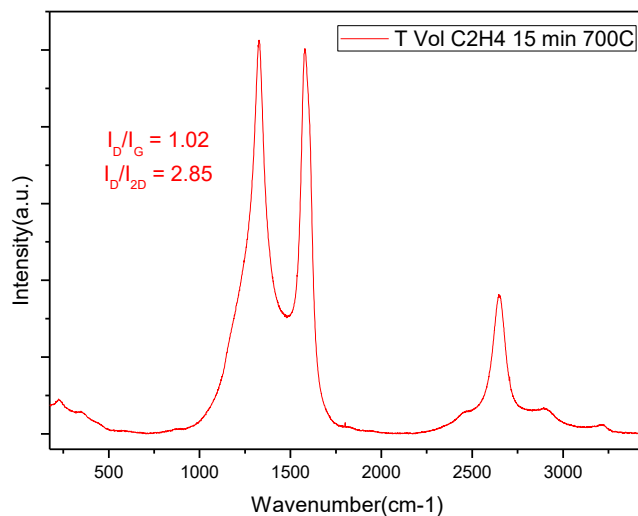


Figure 4.9 Micro Raman spectrum of MWCNTs grown with Ar/H₂, 100/400 sccm for 15 min along with C₂H₄ flow 100 sccm for 30 min at 700 °C.

In the fourth case, when, the raw samples were used as a catalyst with and without Ar/O₂ along with Ar/H₂ and C₂H₄ decomposition, the micro Raman spectroscopic measurements were carried out as shown in figure 4.10. There is a presence of RBM in both experiments in this case. Further, the calculated I_D/I_G value was found to be 0.82 and 1.0, with and without Ar/O₂ whereas the calculated value for I_D/I_{2D} was found to be 1.09 and 1.34, with and without Ar/O₂ respectively. These results give us the conformation of the formation of carbon nanotubes. Further, the flow of Ar/O₂ along with the C₂H₄ and Ar/H₂ gives in the better formation of MWCNTs. These results are in good relevance with our ESEM images for these synthesized samples.

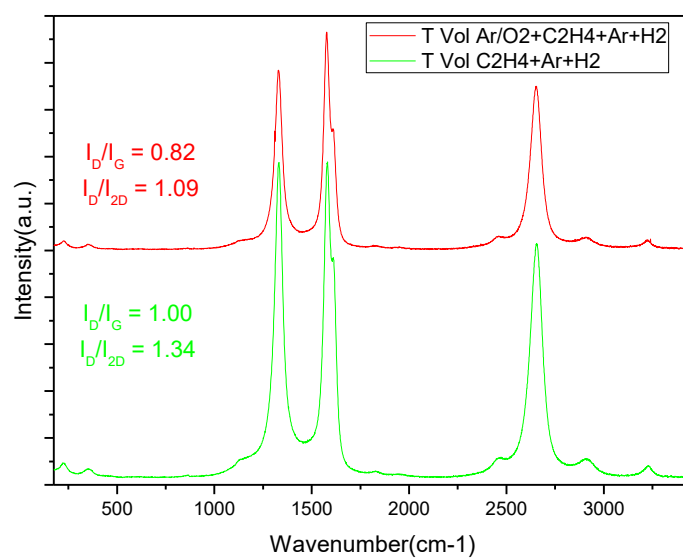


Figure 4.10 Micro Raman spectra of MWCNTs deposited via flow of ethylene, C₂H₄ with Ar/H₂ and Ar/O₂ 100 sccm (above) and C₂H₄ with Ar/H₂ (below) at the temp. of 770 °C in the first zones and 750 °C in the third zone.

4.5 Conclusions

We have successfully demonstrated the synthesis of carbon nanostructures using natural limonite laterite as a catalyst at 700, 800 and 900 °C using ethylene which could be easily produced in large scale. Further, we have studied the synthesis of CNTs (10-100 nm)/CSs (500-700nm) heterostructures with uniform and periodic beaded CS morphologies via CVD using natural limonite laterite powder as catalyst. The experimental results indicate that by amending the temperature inside the CVD furnace, morphology from uniform CNTs, perturbation and then breakage to periodic beaded CSs via catalytic performance. Further, the mechanism has also been discussed in some details for changing the morphology from nanotubes to spherical particles under temperature conditions. Further, when Ar/O₂/H₂ was flown along with the C₂H₄, at 700-800 °C, this results in the better formation of MWCNTs. The obtained results are in good agreement with all the characterisation techniques. They provide an efficient and simple growth process of carbon nanomaterials from the natural limonite laterite and indicate the potential scaling up to the large scale production due to easy availability of catalyst material sources. Our results indicate that the uses of natural mineral oxides for the synthesis of carbon nanostructure can be a suitable approach to scale up the production for specific technological applications.

4.6 References

1. K. Abe, G. Saito, T. Nomura, T. Akiyama, *Energy & Fuels*, 2016, 30, 8457.
2. S. Gialanella, F. Girardi, G. Ischia, I. Lonardelli, M. Mattarelli, M. Montagna, *J. Therm. Anal. Calorim.*, 2010, 102, 867.
3. A. E. Awadallah, W. Ahmed, M. R. N. El-Din, A. A. Aboul- Enein, *Appl. Surf. Sci.*, 2013, 287, 415.
4. J. Ashok, G. Raju, P. S. Reddy, M. Subrahmanyam, A. Venugopal, *Int. J. Hydrogen Energy*, 2008, 33, 4809.
5. D. Kang, J. W. Lee, *Appl. Catal., B*, 2016, 186, 41.
6. T. V. Reshetenko, L. B. Avdeeva, V. A. Ushakov, E. M. Moroz, A. N. Shmakov, V. V. Kriventsov, D. I. Kochubey, Y. T. Pavlyukhin, A. L. Chuvilin, Z. R. Ismagilov, *Appl. Catal., A*, 2004, 270, 87.
7. A. F. Cunha, J. J. M. 'Orf~ao, J. L. Figueiredo, *Fuel Process. Technol.*, 2009, 90, 1234.
8. A. E. Awadallah, A. A. Aboul-Enein, D. S. El-Desouki, A. K. Aboul-Gheit, *Appl. Surf. Sci.*, 2014, 296, 100.
9. N. Bayat, M. Rezaei, F. Meshkani, *Int. J. Hydrogen Energy*, 2016, 41, 1574.
10. M. Pudukudy, Z. Yaakob, Z. S. Akmal, *Appl. Surf. Sci.*, 2015, 330, 418.
11. C. Zhang, J. Li, C. Shi, E. Liu, X. Du, W. Feng, N. Zhao, *Carbon*, 2011, 49, 1151.
12. F. A. Nichols, WW Mullins, *Trans AIME* 1965, 233, 1840.
13. F.A. Nichols . *J Mater Sci.* 1976, 11, 1077.
14. J. A. Tang, M. Valix, *Miner. Eng.* 2006, 19, 1274.

CHAPTER: 5

Growth of carbon nanostructures using siliceous breccia powder as catalyst via ethylene decomposition

5.1 Introduction

The first part of this chapter deals with the catalyst preparation and the synthesis of carbon nanostructures on the natural siliceous breccia powder containing mainly quartz and some traces of hematite and goethite. In the second part it reports on the results of morphology investigations, micro-structural properties characterization and vibrational spectroscopic behaviour of the synthesized carbon nanostructures. Furthermore, a series of syntheses as a function of the H_2/C_2H_4 ratio supplied into the catalyst which modifies the rate of formation of carbon nanostructures has been carried out. The obtained results suggest that siliceous breccia powder is an effective candidate towards the low cost and easy approach for the CNTs/CNFs.

5.2 Synthesis of carbon nanostructures by chemical vapour deposition

In this study, we have used natural siliceous breccia samples were in form of powders having particle size less than 80 μm and come from New Caledonia mines drilled. Figure 5.1 shows the sketch of the sample preparation for the surface roughness analyses. The optical images sonic drilled cores breccia and the powdered sample ($< 80 \mu m$) of the breccia are shown in figure 5.2. Further, Table 5.1 reports the elemental composition of the natural drill core siliceous breccia powder. The elemental composition of the natural drill core siliceous breccia powder was determined using EDX. Both the ESEM image of the sample micro-region where the EDX analysis was carried out and the related EDX spectrum are reported in figure 5.3 and figure 5.4, respectively. The sample was found to contain Si, Fe, Mg, and O as the elements. The peak for Au arose from the Au coating done before performing the ESEM/EDX analysis.

Code 5 surface states for solid cores:

a.1 • as-drilled



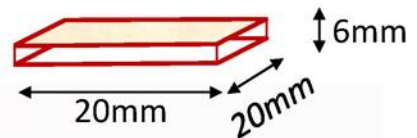
a.2 • as-cut



a.3 • Polished @ $6\mu\text{m}$



a.4 • Polished @ $.25\mu\text{m}$



a.5 • Powdered $< 80\mu\text{m}$



Figure 5.1 Sketch of the sample preparation for the surface roughness analyses.

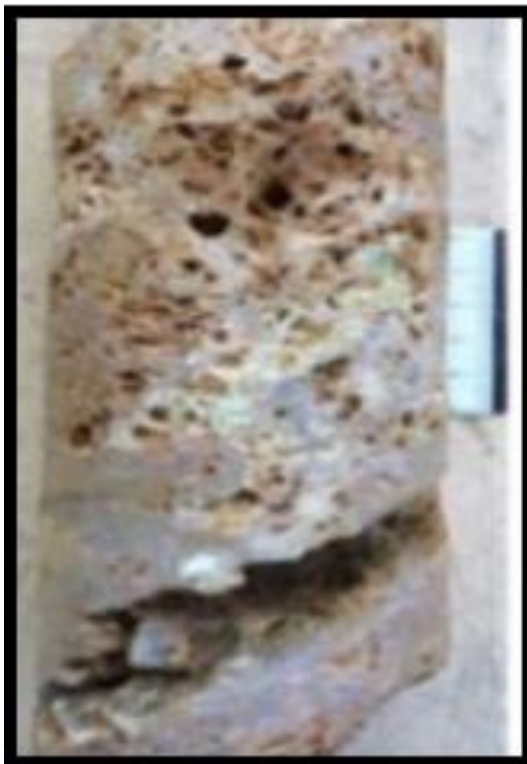


Figure 5.2 Optical images Sonic drilled cores breccia (left) and the powdered sample ($< 80\mu\text{m}$) of the breccia (right).

Table 5.1 Average elemental Compositions of the natural siliceous breccia powder used in this study.

Element	Wt%	At%
OK	45.59	59.57
MgK	00.75	00.65
SiK	53.26	39.64
CrK	00.00	00.00
FeK	00.39	00.15
NiK	00.00	00.00
AuL	00.00	00.00
Matrix	Correction	ZAF

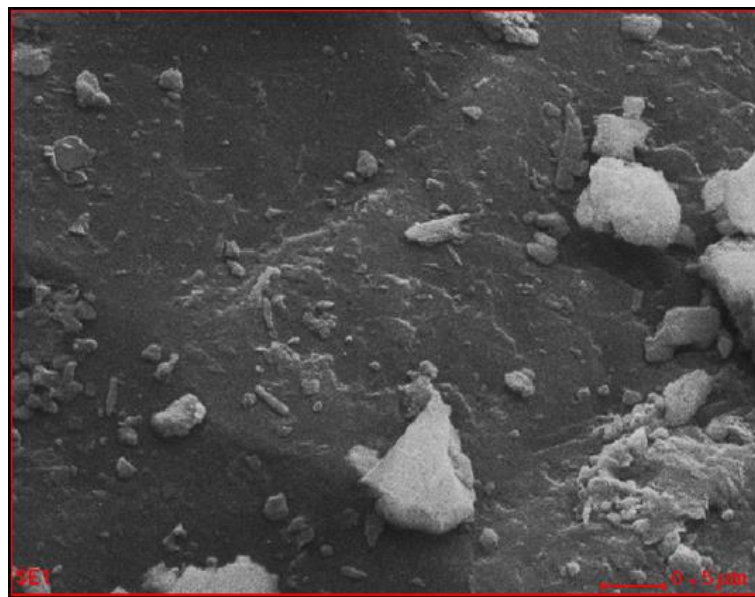


Figure 5.3 ESEM Micrograph for the EDX spectrum of the natural drill core siliceous breccia powder.

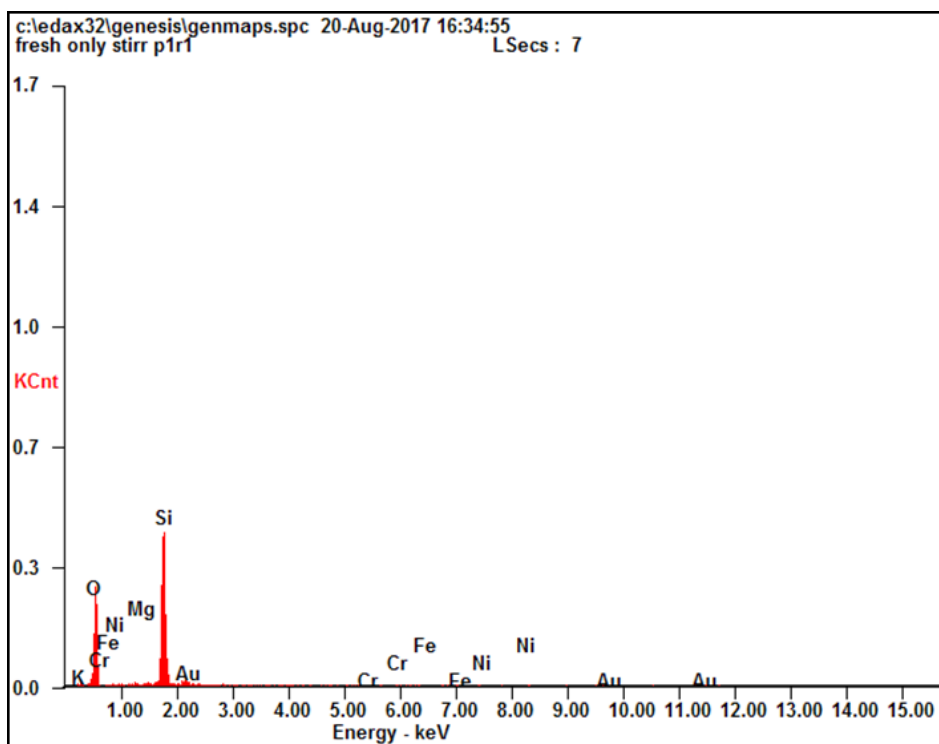


Figure 5.4 EDX spectrum of the natural drill core siliceous breccia powder.

5.2.1 Sample preparation and carbon nanostructure formation

The natural drill core siliceous breccia powder with $< 80\mu\text{m}$ size was weighed to 50 mg and loaded in the quartz boat and was purged with the 300 sccm Ar gas for 30 min in the chemical vapour deposition (CVD) furnace. Next, the raw sample was reduced under Ar/H₂ 100/400 sccm for 15 min at 700 °C. In the first reaction, we have flown C₂H₄/H₂ 100/30 sccm at the temperature of 700 °C for 30 min. In the next experiment, we have flushed C₂H₄ 100 sccm at the temperature of 700 °C for 30 min. During the course of the reaction, the outlet gases were collected in bubbler. After the 1 hour of reaction, the quartz tube was shifted out of the furnace and was cooled to room temperature under a low flow of Ar (100 sccm). Finally the carbon deposited over the catalyst was collected for the analysis. The flow of all types of gases was maintained constant using an electronic mass flow controller (MKS 247D). The summary of protocol for synthesis of carbon nanostructures on natural drill core siliceous breccia powder is shown in figure 5.5.

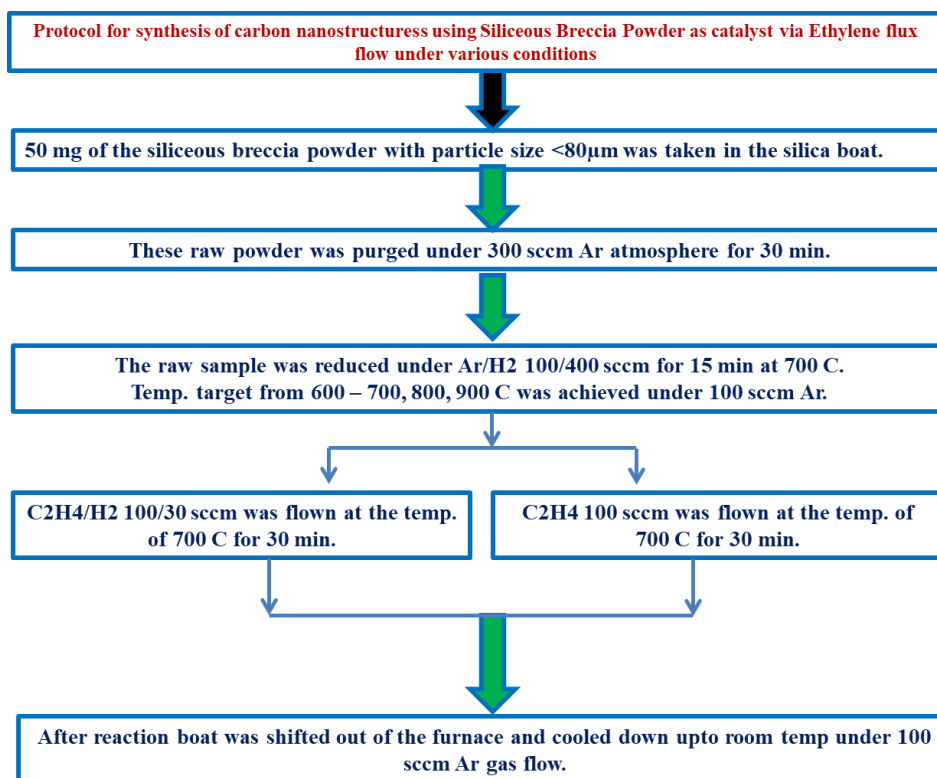


Figure 5.5 Protocol for the synthesis of carbon nanostructures using natural siliceous breccia powder.

5.3 Characterization of natural drill core siliceous breccia and synthesized carbon nanostructures

The raw and ethylene decomposed catalysts were characterized by using different techniques. The crystal structure and phase purity of the fresh and spent samples were determined by powder X-ray diffraction (XRD) using a Bruker D8 Advance diffractometer with a Cu K α radiation wavelength of 1.54 Å as the X-ray source. The samples were scanned from 20 to 80 degrees (2 θ) with a step size of 0.025 degrees. The mean crystalline size of the oxide phase of the calcined powders was calculated from the full widths at half maximum of the intense X-ray diffraction peaks using Scherrer's equation. The morphology of the calcined catalyst and of the synthesized carbon nanomaterials samples was observed using an environmental scanning electron microscope (ESEM) at an operating voltage of 3 kV equipped with an energy dispersive X-ray (EDX) analyser instrument to determine the elemental composition of the raw and of the as-obtained catalyst

after calcination. Further, the vibrational properties of the raw natural low-Ni containing iron ore powders were investigated by means of micro-Raman and FTIR spectroscopies.

Systematic micro Raman measurements on the fresh catalyst and nano carbon deposited at different temperature were carried out by means of a single stage Horiba-Jobin Yvon spectrometer (model LABRAM HR800) operated in the same conditions as described in chapter 3. FT-IR spectra were obtained at room temperature in the spectral range between 400 cm^{-1} and 4000 cm^{-1} using a JASCO spectrometer model FT/IR-660 plus as described in chapter 3.

5.4 Results and discussion

The structural and microstructural characterizations along with surface morphology were carried out by X-ray Diffraction (XRD), Environmental Scanning electron microscopy (ESEM). The spectroscopic characterization of siliceous breccia sample and the as synthesized carbon nanostructures were investigated by micro Raman spectroscopy and FTIR spectroscopic techniques.

5.4.1 Structural/microstructural characterizations

The natural drill core siliceous breccia sample and the as synthesized carbon nanostructures have been characterized by XRD, ESEM techniques. The results obtained from above techniques are hereafter presented and discussed.

5.4.1.1 Gross structural characterization

X-ray Diffraction (XRD) technique was used to characterize gross structural analysis as well as phase purity of the natural raw siliceous breccia powder as shown in figure 5.6. Before the XRD measurement, the diffractometer was calibrated with silicon powder ($d_{111}=3.1353\text{ \AA}$). The crystal structure and phase purity of the raw natural siliceous breccia powder was studied using X-ray diffraction (XRD), and the XRD patterns are shown in figure 5.6. Table 5.2 reports the XRD pattern, in terms of the angles at which the major diffraction peaks occur and corresponding d-spacing, recorded on the siliceous breccia powder used in this study. According to XRD powder analyses, the sample

contains 100 wt. % of quartz with traces of hematite and goethite, the diffraction pattern is completely in correlation with ruff data base RRUFF ID R100134.9 [1].

Table 5.2 Experimental diffraction angles and corresponding d-spacing of the siliceous breccia powder used in this study.

2 Θ (Degrees)	d-spacing (\AA)
20.77	4.27
26.55	3.35
36.46	2.46
39.39	2.28
42.37	2.13
50.06	1.82
59.88	1.54

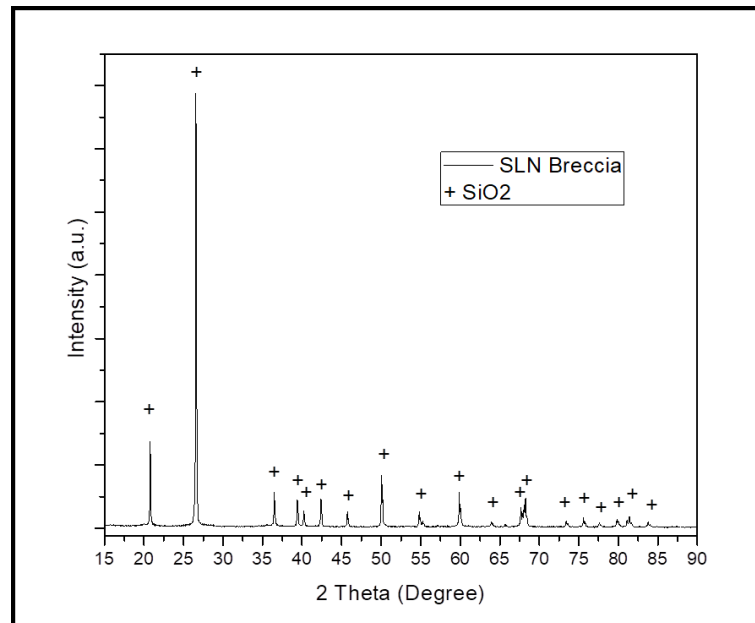


Figure 5.6 XRD patterns of the natural drill core siliceous breccia.

5.4.1.2 Surface morphology

The surface morphology has been investigated by environmental scanning electron microscopy (ESEM) technique. Figure 5.7 represents the, ESEM images of natural drill core siliceous breccia with different magnifications. The ESEM images of the magnified view of the natural siliceous breccia powder clearly showed a high crystalline morphology.

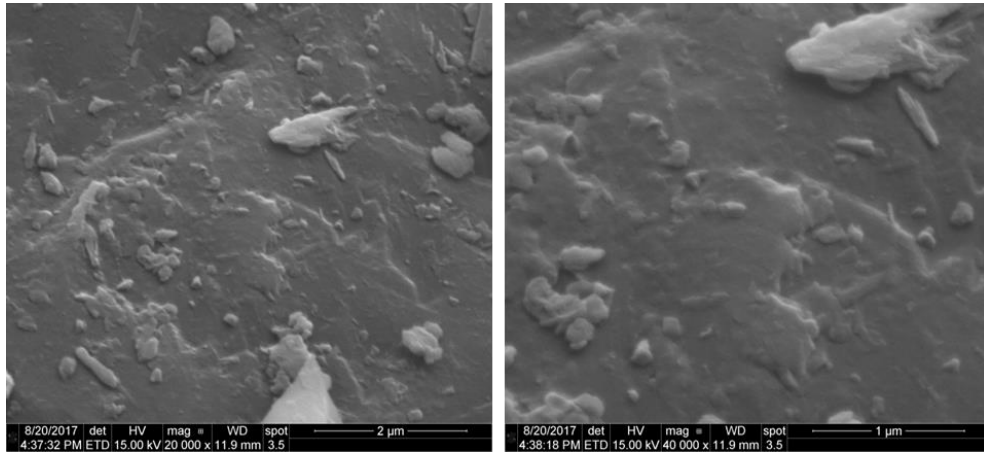
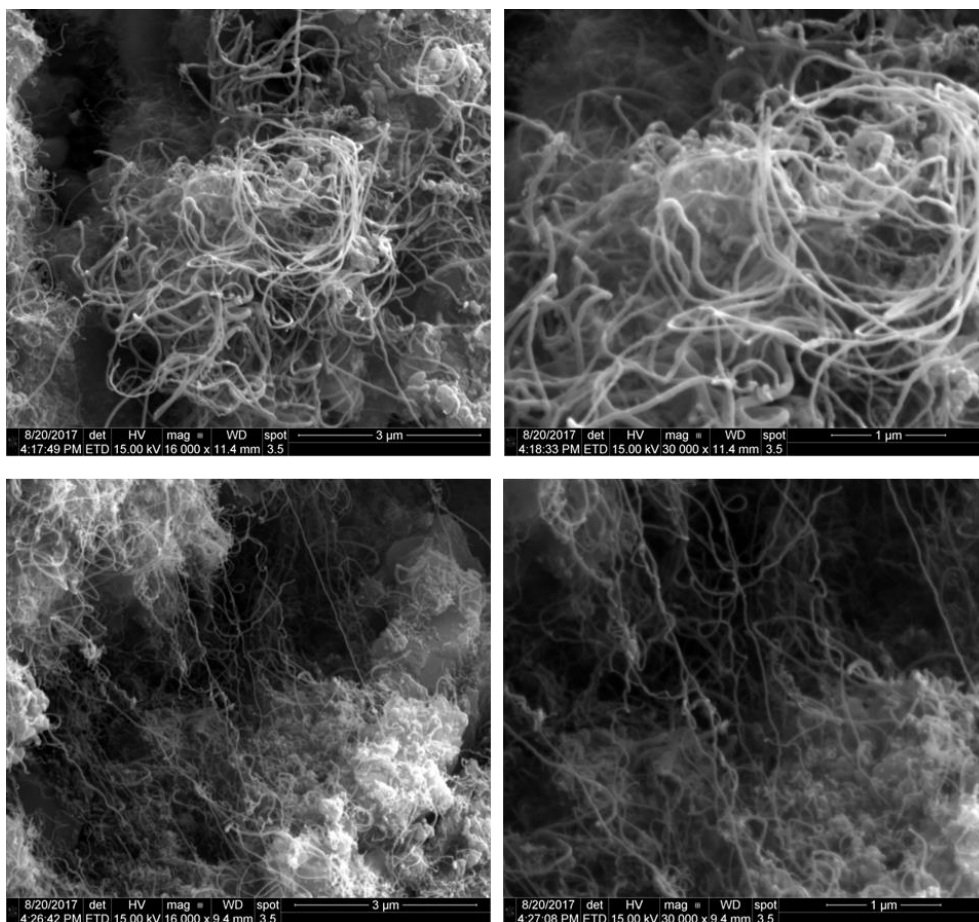
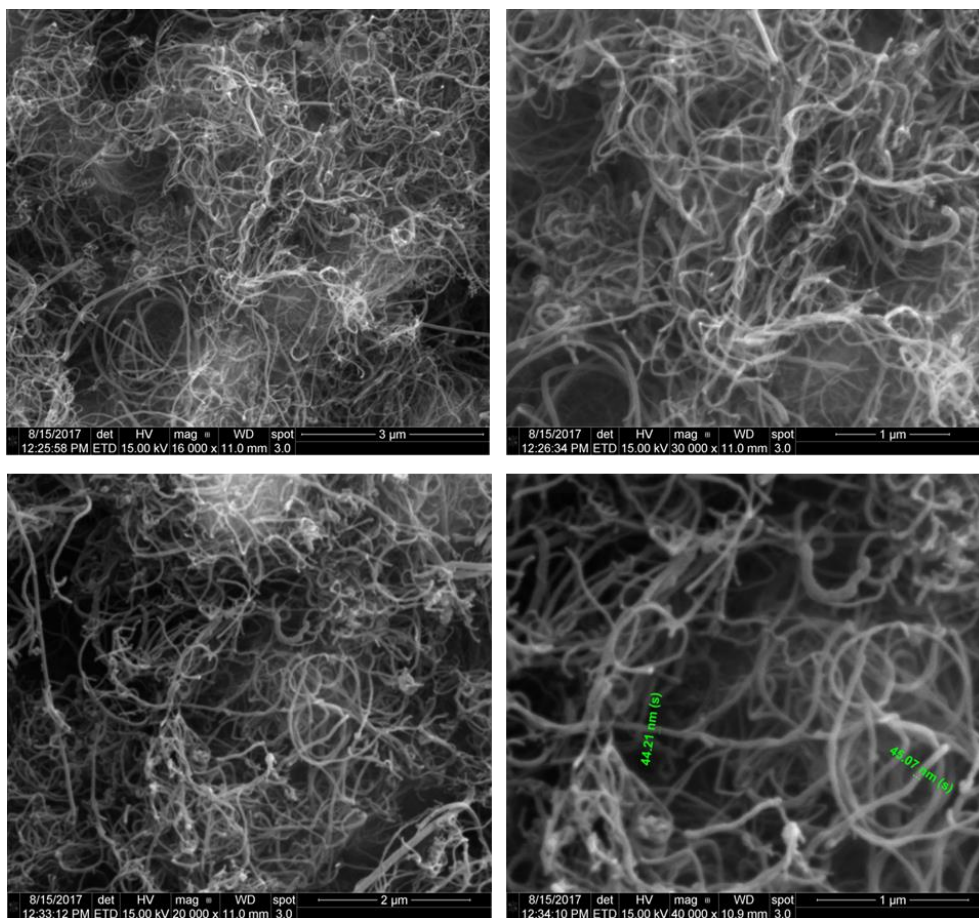


Figure 5.7 ESEM micrographs on the natural siliceous breccia powder with different magnifications.

Figure 5.8 represents the, ESEM images with different magnifications of the MWCNTs over natural siliceous breccia powder deposited by 100 sccm ethylene (C_2H_4) with and without 30 sccm H_2 , respectively, using chemical vapour deposition method. The images show clearly nanotubes like structures connected with each other in a bundle formation. The average diameter of the MWCNTs varies from 10-50 nm.



(a) ESEM images of MWCNTs via C_2H_4/H_2 100/30 sccm flushed at the temperature of 700 °C for 30 min.



(b) ESEM images of MWCNTs via C_2H_4 100 sccm flushed at the temperature of 700 °C for 30 min.

Figure 5.8 ESEM images of MWCNTs; ESEM images of MWCNTs via C_2H_4/H_2 100/30 sccm flown at the temp. of 700 °C for 30 min (a); ESEM images of MWCNTs via C_2H_4 100 sccm flushed at the temperature of 700 °C for 30 min (b).

Furthermore, the presence of quartz and goethite in the drill core natural siliceous breccia powder and growth of high quality MWCNTs were confirmed by vibrational spectroscopy measurements.

5.4.2 Spectroscopic Analysis of natural siliceous breccia powder and synthesized carbon nanostructures

5.4.2.1 Micro Raman spectroscopic Analysis

The vibrational properties of natural siliceous breccia powder were studied using micro Raman spectroscopy and the observed Raman spectra are shown in figure 5.9. Figure 5.9 shows two experimental spectra obtained from the drill core siliceous breccia powder. In general, the as-observed spectra consisted of a well resolved Raman over imposed a broad, continuous luminescence background which was subtracted using the Horiba LabSpec 5 baseline correction. The as-obtained Raman spectra were then compared with reference spectra of the RRUFF database. The peaks of the as-obtained Raman spectrum are well matched with the RRUFF data base for goethite, FeO(OH) and quartz, SiO₂. Quartz is found to be the main phase during the repeated measurements carried out on the natural siliceous breccia powder. Further, some traces of Goethite were also found. A very strong band of quartz is located at around 461 cm⁻¹ and two weak bands appear at around 367 and 248 cm⁻¹. The band at around 462 cm⁻¹ corresponds to the A₁ vibration mode characteristic of quartz [2]. The spectrum of goethite consists of a set of bands peaked at about 147, 231, 301, 389, and 676 cm⁻¹. The peak positions of the bands and, in particular, of the band at 301 cm⁻¹ and that of the strongest one at 389 cm⁻¹ agree with the values reported in the literature. The narrow band at 301 cm⁻¹ is assigned to the symmetric bending vibration of Fe-OH, whereas the band at 389 cm⁻¹ is ascribed to the symmetric stretching vibration of Fe-O-Fe/-OH [3,4]. The bands at 231 and 676 cm⁻¹ are assigned to the Fe-O A_{1g} mode and Fe-O stretching, respectively [5].

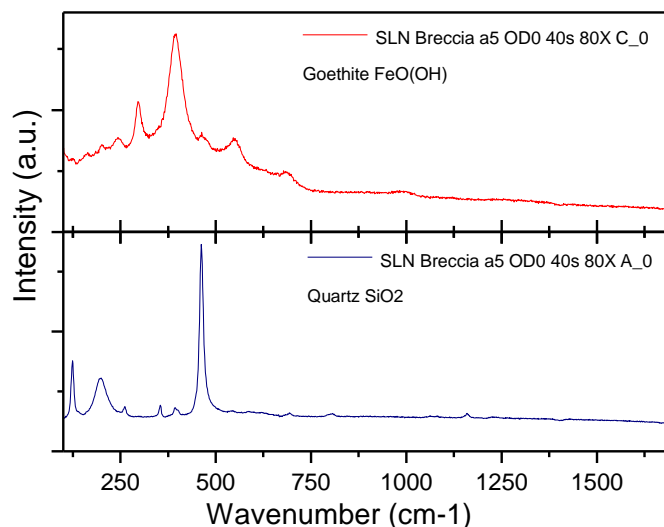


Figure 5.9 Raman spectrum of natural siliceous breccia powder.

As for the synthesised carbon nanostructures, two well-resolved bands were observed in the Raman spectra of all of the samples obtained at each of the reaction temperatures. The first band was centered at about 1330 cm^{-1} (known as the D band) and the second band was centered at about 1584 cm^{-1} (known as the G band). The D band centered at 1330 cm^{-1} should be ascribed to the structural disorder, mainly due to point defects, within the graphitic layers of carbon nanostructures. The G band centered at 1584 cm^{-1} was attributed to the in-plane carbon-carbon stretching vibration of the two adjacent graphitic layers. In addition to these two bands, a third band was also observed at 1609 cm^{-1} , as a shoulder of the G band. This band is known as the D' band and could be due to defects outside the graphitic layers of the nano carbon.

In the second case, where C_2H_4 was flushed without mixing H_2 , the positions of the Raman bands were found distinguishable with the previous set of experiment irrespective of the reaction temperature being the same and also of the morphology of the deposited nano-carbon. However, the intensity of one of the bands was found to differ for different reaction temperatures. The first band was centered at about 1330 cm^{-1} (known as the D band) and the second band was centered at about 1594 cm^{-1} (known as the G band). No additional shoulder band of the G band was observed in this case as compared to the first case. Also, not

much appreciable change in the intensity of the G band was noticed in this case. These results indicated that the structural imperfections of the graphitic carbon nanostructures decreased as the reaction temperature was increased.

The crystallinity and graphitization degree can be further explained on the basis of the ratio value I_D/I_G of the synthesised carbon nanostructures at various reaction temperatures, since it is an effective tool to assess the crystalline quality and graphitization degree of the synthesised carbon nanostructures. The calculated I_D/I_G values were found to be close to 1.1. These values being quite small and close to unity suggest a high degree of crystalline quality of graphitization of the deposited nano-carbon. The smaller the I_D/I_G value, then the higher is the graphitization degree. The decreased I_D/I_G value with increasing reaction temperature indicated the deposition of the well-ordered graphitic carbon to be better than the deposition of the defective carbon species. The same trend is observed by using the ratio of intensities of the D and G' bands, $I_D/I_{G'}$. Thus, in the present case, a higher graphitization degree was observed for synthesised carbon nanostructures without H_2 mixing with the C_2H_4 at 700 °C.

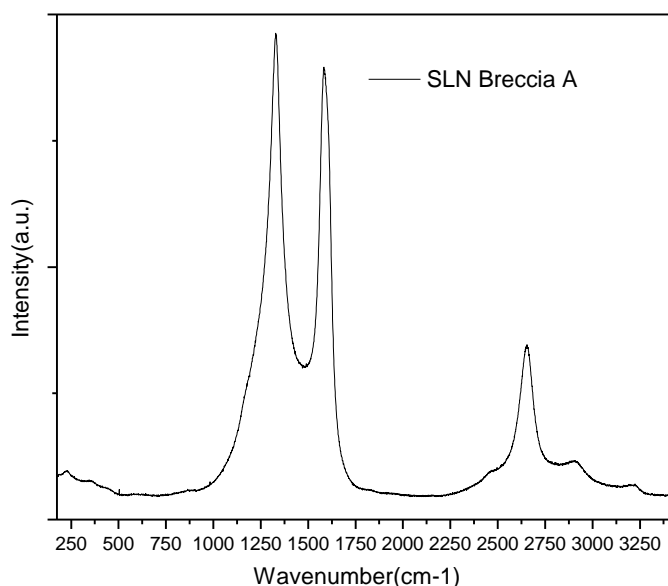


Figure 5.10 Micro Raman Spectrum of MWCNTs grown via C_2H_4/H_2 100/30 sccm flown at 700 °C for 30 min.

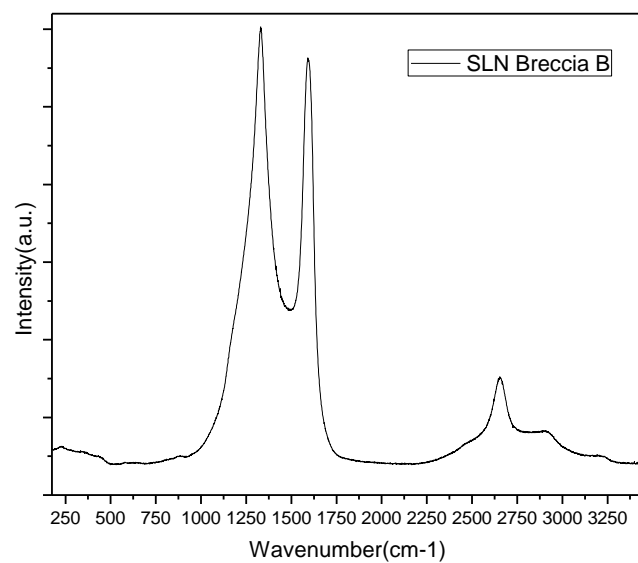
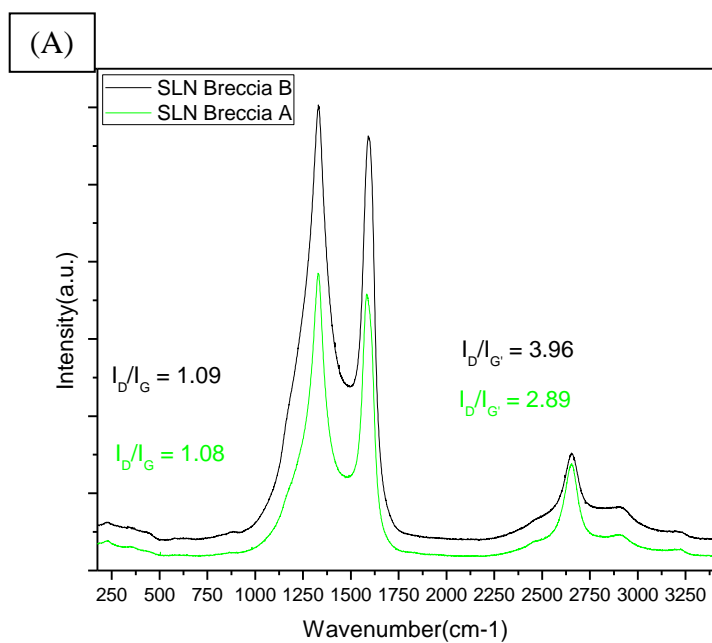


Figure 5.11 Micro Raman Spectrum of MWCNTs grown via C_2H_4 100 sccm flown at the temp. 700 °C for 30 min.



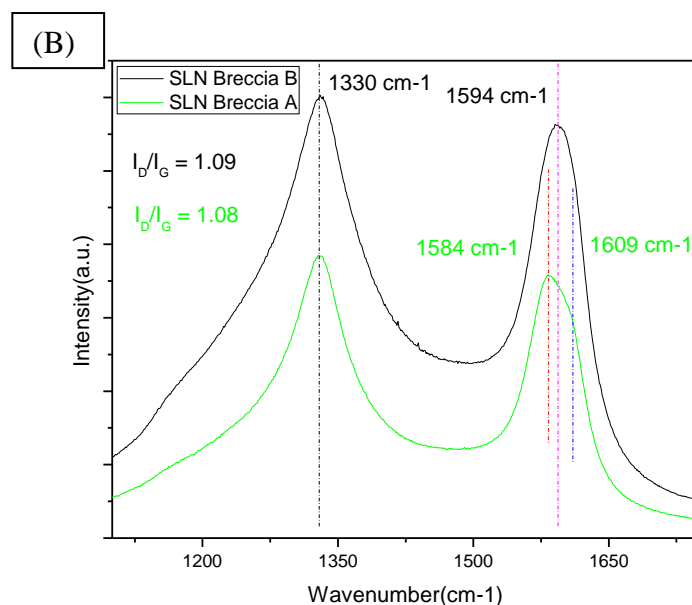


Figure 5.12 (A) & (B) Comparison of Micro Raman Spectrum of MWCNTs grown via C_2H_4 with and without H_2 mixing flown at the temp. 700 °C for 30 min.

5.4.2.2 FTIR (Fourier transform infrared) spectroscopy) of siliceous breccia

FTIR spectroscopy was also exploited to assess the quality of the natural siliceous breccia powder used as catalyst. Figure 5.13 shows the FTIR spectrum of siliceous breccia powder. Several distinct bands in the 400-4000 cm^{-1} region were observed which correspond siliceous breccia powder. The characteristic structural vibrations in the FTIR spectra (figure 2) were studied, and three main vibrational bands were identified: (1) Si-O bending vibration at 470 cm^{-1} and 515 cm^{-1} for alpha-quartz [3] (2) Si-O-Si symmetrical stretching vibration at 780 cm^{-1} and 799 cm^{-1} as a doublet for alpha-quartz, which are its characteristic vibrations; (3) Si-O-Si asymmetrical stretching vibration is located at 1098 cm^{-1} for alpha-quartz. The obtained result is consistent with earlier results obtained with the other characterization techniques.

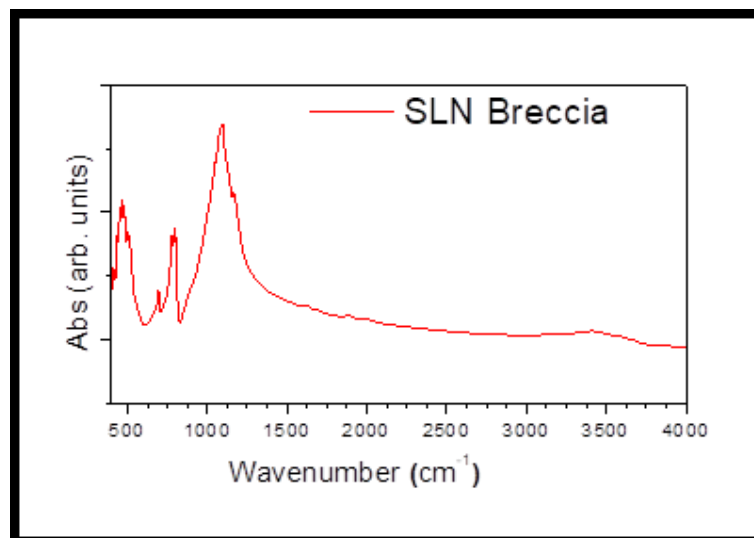


Figure 5.13 FTIR spectrum of siliceous breccia powder.

5.5 Conclusions

We have successfully carried out the growth of carbon nanostructures on siliceous breccia powder as catalyst via C_2H_4 decomposition under various conditions. Further, the combination of ESEM and micro-Raman spectroscopic analysis provides a clear picture of both the chemical and phase composition of the analysed samples.

5.6 References

1. <http://rruff.info/quartz/source/asc/R100134>
2. D. Krishnamurti, Proc. Math. Sci. 1958, 5, 276.
3. D. Faria, S. Silva, M. Oliveira, J. Raman Spectrosc. 1997, 28, 873.
4. M. Hanesch, J. Int. Geophys. 2009, 177, 941.
5. M.A. Legodi, D. Waal, Dyes Pigm. 2007, 74, 161.

CHAPTER: 6

Combined analysis & growth of graphitic layers on Cu substrate from black shale carbon powder as precursor

6.1 Introduction

In this chapter, we deal with two cases of drilled core organic matter rich black shale carbon samples. First case, deals with the results of combined spectroscopic analyses performed on a sample extracted from a core drill obtained from a geological survey for raw materials mining purposes. The aim of the work was to detect the major mineral component phases following an experimental protocol including both combined mineralogical and chemical analyses, which are necessary for resource and reserve estimates during mine operation. This study provided different challenges: 1) micrometric grain size; 2) chemical bonding of organic matter; 3) the presence of fine inter-grown clay minerals, sulphides quartz and carbonates. To this aim, both micro-Raman as well as Energy dispersive X-Ray spectroscopy tests were carried out in a complementary way. The sample, in form of a solid bar with a very dark/black colour, was labelled as BC6 (18/84, 60 m), and, according to the provider (the French mining and metallurgical group ERAMET), it consists of sulphur minerals, mainly pyrite.

Further, in the second case, black shale carbon powders, mainly contain minerals like quartz and dolomite, were exploited to obtain coating layers, on Cu substrates. The shape dependent structural/microstructural characteristics and vibrational properties of the pristine black shale powders and the graphite layers deposited on Cu substrates by using the same powders as precursor have been explored in detail. Furthermore, comparative studies by varying the temperature and the different Cu substrates as catalysts.

The results of first case were presented as the ‘Combined Raman and EDXS Analyses on Drill Core Samples’; **Arun Kumar**, Marco Giarola, Nicola Daldosso, Marco Zanatta, Gino Mariotto, Andrea Sanson, Maurizio Montagna, Maria Secchi, Evgeny Borovin, Mauro Bortolotti, Stefano Gialanella, Luca Luterotti; at II International Conference on Applied Mineralogy & Advanced

Materials & XIII International Conference on Applied Mineralogy, Castellaneta Marina (Taranto), Italy from June, 5-9, 2017; Vol. 6, p. 53, 2017; ISSN 2464-9147 (Online); Applied Mineralogy & Advanced Materials AMAM-ICAM 2017.

6.2 Organic matter rich carbon shale material origin, specification & synthesis of graphitic layers on Cu by chemical vapour deposition

We have firstly studied an organic matter rich black shale carbon sample (BC6), as the protolith of the Mn-laterite deposit in SW Gabon (ERAMET-COMILOG), the 3rd world's Mn-producer. The aim of this work was to establish a reliable experimental protocol allowing the detection and identification of the major mineral phases and organic matter phases present in it. The optical image of this sample (BC6) is shown in Fig. 6.1.

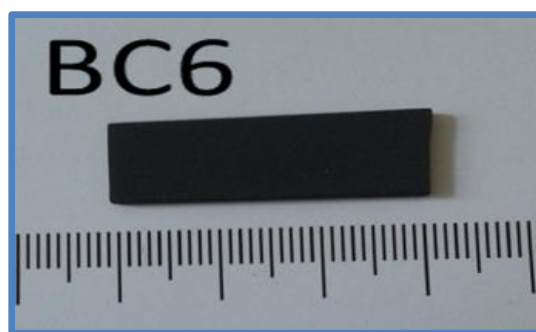


Figure 6.1 Optical image of the organic matter rich black shale (BC6).

Further, we have used a second natural organic matter rich black shale carbon powder sample (BC4), provided to us under the part of the EU H2020 SOLSA project (www.solsa-mining.eu). Table 6.1 shows the elemental composition of the natural organic matter rich black shale carbon powder. The optical images sonic drilled cores organic matter rich black shale and the powdered sample ($< 80 \mu\text{m}$) are shown in figure 6.2. The elemental composition of the natural drill core organic matter rich black shale carbonate powder was studied using EDAX, and the HRSEM image of the place where the EDX analysis

was carried out and the elements obtained are shown in figure 6.3. The sample was found to contain Si, Fe, Mg, and O as the elements. Figure 6.4, shows the quantitative analysis of the BC4 drill core organic matter rich black shale carbonate powder on the basis of EDX analysis.



Figure 6.2 Optical images of sonic drilled black shale core (left) and of the powdered sample (< 80 μm) of the carbonate shale (right).

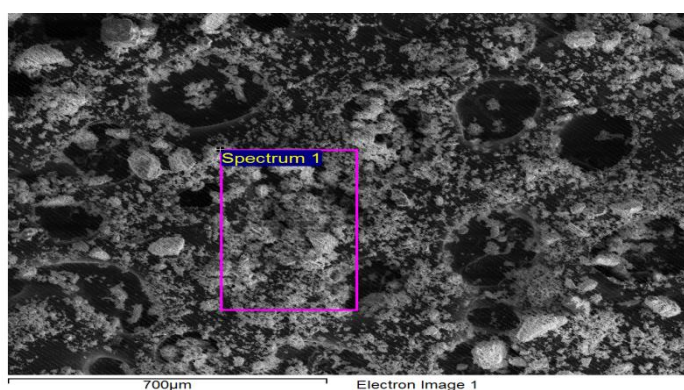


Figure 6.3 ESEM Micrograph-of the natural drill core powdered sample.

Sample/Elements(at%)	C	Mg	Al	Si	S	Ca	O
BC4	22.89	2.77	0.88	5.05	0.29	3.64	64.48

Table 6.1 Table of average elemental composition from EDX analysis of the natural drill core organic matter rich black carbon powder.

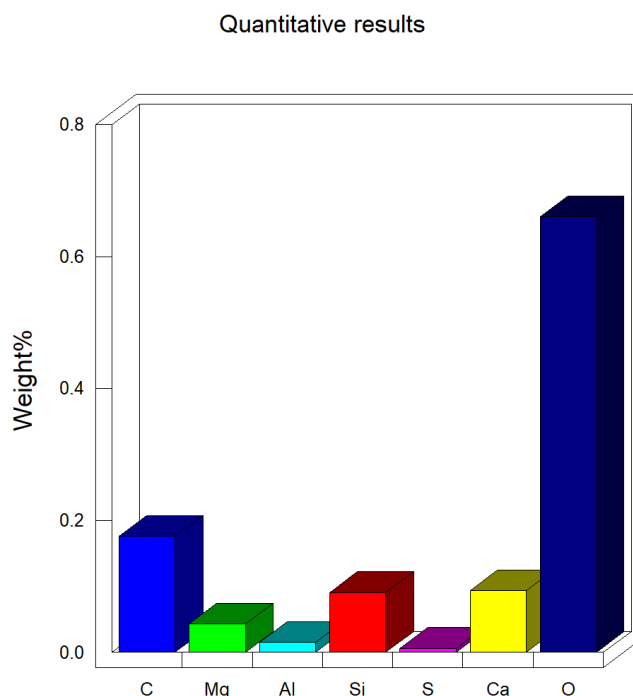


Figure 6.4 Quantitative analysis of the BC4 on the basis of EDAX analysis.

6.2.1 Sample preparation and synthesis of graphitic layer on Cu

We synthesised graphitic layers on the Cu substrate using a three-zone atmospheric-pressure CVD furnace. The CVD furnace was equipped with a fused-silica (quartz) tube with an internal diameter of 22 mm. Furnace temperatures were monitored using built-in furnace thermocouples with a microprocessor based temperature and gas flow controller with an accuracy of ± 1 °C. During the growth, the temperatures were set at 600 °C for zones 1 (G1) and 2 (G2) and 800 °C for zone 3 (G3), respectively. The flow of argon and hydrogen (99.9999%, from Gas Technologies) was maintained using electronic mass flow controllers (MKS model P4B) with digital mass flow control unit (MKS model 247D). The synthesis was carried out in three steps. First, we placed a ceramic boat with 4 gm of natural black shale carbon powder outside of the furnace, upstream of the gas flow. We also positioned three Cu substrates, one was done using SiO₂ wafer and we deposited 500 nm of Cu in the e-beam evaporation. The second sample was done on SiO₂ wafer and we sputtered 700 nm of Cu. The third sample was a piece of copper foil with a 0.5 cm x 1.5 cm (Alfa Aesar, 99.9%) upstream, outside the

heated zone of the furnace. We purged the quartz tube with argon and hydrogen, while all the samples and the boat were kept at room temperature until the furnace reached equilibrium at the desired temperatures in all the three zones. Next, for graphitic layer synthesis, we pushed the quartz tube inside the furnace to position the Cu samples in the middle of the growth zone G3 (800 °C). We then introduced the natural organic matter rich black shale carbonate powder at the edge of the first zone G1 inside the furnace (600 °C) using an external magnet. We kept the boat inside the furnace for 30 minutes in order to complete the reaction. To end the process, we first pulled out the natural organic matter rich black shale carbonate powder boat from G1, and then shifted the quartz tube out of the furnace, allowing a fast cool down of the sample to room temperature, under a flow of argon and hydrogen before removing it from the furnace and exposing it to air. We used here the “fast heat” technique. Using this technique, we heated the sample to the desired temperature without exposing it to temperature ramp up or down. During the course of the reaction, the outlet gases were collected in bubbler. After the 1 hour of reaction, the quartz tube was shifted out of the furnace and was cooled to room temperature under a low flow of Ar (100 sccm) to collect the carbon deposited over the catalyst for its analysis. The flow of all types of gases was maintained using an electronic mass flow controller (MKS 247D). The summary of protocol for synthesis of graphitic layers on Cu substrate is shown in figure 6.5.

Protocol for synthesis of graphitic layer on Cu Substrate using natural black shale carbon powder as precursor

4 gm of the black shale powder with particle size $<80\mu\text{m}$ was taken in the silica boat as a precursor.

These raw powder was purged under 300 sccm Ar atmosphere for 30 min.

Positioned three Cu substrates G3 Cu with 500 nm & 700 nm on SiO₂ wafer by e beam evaporation and Cu foil 0.5x1.5 cm.

Ar/H₂ 100/30 sccm was flown at the temp. of 600,600 and 800 C in G1,G2 and G3 for 30 min.

After reaction boat was shifted out of the furnace and cooled down upto room temp under 300 sccm Ar gas flow.

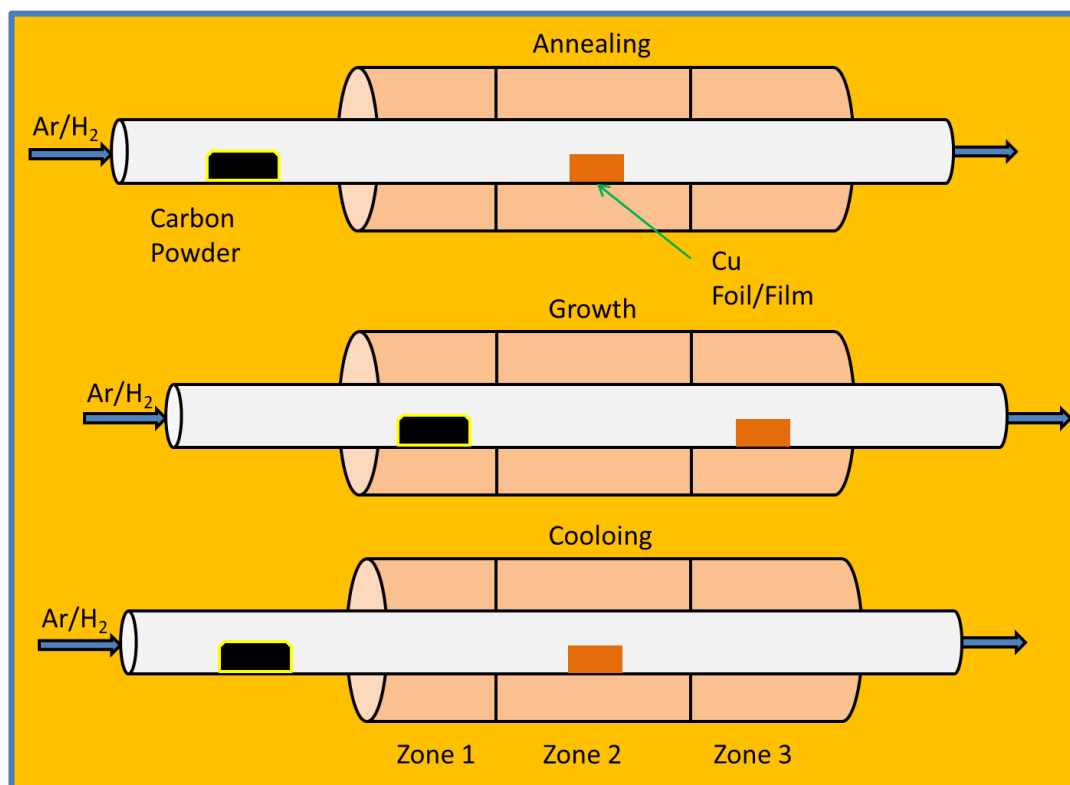


Figure 6.5 Protocol for the synthesis graphitic layer on Cu substrate.

6.3 Characterization of natural drill core black shale carbon powder and synthesised graphitic layers

The pristine natural black shale carbon powder and synthesised graphitic layers on Cu substrate were characterized by using different techniques. The crystal structure and phase composition of the fresh and synthesised samples was determined by powder X-ray diffraction (XRD) using a Bruker D8 Advance diffractometer with a Cu K α radiation wavelength of 1.54 Å as the X-ray source. The samples were scanned from 15 to 90 degrees with a step size of 0.03 degrees. The mean crystalline size of the oxide phase of the calcined sample was calculated from the full widths at half maximum of the intense X-ray diffraction peaks using Scherrer's equation. The energy dispersive X-ray spectra (EDXS) were acquired with a system (mod. Falcon Zaphire, EDAX) attached to a scanning electron microscope (SEM- mod. XL30, FEI) operated in a low-vacuum mode and using an accelerating voltage for the primary electrons of 20 kV. When the low-vacuum mode is used, the specimens can be observed in the as delivered conditions, with no need of surface coating with a conductive film, to prevent electrostatic charging, in case the observed sample was partially or fully non-conductive. Film coating would have been unacceptable in the present case for possible interference of the X-ray lines from the film (C or Au are typically used) and those coming from the underlying sample material. The morphological appearance of the synthesised graphitic layers sample was observed using a high resolution scanning electron microscope (HRSEM) at an operating voltage of 3 kV equipped with an energy dispersive X-ray (EDX) analyser instrument to analyse the elemental composition of the raw and as obtained catalyst after calcination. Further, the spectroscopic analysis of the raw natural organic matter rich black shale carbon powder sample, and graphitic layers deposited catalyst annealed was carried out using micro Raman spectroscopy by means of a single stage Horiba-Jobin Yvon spectrometer (model LABRAM HR800) operated in the same conditions as described in chapter 3.

6.4 Results and discussion

The structural and microstructural characterizations along with surface morphology were carried out by X-ray Diffraction (XRD), High Resolution Scanning electron microscopy (HRSEM). The spectroscopic characterization of pristine natural black shale carbon powder and the as synthesized graphitic layers on Cu were investigated by micro Raman spectroscopy and FT-IR spectroscopic techniques.

6.4.1 Structural/Microstructural characterizations

The natural drill core organic matter rich black shale carbon powder and the as synthesised graphitic layers have been characterized by XRD, HRSEM, techniques.

6.4.1.1 Gross structural characterization

The phase identification, crystallite size and crystallinity of synthesized natural drill core organic matter rich black shale carbonate powder sample play great influence on the spectroscopic properties. X-ray Diffraction (XRD) technique was used to characterize gross structural analysis as well as phase purity of the natural black carbon powder. Before the XRD measurement, the diffractometer was calibrated with silicon powder ($d_{111}=3.1353 \text{ \AA}$). The crystal structure and phase purity of the raw natural drill core organic matter rich black shale powder was studied using X-ray diffraction (XRD), and the XRD patterns are shown in Fig. 6.6. Table 6.2 reports the experimental values of the diffraction angles at which the major diffraction peaks occur and the corresponding d-spacing of the black carbon powder used in this study. This analysis was compared and matched with RRUFF data base with RRUFF ID R050370.1 for dolomite and RRUFF ID R100134.9 for quartz XRD peaks [1,2]. According to XRD powder analyses, the sample contains mainly dolomite with some traces of quartz and other elements.

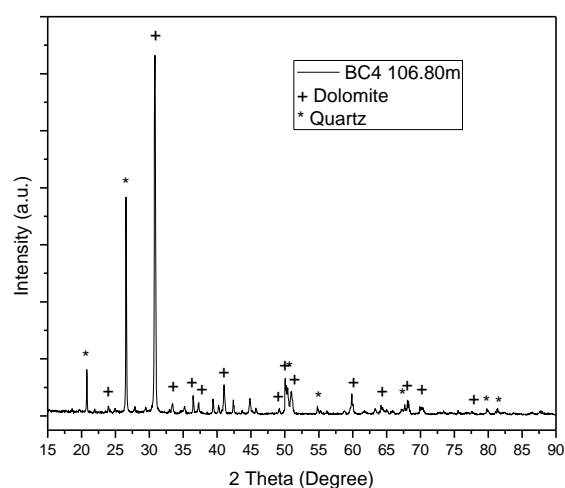


Figure 6.6 XRD patterns of the natural black shale carbon powder.

Table 6.2 Experimental diffraction angles and corresponding d-spacing of the natural black carbon powder used in this study.

2 θ (Degrees)	d-spacing (Å)
20.77	4.27,
26.55	3.35
30.52	2.92
30.82	2.89
36.46	2.46
37.27	2.41
39.39	2.28
41.01	2.19
44.82	2.02
49.17	1.85
50.13	1.81
50.94	1.79
54.78	1.67

59.88	1.54
67.32	1.38
68.16	1.37

6.4.1.2 Surface morphology

SEM images of several millimeter or sub-millimeter regions of the BC6 sample shown in Fig. 6.7 clearly confirm its poly-crystalline and multi-phase structure, with the presence of grains of about 100 micrometres in size. EDX spectra of the same sample regions allow for the determination of the local relevant chemical composition. These results still do not provide precise indications on the mineral phases that are there in the analysed sample. Phase composition is extremely critical information, in view of the drilling conditions to be adopted and, most importantly, the extraction methodology to be used to obtain from the mined ores the metal(s) of interest. The chemical information can be profitably complemented with the phase identification by means of micro-Raman spectroscopy.

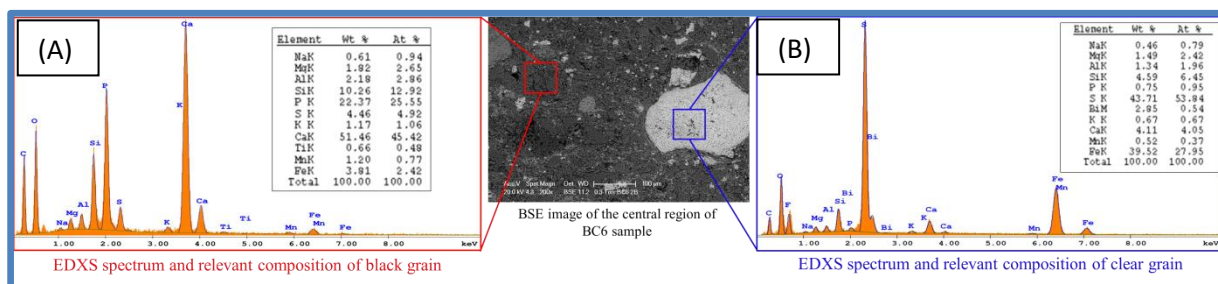


Figure 6.7 SEM image of the central region of the BC6 sample and EDX spectrum and relevant composition on black grain (A) and clear grain (B)

The surface morphology has been carried out by high resolution scanning electron microscopy (HRSEM) technique. Figure 6.8 represents the, HRSEM images of natural drill core black shale powder with different magnifications. The HRSEM images of the magnified view of the black carbon powder showed clearly highly crystalline morphology.

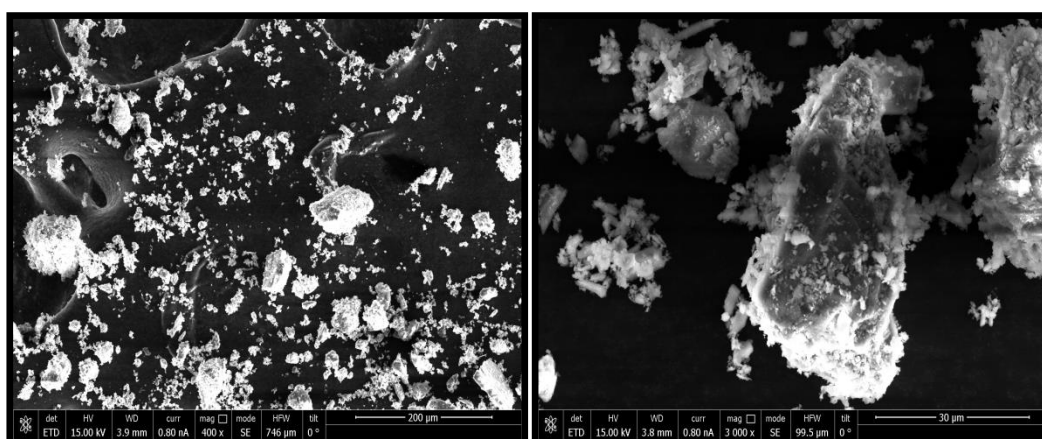


Figure 6.8 HRSEM micrographs on the natural black carbon powder with different magnifications.

Figure 6.9 represents the, HRSEM images with different magnifications of the graphitic layers on Cu substrate. The images show clearly graphitic layers connected with each other in an irregular formation. The average size of the graphitic layers varies from 100-500 nm.

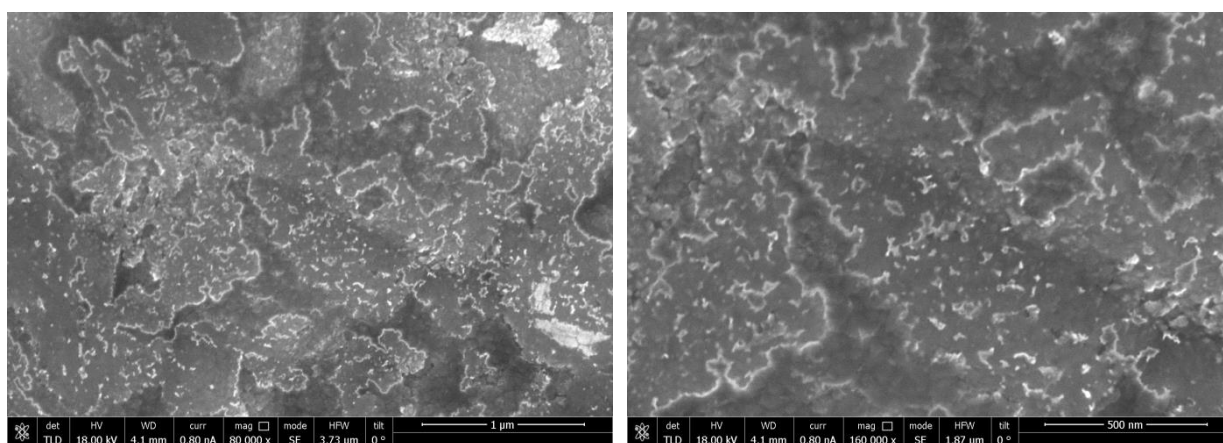


Figure 6.9 HRSEM micrograph of graphitic layers on the Cu substrate at 800 °C

6.4.2 Spectroscopic analysis of raw black carbon powder and graphitic layer Cu

6.4.2.1 Micro Raman spectroscopic analysis

For the 1st case, the analytical data were cross-checked and implemented using Raman spectroscopy and some typical spectra carried out on BC6 sample are shown in figure 6.10 below.

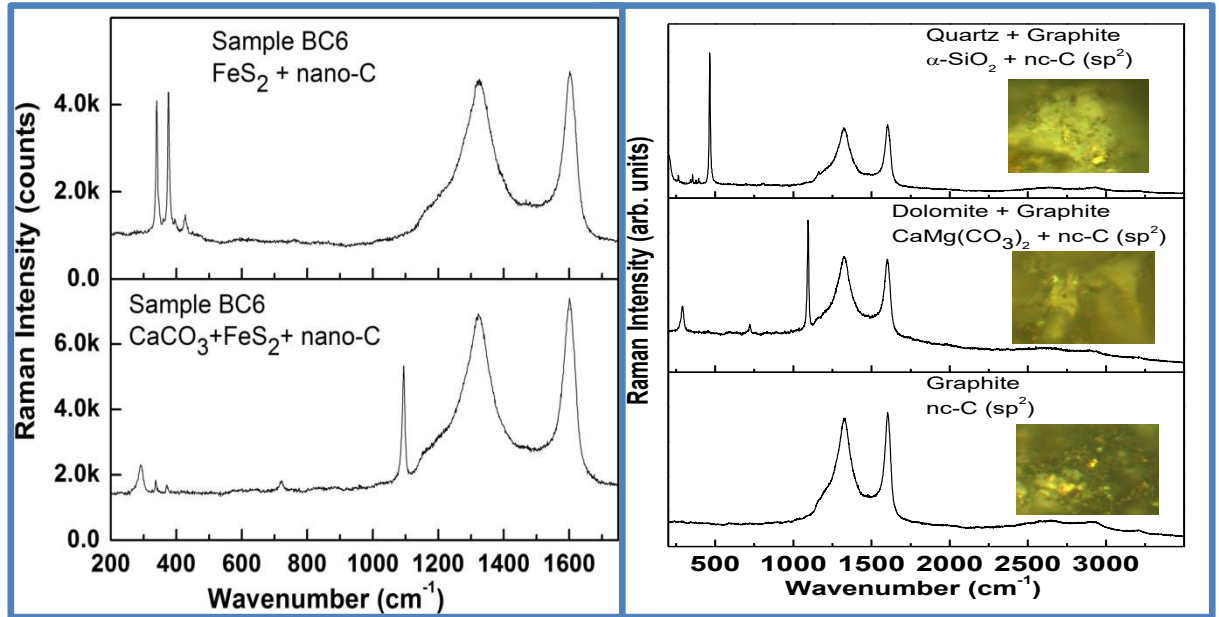


Figure 6.10 Raman spectra recorded on the black shale carbon sample BC6.

In fact, the figure reports micro-Raman spectra observed from two different micro-regions in the central part of this sample indicates in both cases a significant occurrence of microcrystalline graphite, revealed by the very strong and quite narrow D and G bands in the region of 1300-1650 cm^{-1} . In addition, a noticeable pyrite FeS_2 component is observed, in the first micro-region, while, in the other one, an important presence of dolomite $\text{CaMg}(\text{CO}_3)_2$, with a relatively minor occurrence of pyrite FeS_2 , occurs.

In fact, the pyrite (FeS_2) presence is detected on the basis of the three typical Raman peaks at about 340, 376 and 427 cm^{-1} , while in the second micro-region, besides pyrite, a noticeable amount of dolomite $\text{CaMg}(\text{CO}_3)_2$ can be inferred from the characteristic peaks observed at 292 and 1094 cm^{-1} .

Additional Raman measurements on morphologically dissimilar micro-regions, especially on single microcrystalline grains, allowed to detect, besides the always present nanocrystalline graphite, also dolomite $\text{CaMg}(\text{CO}_3)_2$ and, in turn, quartz SiO_2 alone or, even, accompanied by a minor amount of pyrite. Finally, in some regions only nanocrystalline graphite with its characteristic D (disorder) and G (graphite) bands centered at about 1326 cm^{-1} and about 1601 cm^{-1} , respectively, is observed.

Micro Raman spectroscopy was also used, in the 2nd case, the vibrational properties of the natural black shale, organic matter rich, carbon powder was studied using micro Raman spectroscopy and the Raman spectrum are shown in figure 6.11.

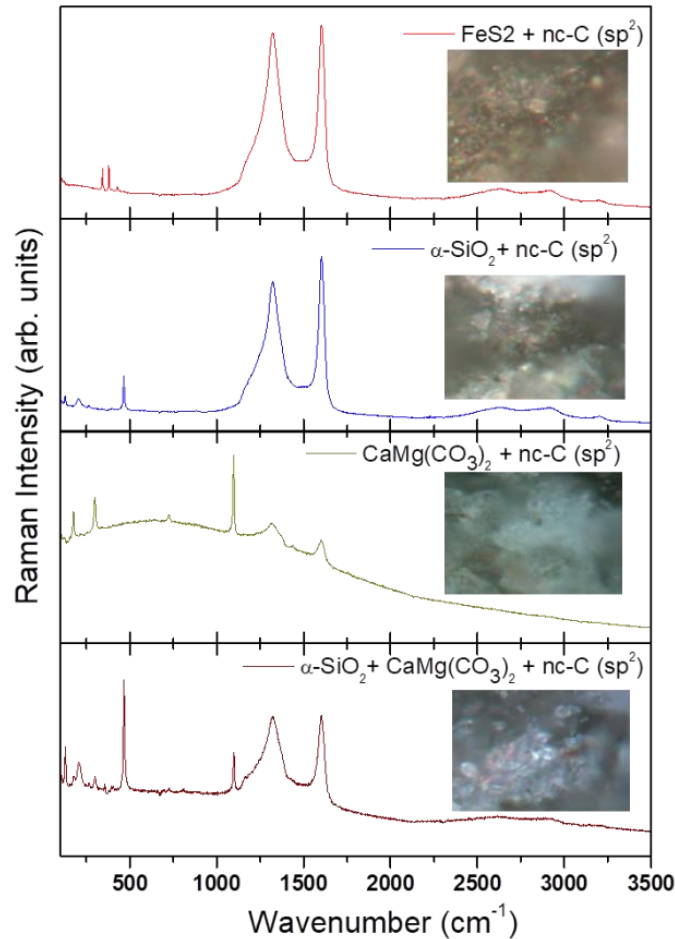


Figure 6.11 Raman spectrum of natural black shale carbon powder used as precursor.

All of the spectra carried out from raw black shale carbon powders (plotted in figure 6.11) show the two main characteristic features of highly disordered crystalline graphitic forms of carbon, namely the D (disordered) band centered at around 1323 cm^{-1} and the G (graphite) band at around 1603 cm^{-1} , superimposed to a continuous background. Apart from these strong D and G bands, the pyrite (FeS_2) presence is also detected on the basis of the three typical Raman peaks at about 340 , 376 and 427 cm^{-1} . Besides pyrite, a noticeable amount of dolomite $\text{CaMg}(\text{CO}_3)_2$ can be inferred from the characteristic peaks observed at about 292 and 1094 cm^{-1} . Additional Raman measurements on other peculiar micro-regions, especially on single microcrystalline grains, allowed to detect, besides the always present nanocrystalline graphite, quartz ($\alpha\text{-SiO}_2$) with a featured band at 464 cm^{-1} often accompanied by a minor amount dolomite $\text{CaMg}(\text{CO}_3)_2$. Despite the presence of incorporation of FeS_2 , dolomite, quartz and the strong luminescence both the D and G bands can be clearly observed in the spectrum of the raw natural carbonate sample and become more clear, in terms of intensity and of spectral profile. The intensity ratio between the D and G band was found to be $I_D/I_G = 0.95$. Their spectral features (shape and width) suggest the presence, in raw natural sample, of a remarkable structural disorder of the graphitic component, i.e. of the sp^2 carbon domains with all the other incorporated phases and are quite similar.

On the other hand, the Raman spectra carried out from sample treated via CVD technique on Cu substrate (plotted in figure 6.12) indicates an even stronger modification of the sp^2 C phase whose evolution turns out more and more correlated to the graphitic layers. And this also leads to the reducing the luminescent background.

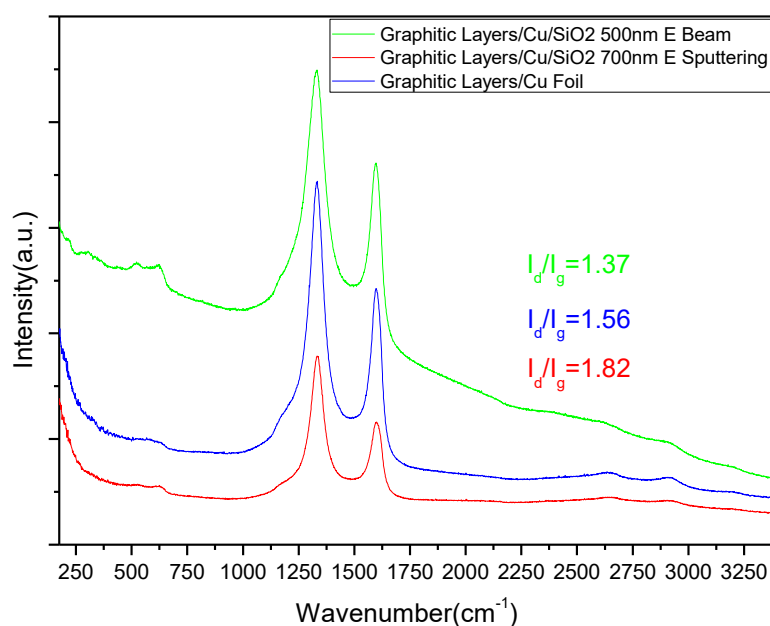


Figure 6.12 Raman spectrums of graphitic layers deposited on Cu.

In fact, in samples treated via CVD technique on Cu substrate, the two D and G bands, which were visible in the raw natural black shale powdered sample, appear as the well fully resolved peaks at about 1330 cm^{-1} and 1597 cm^{-1} , respectively. There is a subsequent shift in the D band of about 7 cm^{-1} in the sample on the Cu substrate while the position of the G band is shifted about 6 cm^{-1} , further it has sharper and better defined D and G bands as shown in figure 6.13.

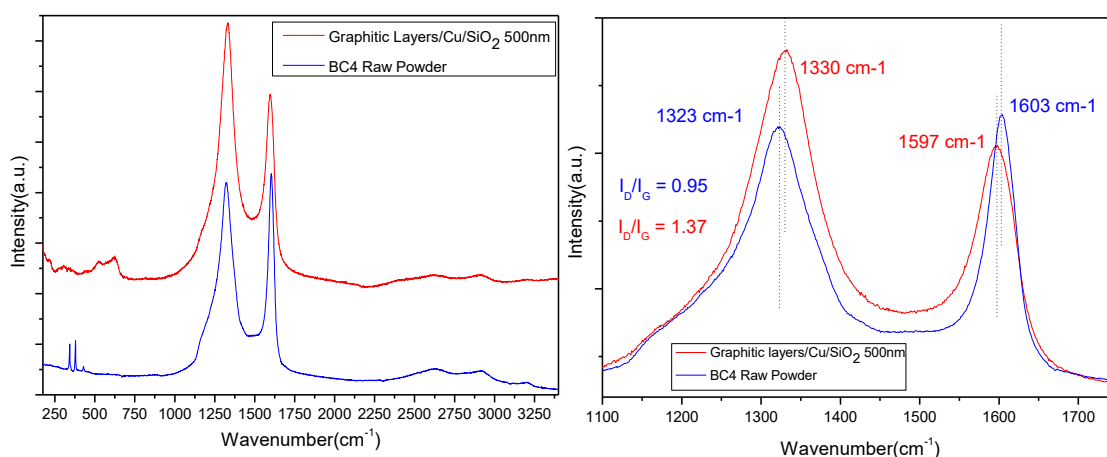


Figure 6.13 Raman spectrum comparisons of natural drill core organic matter rich black shale carbon powder and the graphitic layers/Cu.

The intensity ration between the D and G band was found to be $I_D/I_G = 1.37$, which is compatible with the formation of graphitic layers on the Cu substrate using natural organic matter rich black shale via CVD technique. Further, the G' (2D) at 2618 cm^{-1} and D+G at 2910 cm^{-1} , respectively, become clearly visible. The second order G' (2D) band, sensitive to the stacking order of the graphene sheets along the c-axis, becomes well defined. This is the typical profile of graphitic layers, which have no stacking order and can be considered as 2D nanographite systems. It is seen that in graphitic layers, the 2D band is almost completely missing since the dual-resonance is inhibited in a graphene lattice containing disorders that cannot be entirely removed by the graphitic carbon reduction and deposition process [7].

The peak cantered at about 2910 cm^{-1} turns out to be combination of D and G bands, and is referred as D+G band. The ratio of the intensities of D and G bands is a good indicator of the quality of bulk samples. Similar intensities of these bands indicate a high quantity of structural defects.

This is well accepted that the oxygen functional groups in graphitic oxide sheets can be removed and the conjugated graphene network (sp^2 carbon) will be reproduced by a chemical reduction process. The reproduced graphene network usually has a smaller average size than the original graphitic oxide, which will lead to a consequent increase in the intensity ratio I_D/I_G [8]. Thus, this change of I_D/I_G suggests that more graphitic domains are formed on Cu substrate sheets by removal of oxygen functional groups from graphitic oxide.

To conclude, the Raman study clearly shows the formation of graphitic layers from the natural black shale carbon powder via simple route of CVD technique on Cu substrate. However, on a qualitative basis we can also claim that the formation of graphitic layers is very much of good quality with easy route of synthetization and with the natural carbon powder samples. These results provide now a clear picture concerning of the chemical and phase composition of the analysed sample.

6.4.2.2 FT-IR (Fourier transform infrared spectroscopy) analysis of black shale carbon powder

FT-IR analysis was carried out on shale carbon powders, taken from sample BC4-106.80 m, and figure 6.14 shows the observed absorption spectrum. Several distinct bands in the range of 500-4000 cm^{-1} region were obtained. The major band appeared at about 728 cm^{-1} assigned to symmetric CO_3 deformation, 852 cm^{-1} assigned to asymmetric CO_3 , 1447 cm^{-1} assigned to asymmetric CO_3 stretching deformation which corresponds for the dolomite mineral phase. Other dolomite characteristic FTIR absorptions bands at about 2625 cm^{-1} and 3015 cm^{-1} are also observed. Further, quartz is a very common mineral phase in this kind of sample and the modes assigned at about at 470 cm^{-1} and 515 cm^{-1} for alpha-quartz (2) Si-O-Si symmetrical stretching vibration at 780 cm^{-1} and 799 cm^{-1} as a doublet for alpha-quartz, which are its characteristic vibrations; (3) Si-O-Si asymmetrical stretching vibration is located at 1098 cm^{-1} for alpha-quartz, covering a significant area in the finger print region in the IR spectrum [9-11]. The obtained result is consistent with earlier results obtained with the other characterization techniques.

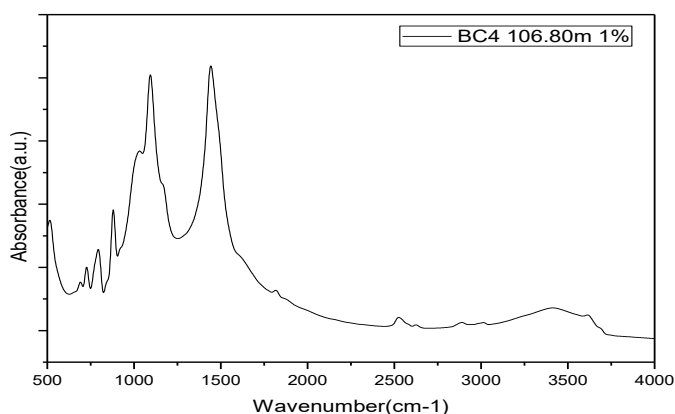


Figure 6.14 FTIR spectrum of BC4-106.80m powder.

6.5 Conclusions

The combination of EDXS and micro-Raman provides a clear picture of both the chemical and phase composition of the analysed samples. The experimental tools used in this feasibility study allow probing a very small sample region, especially when it is compared to the interesting size for real mineralogical core drills.

The second set of experiments provides a comprehensive description of the present work, in which we have synthesised graphitic layers on the Cu substrate using natural black shale carbon powder containing mainly clay minerals like quartz and dolomite. The shape dependent structural/microstructural characteristics and vibrational properties of the natural black shale carbon powder and the synthesised graphitic layers have also been explored in detail. The obtained results strongly suggest that our synthesised graphitic layers from the black shale carbon powder are a promising candidate towards the low cost and easy route and for potential relevant applications such metal coating to avoid corrosion.

6.6 Reference

1. <http://rruff.info/chem=Mg,C,O/display=default/R050370>
2. <http://rruff.info/quartz/source/asc/R100134>
3. F. Tuinstra , J.L. Koenig , J. Chem. Phys. 1970 , 53, 1126.
4. D. Graf, F. Molitor, K. Ensslin, C. Stampfer, A. Jungen, C. Hierold, L. Wirtz, Nano Lett. 2007, 7, 238.
5. A.C. Ferrari, Phys. Rev. Lett. 2006, 97, 187401.
6. Z.Y. Ji, X.P. Shen, Y. Song, G.X. Zhu, Mater. Sci. Eng. B, 2011, 176 711.
7. C. Xu, X. Wang, J.W. Zhu, J. Phys. Chem. C 2008, 112, 19841.
8. H. Feng, X. Wang, D. Wu, Ind. Eng. Chem. Res. 2013, 52, 10160.
9. S. Gunasekaran, G. Anbalagan, S. Pandi, J. Raman Spectrosc. 2006, 37, 892.
10. V.C. Farmer, Mineralogical Society Monograph No. 4. Mineralogical Society, London, 1974, 399.
11. T.T. Nguyen, L.J. Janik, M. Raupach, Aust. J. Soil Res. 1991, 29, 49.

CHAPTER: 7

Micro-Raman spectroscopy investigations on B-doped Silicon Oxycarbide [SiOC(B)] powders underwent thermal treatments at high-temperature

7.1 Introduction

Polymer-derived ceramics, PDCs, constitute a new class of amorphous ceramic obtained through pyrolysis of pre-ceramic polymers [1]. First examples of PDCs were the silicon carbide fibers developed by Yajima in 1975 for high temperature structural application [2]. Since then, two main ternary PDCs families have been extensively studied: silicon oxycarbides, SiOC, and silicon carbonitrides, SiCN. In both cases their structure is based on mixed Si-centered tetrahedral with N, C and O sitting at the corners creating an amorphous covalent ceramic network [3-6]. Another common feature of PDCs structure is the presence of carbon atoms bonded to each other and forming an extra carbon phase, called “free carbon” [7,8]. The room temperature conductivity increases of several orders of magnitude with the maximum pyrolysis temperature, T_p , in the range 1000°C-1400°C. This behavior has been related to structural transformations of the polymer derived ceramic which occur in this temperature range, including H_2 release with increase in the sp^2/sp^3 ratio of C atoms in the free carbon layers, [9,10] phase separation with the formation of a percolating free carbon network and formation of nanocrystalline SiC [11-13].

This report deals with the study of sol-gel -derived silicon boron oxycarbides synthesised, via sol-gel route, from poly(boro)siloxanes enriched with different amounts of boron. Their structural evolution under thermal annealing at 1200°C and 1400°C has been investigated by micro-Raman spectroscopy in order to get insights about the effects of B-doping on both the nanostructure and on the electrical conductivity of these materials.

These results were published as ‘The effect of B-Doping on the electrical conductivity of polymer-derived Si(B)OC ceramics’; G.D. Sorarù, G. Kacha, R. Campostrini, A. Ponzoni, M. Donarelli, **A. Kumar** and G. Mariotto; Journal of the American Ceramic Society (2017),100:4611-4621.

7.2 Synthesis of the B-doped polymer derived Si(B)OC ceramics with different pyrolysis temperature

Sol-gel method was used for preparing boron-free and boron-containing gels, precursors for SiOC and Si(B)OC ceramics. Methyltriethoxysilane, MTES, (ABCR, Karlsruhe, Germany) and boric acid, B(OH)₃, (Carlo Erba, Milan, Italy); were used as received. B-free SiOC gels were obtained with a two steps acid/basic process. MTES was first hydrolyzed under reflux at 70 °C for 1 hour with an acidic HCl solution (pH=1) using a H₂O/Si molar ratio of 3. After that an ammonia solution (30 wt%) was added to the hydrolyzed alkoxide with molar ratio of NH₃/MTES= 1/5. The mixture was then cooled to room temperature and left for gelation in open polypropylene test tubes. B-containing SiOC precursors were obtained using a non-hydrolytic process starting from MTES and boric acid following a published procedure. The proper amounts of B(OH)₃ - in order to obtain a nominal B/Si atomic ratios of 0.1, 0.3 and 0.5 - were added to MTES. The system was stirred at 70 °C under reflux until complete dissolution of the boric acid into MTES. The homogeneous solutions were then poured into open polypropylene tubes for gelation. Gelation was completed in less than 2 weeks depending from the composition. [14] After gelation the wet gels have been dried in an oven in two steps (50 °C for 10 day, 80 °C for 5 day). The dried samples were then milled to coarse gel powders and converted into the corresponding SiOC and Si(B)OC ceramics using a pyrolysis treatment in flowing argon (100 mL/min) at 1200 °C and 1400 °C with an heating rate of 10 °C/min and a dwell time at the maximum temperature of 1 hour.

7.3 Characterization of the B-doped polymer-derived Si(B)OC ceramics with different pyrolysis temperature

The structural and vibrational evolution of both pure and B-doped powders pyrolyzed at 1200 °C and 1400 °C was investigated by micro-Raman spectroscopy by means of a single stage Horiba-Jobin Yvon spectrometer (model LABRAM HR800) mounting a He-Ne laser as excitation source (wavelength = 632.8 nm) and a notch filter in order to reject the Rayleigh line. Raman spectra were excited in backscattering geometry over the Stokes-shifted region between 500 and 3000 cm^{-1} by a He-Ne laser (wavelength excitation=632.8 nm), whose power at the samples surface was kept below 2 mW. The laser beam was focused onto the sample surface through an 80X magnification objective, having a numerical aperture N.A. = 0.75 and providing a surface spot of about 2 μm in size. The selection of the sample micro-region worth to be measured was achieved by means of a micro-manipulator operated under direct optical inspection on a colour camera interfaced to the microscope objective used to focus the laser beam onto the sample. The scattered radiation was dispersed by a 600 lines/mm diffraction grating and detected at the spectrograph output by a red-extended multichannel detector, a CCD with 1024x256 pixels, cooled by liquid nitrogen. The spectral resolution was about 1 cm^{-1} /pixel over the spectral range of interest. The spectral calibration was provided by the emission lines of an Ar lamp. Finally, in order to assess the reproducibility of the recorded spectra, repeated micro-Raman measurements were carried out under the same experimental conditions from different grains of the investigated powders.

7.4 Results and discussions

The first- and second-order Raman spectra of SiOC and Si(B)OC ceramic powders underwent thermal treatments at 1200 °C and 1400 °C are shown in figure 7.1. The spectra carried out from samples treated at 1200 °C (plotted in figure 7.1 A) consists of the two characteristic features of highly disordered graphitic forms of carbon, namely the D (disordered) band centered at around 1350 cm^{-1} and the G (graphite) band at around 1600 cm^{-1} , superimposed to a continuous background. Despite of the strong luminescence both the D and G

bands can be clearly observed in the spectrum of the pure SiOC sample and become more defined, in terms of intensity and of spectral profile, by increasing the B content. Their spectral features (shape and width) suggest the presence, in pure SiOC sample, of a remarkable structural disorder of the graphitic component, i.e. of the sp^2 carbon domains, although the related fractional amount seems to be enhanced by the B presence at the highest content (see figure 7.1 A, top panels). In fact, the spectral features of Si(B)OC loaded with the highest B content but treated at 1200 °C turns out quite similar, although a little broader, to those of SiOC sample treated at 1400 °C (see Figure 7.1 B).

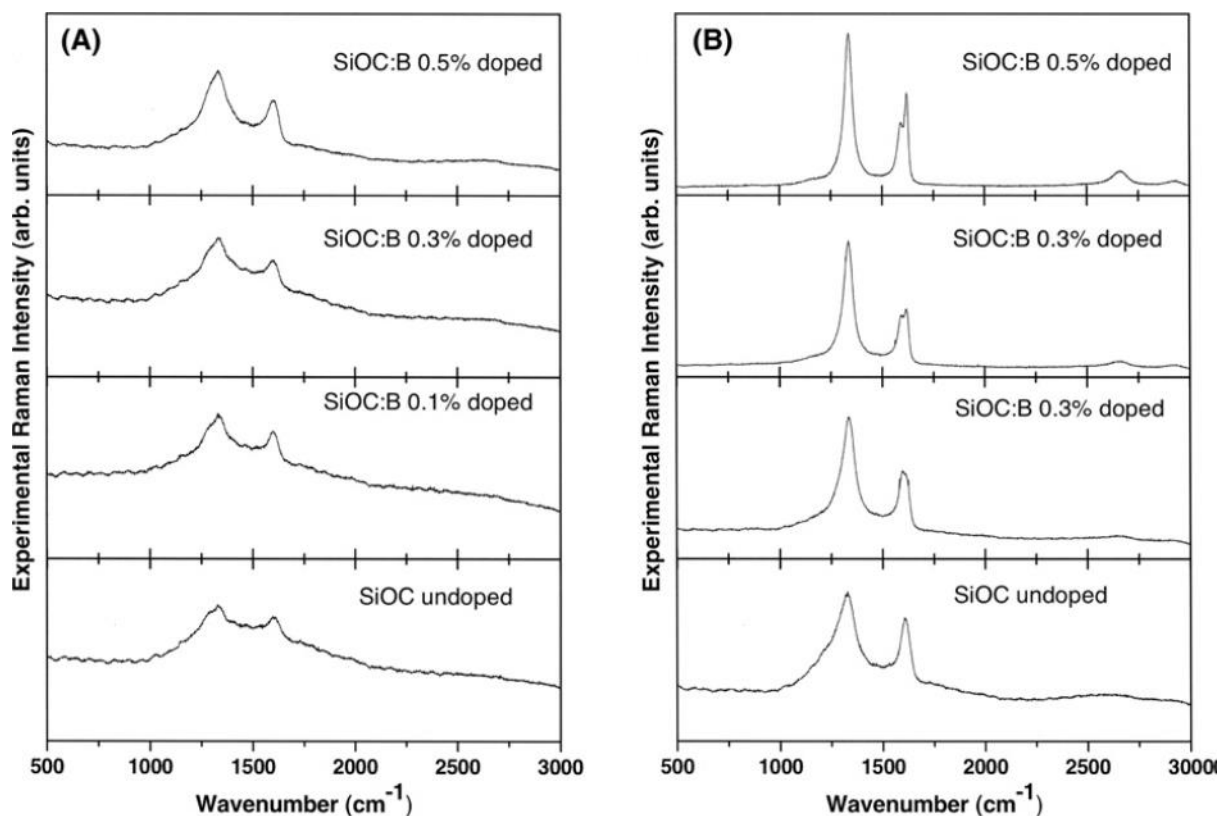


Fig. 7.1 Raman spectra recorded on the SiOC and Si(B)OC powders pyrolyzed at: (A) 1200 °C and (B) 1400 °C.

On the other hand, the Raman spectra carried out from samples treated at 1400 °C (plotted in figure 7.1 B) reveal an even stronger modification of the sp^2 C phase whose evolution turns out more and more correlated to the B content. Finally, the

B presence seems to cause even a relevant quenching of the luminescent background. In SiOC powders treated at 1400 °C the two D and G bands, which were visible in the SiOC sample treated at 1200 °C, appear as well fully resolved peaks at about 1329 cm^{-1} and 1605 cm^{-1} , respectively. Similarly as for B/Si=0.1 sample heated at 1400°C two clear peaks of D (1334 cm^{-1}) and G (1605 cm^{-1}) are observed, the latter one occurring as a non-resolved doublet.

Increasing the B doping leads to sharper and better defined D and G bands, which turn out in quite narrow Raman peaks in the heavier B-doped samples. For the samples with the higher B content (B/Si=0.3 and 0.5) together with the D and G bands also the bands D' at about 1620 cm^{-1} , G' (2D) at 2658 cm^{-1} and D+G at 2913 cm^{-1} , respectively, become clearly visible. The occurrence of the D' band in B-doped carbons has been attributed to the partial substitution, in the graphene layers, of C with B atoms resulting in the formation of BC_3 units, which reduce the in-plane correlation and act as point defects. The enhancement of this band should be, therefore, ascribed to an increase in the local distortion of graphite lattice, which is reflected by the behaviour of the D band intensity. The second order G' (2D) band, sensitive to the stacking order of the graphene sheets along the c-axis, becomes well defined at 1400 °C and peaks at 2658 cm^{-1} for B/Si=0.3 sample. This is the typical profile of turbostratic graphite samples, which have no stacking order and can be considered as 2D nanographite systems. The peak centred at about 2913 cm^{-1} turns out to be combination of D and G bands, and is referred as D+G band. B/Si=0.5 sample shows a similar behavior with that of B/Si=0.3 samples, while the former shows sharper peaks. To conclude, the Raman study clearly shows that increasing either the pyrolysis temperature or the boron content promotes the ordering of the highly disordered graphitic structures formed at lower temperature. However, on a qualitative basis we can also claim that a boron addition of a B/Si=0.5 seems to cause a similar effect as that due to increasing the pyrolysis temperature of 200 °C on the undoped material since the spectrum of the SiOC sample treated at 1400 °C is very much alike that of the Si(B)OC (B/Si=0.5) annealed at 1200 °C.

7.5 Conclusions

Polymer-derived Si(B)OC ceramics with nominal boron atomic content up to B/Si=0.5 have been synthesized and characterized by micro Raman spectroscopy. The studied Si(B)OC powders were thermally treated at two different temperatures, namely 1200 °C and 1400 °C. The structural characterization reveals that B partially substitutes C in the sp^2 graphene layers with the formation of BC_3 units. The Raman analysis shows that the sp^2 carbon phase undergoes a strong evolution from 1200 °C to 1400 °C with a growth and ordering of the graphene domains. The clear presence of the D' band for the B-doped Si(B)OC, which is more intense for the samples with the higher B content, suggests the presence of B atoms in substitutional positions within the sp^2 C planes.

7.6 References

1. P. Colombo, G. Mera , R. Riedel, G.D. Soraru, J. Am. Ceram. Soc. 2010, 93, 1805.
2. S. Yaiima S, J. Hayashi, M. Omori, Chem Lett. 1975, 9, 931.
3. G.D. Soraru, F. Babonneau, J.D. Mackenzie, J. Non-Cryst Solids. 1988, 106, 256.
4. C.G. Pantano, A.K. Singh, H. Zhang, J. Sol-Gel Sci. Technol. 1999, 14, 7.
5. S.J. Widgeon, S. Sen, G. Mera, E. Ionescu, R. Riedel, A. Navrotsky, Chem Mater. 2010, 22, 6221.
6. G. Mera, A. Navrotsky, S. Sen, H.J. Kleebe, R. Riedel R. J. Mater. Chem. A. 2013, 1, 3826.
7. H.J. Kleebe, Y.D. Blum, J. Europ. Ceram. Soc. 2008, 28, 1037.
8. S. Widgeon, G. Mera, Y. Gao, Chem Mater. 2012, 24, 1181.
9. Y. Chen, F. Yang, L. An, Appl Phys Lett. 2013, 102, 231902.
10. V.L. Nguyen, C. Zanella, P. Bettotti, P.J. Soraru, Am. Ceram. Soc. 2014, 97, 2525.
11. J. Cordelair, P. Greil, J. Eur. Ceram. Soc. 2000, 20, 1947.
12. C. Haluschka, C. Engel, R. Riedel, J. Eur. Ceram. Soc. 2000, 20, 1365.
13. F. Dalcanale, J. Grossenbacher, G. Blugan, J. Europ. Ceram. Soc. 2014, 34, 3559.
14. G.D. Soraru, F. Babonneau, C. Gervais, N. Dallabona, J. Sol-Gel Sci. Technol. 2000, 18, 11.

CHAPTER: 8

Conclusion, potential outcomes and future road map

In this study the carbon nanomaterials were successfully synthesized by the chemical vapour deposition process using natural minerals. The chemical vapour deposition process with temperature (700-900 °C), is highly efficient synthesis route for synthesising carbon nanomaterials. The carbon nanomaterials synthesized during the course of this research work were characterized with different experimental techniques. The structural and microstructural characterizations along with surface morphology were carried out by x-ray diffraction (XRD), high resolution scanning electron microscopy (HRSEM)/environmental scanning electron microscopy (ESEM). The spectroscopic characterization of natural minerals and as synthesized carbon nanostructures were investigated by micro Raman, FTIR spectroscopic techniques. The outcome of the as synthesised carbon nanostructures in terms of production and application will enhance their rapid growth of applications in day to day life.

In the **3rd chapter**, the main highlights of the present work are to explore the successful demonstration of the synthesis of carbon nanostructures which can be easily scaled up in bulk quantity under methane flux flow on natural limonite laterite. This method and the catalytic materials we opted for the synthesis of carbon nanostructures is very simple, effective and economic. The ESEM results indicate that the average size of MWCNTs is 10-100 nm agglomerated with each other. In the **4th chapter**, we have studied the synthesis and characterization of growth of carbon nanostructures on natural limonite laterite ore with low-Ni content iron, and comparative studies as a function of the temperature as well as of the $H_2/C_2H_4/Ar/O_2$ flux ratio supplied on the catalyst. The deposition rate of carbon material has been found to significantly vary, this finding being rarely reported in the literature on natural materials. Another interesting behaviour of the as synthesized carbon nanostructures is that it starts forming a carbon nano spheres when the deposition temperature increases. Because high temperature

induces perturbations in the CNFs and hence the breakage of CNFs occurs into spheroids and that can be inferred from the transformation of CNFs (10-80 nm) to CSs (500-700nm), which can be considered heterostructures with uniform and periodic beaded CS morphologies. Further, when Ar/O₂/H₂ was flown along with the C₂H₄, at 700-800 °C, the formation of MWCNTs was 700, 800, 900 °C achieved, the presence of which was confirmed by the exploited characterization techniques. These findings confirm the efficient and suitable approach for the tailoring the carbon nanostructures architecture from the natural limonite laterite. The same approach can be exploited for scaling up for large scale production due to easy availability of catalyst materials which could have great potential application in particle-based technologies such as, drug delivery, sensors, electronics, catalysis, and other nanotechnology.

In the **5th chapter**, carbon nanotubes and carbon nanofibers were synthesised as well on the natural drill core siliceous breccia powder containing mainly quartz and some traces of hematite and goethite. Furthermore, comparative studies by varying the H₂/C₂H₄ flux ratio supplied on the catalyst. The combined analyses by ESEM and micro-Raman spectroscopy provide a clear picture of both the elemental composition and phase formation of the samples. The obtained results strongly suggest that siliceous breccia powder is a promising candidate towards the low cost and easy approach for the mass production of the CNTs/CNFs which are potential candidates for the relevant applications.

The **6th chapter** deals with two cases of drilled core organic matter rich black shale samples. In the first case, the results of combined spectroscopic analyses, performed on an organic matter rich black carbon sample, are considered. The sample is a piece of a drill core extracted from a geological survey for raw materials mining purposes. The study concerns different aspects: 1) micrometric grain size; 2) minerals chemical bonding and inertial organic matter; 3) the presence of fine inter-grown clay minerals, sulphides quartz and carbonates. The aim of the work was to detect the major mineral component phases following an experimental protocol setting up the bases that will be developed further within the EU-H2020 SOLSA project (<http://www.solsa-mining.eu>), funded by the EU-H2020 Raw Material program. Further, in the second case, black shale carbon

powders, mainly containing clay minerals like quartz and dolomite, were exploited to obtain coating layers, on Cu substrates. The shape dependent structural/microstructural characteristics and vibrational properties of the pristine black shale powders and the graphite layers deposited on Cu substrates by using the same powders as precursor have been explored in detail. Furthermore, comparative studies by varying the temperature and the different Cu substrates as catalysts.

In the **7th chapter**, work deals with the investigation of structural and electrical properties of silicon oxycarbide powders, doped with different amounts of boron, produced from sol-gel-derived poly(boro)siloxanes. The evolution of Raman spectra of the different samples, annealed at 1200 °C and 1400 °C, has been investigated in order to get insights about the effects of Boron-doping on the nanostructure and on the electrical conductivity of the studied materials. The Raman analysis shows that the sp^2 carbon phase undergoes a strong evolution from 1200 °C to 1400 °C with a growth and ordering of the graphene layers. The clear presence of the D' band for the B-doped Si(B)OC, which is more intense for the samples with the higher B content, confirms the insertion of B atoms in substitutional positions in the sp^2 C planes.

A road map is planned for the synthesis of carbon nanostructures exploiting natural oxide minerals in view of their potential applications for energy storage, drug delivery, sensors, electronics, catalysis, and other nanotechnology uses. Along with that our major research work will be establishing the cost effective and large scale synthesis process of carbon nanostructures from the natural materials that require less energy and could be completed in short time period.